Electron dynamics in inner-shell photo-ionization, dielectronic recombination and electron impact excitation

by

Qianxia Wang

A dissertation submitted to the Graduate Faculty of
Auburn University
in partial fulfillment of the
requirements for the Degree of
Doctor of Philosophy

Auburn, Alabama
August 6, 2016

Keywords: Auger, Dielectronic Recombination, fine-structure excitation

Approved by

Stuart Loch, Chair, Associate Professor of Department of Physics
Michael S. Pindzola, Professor of Department of Physics
Eugene Oks, Professor of Department of Physics
Allen L. Landers, Howard Carr Professor of Department of Physics
Konrad Patkowski, Assistant Professor of Department of Chemistry and Biochemistry

Abstract

This dissertation includes three main topics: Dynamics of outgoing inner shell photoionized electrons and Auger decay electrons, an investigation into the recently proposed mechanism of below threshold dielectronic recombination and electron impact fine-structure excitation of Ne^+ and Ne^{2+} at very low temperatures.

For the first topic, we compare our time-dependent numerical method with a widely used analytical one at different photo-electron energies. We determine that the time-dependent numerical method is more accurate in the low and medium energy region. We apply this method to investigate inner shell photo-ionization followed by Auger decay in Kr at low energies (including as low as zero atomic units of energy). We investigate an interesting feature in the relative angular distribution of the outgoing electrons. To confirm the validity of this phenomenon, we use a Classical Trajectory Monte Carlo Method to re-simulate the process, with similar results being generated. A physical mechanism is identified for the unusual features in the relative angular distribution.

The second topic concerns a newly proposed mechanism for dielectronic recombination. The traditional definition for dielectronic recombination only counts the contribution of above threshold (or positive energy) resonances which can be accessed via free electrons. This definition leads to several problems when the temperature is very low. For example, the dielectronic recombination coefficient becomes very sensitive to the energy position of resonances and whether they are above or below threshold. Moving a resonance by a few meV from above to below threshold can change the dielectronic recombination rate coefficient by large values, often factors of 10 or 100. A new recombination mechanism was proposed recently, pointing out that certain below threshold resonances should also be counted in the rate coefficient calculation due to an interaction with Rydberg electrons. This new

mechanism has not been an experimentally confirmed. We proposed that below threshold satellite line observation can be used to prove the existence of this new mechanism. We also develop a method to identify ions with near threshold resonances and several key ions are selected to re-evaluate their dielectronic recombination rate coefficient with the inclusion of below threshold resonances contributions.

For the last topic, we calculate collision strengths, effective collision strengths and excitation rate coefficients for fine-structure electron impact excitation of Ne^+ and Ne^{2+} using different R-matrix techniques and different target expansions. We compare target energies and Einstein A coefficients with NIST values, and compare calculated effective collision strengths with existing values. A recommended dataset is provided for each ion, along with an estimate of the uncertainty in the collision data. This work has important applications in ultra-low temperature astrophysical plasmas.

Acknowledgments

Firstly, I would like to express my sincere appreciation to my advisor Dr. Stuart Loch for the support of my Ph.D study and related research, for his patience, encouragement, and immense knowledge. His guidance helped me in all the time of research and writing of this thesis. I could not have imagined having a better advisor and mentor for my Ph.D study.

Besides my advisor, I would like to thank the rest of my thesis committee: Dr. Michael S. Pindzola, Dr. Eugene Oks, Dr. Allen L. Landers, and Dr. Konrad Patkowski for their valuable comments and advices, but also for the hard question which incented me to widen my research from various perspectives.

Lastly, my sincere thanks also goes to my family members for their help and encouragement in both research and life. Without their support, I can not be so persistent in chasing my interest in physics research.

Table of Contents

List of Figures

List of Tables

xvii

Chapter 1

INTRODUCTION

In this chapter an overview is provided for the physical mechanisms investigated in the later chapters, a description is also given of the important areas of application for each of the projects. Two of the chapters have been published (chapters 2 and 3 [1, 2]) and one has been submitted for publication (Chapter 6).

1.1 Electron dynamics for inner shell photoionization followed by Auger decay

Considering first the study of inner shell photoionization followed by Auger decay. The application of this work is for the study of electron dynamics in X-ray photoionization experiments at such as the Advanced Light Source (ALS - `https://www-als.lbl.gov/`). If an X-ray photon interacts with an atom, there are various mechanisms that can lead to the ejection of several electrons. This process can happen in the form of sequentially losing electrons one by one, or simultaneously all at once, with generally the former one being the dominant mechanism. If the energy of X-rays is higher than the inner-shell ionization potential, electrons in those inner shell are inclined to be photo-ionized. Then the atom can auto-ionize via an Auger decay.

The process of inner-shell photoionization followed by Auger decay is illustrated in Figure 1.1 using Neon as an example. After absorbing a photon with energy more than the ionization potential, the electron in the K-shell will be ionized. This free (photo-ionized) electron will travel away from the atom. Then the atom with an inner shell hole is not stable, one electron in an outer subshell can decay to a lower subshell to fill the hole and the extra energy can be given to another bound electron. If the extra energy is large enough to ionize the electron it will also be emitted from the atom and one will have two outgoing electrons

1

that can interact with each other. It is the interaction of these outgoing electrons that is the focus of chapters 2 and 3 of this dissertation.
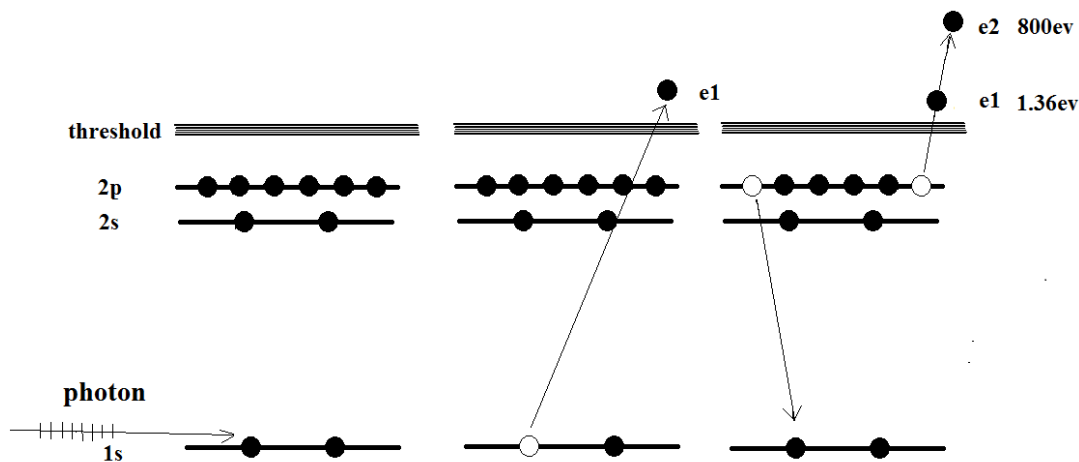
Figure 1.1: Schematic showing the process of K-shell photo-ionization followed by Auger decay

The inner-shell photo-ionization followed by Auger decay is an important and challenging research topic in AMO physics. Firstly, the dominant ionization mechanism in the x-ray regime is core-shell photo-ionization followed by Auger decay (except for K-shell ionization of heavy atoms, where fluorescent decay can dominate). Also this topic is important because Auger spectroscopy is a powerful probe of electron correlations in atoms [3]. Thirdly, this study also provides an ideal environment to study ultra-fast phenomena which is critical in understanding different dynamics, such as radiation damage, chemical reactions, etc. Because the core-hole lifetimes are typically a few femto-seconds for shallow core levels in the soft x-ray region and 1 fs or less for deep core levels, these system are natural laboratories in which to study ultrafast dynamics [4]. And lastly, this process results in three charged particles, which is relatively difficult to describe quantum mechanically or classically.

The study of post-collision interaction (PCI) is an important means of investigating the dynamics of photo-emission. In general, PCI results from the change in the coulomb potential felt by the slow moving photo-electron when Auger decay occurs. This is reflected in the line shape and peak position of the photo-electron energy distribution. Another important

quantity studied in the following chapters is the relative angular distribution of the two outgoing electrons which shows the influence of the electron-electron interaction.

There are two projects related to this topic which will be described in Chapters 2 and 3. Chapter 2 contains a comparison of two quantum mechanical methods used to describe the inner shell photo-ionization followed by Auger decay in Neon. One of the two methods is to numerically solve the Time Dependent Schrödinger Equation (TDSE), in which all three pairs of interactions are fully considered. The other group of methods is also a quantum mechanical method, but based on the solution of the Stationary Schrödinger Equation (SSE). All three pairs of interactions are taken into account but with different approximations according to different situations. We will show that the TDSE method works well in the low photo-electron energy regime both in calculating the photo-electron energy and relative angular distributions. In Chapter 3, we investigate the same topic in the low photo-electron energy distribution for Kr. To confirm the validity of a surprising shape in the relative angular distribution for low photo-electron energies, we recalculate this distribution with a Classical Trajectory Monte Carlo (CTMC) method, with similar results being obtained.

1.2 The contribution of near threshold resonances to dielectronic recombination rate

The second topic of this dissertation concerns near threshold resonances in dielectronic recombination. When an electron collides with an ion, several kinds of process can happen. If the energy of the electron is high enough, one electron of the ion can be knocked out via an electron-impact single ionization. Also the electron can be captured directly by the ion, causing a recombination. The three types of recombination usually considered are Radiative Recombination (RR), Dielectronic Recombination, and three-body recombination. In RR a free electron is captured into the potential well of the ion and a photon is emitted, the RR rate coefficient drops off quickly with increasing temperature and so is most important in low temperature plasmas. Three-body recombination involves a collision of two free electrons in

the presence of the ion, with one of the electrons losing enough energy to be captured into a bound state of the recombined ion. It is usually small unless the electron densities in the plasma become very large (typically greater than 1×10^{16} cm^{-3}). The remaining process of Dielectronic Recombination (DR) involves two steps. Firstly, a positive ion captures a free (positive energy) electron into one of its bound states. The extra energy from this electron promotes another electron of the ion to an excited state. Thus, the ion becomes doubly-excited. This first step is called resonance capture. Then this doubly-excited ion can stabilize via radiative dacay (either a core electron decay (Type I) or Rydberg electron decay (Type II)). If the final state is below the ionization potential then the recombination process is complete and the ion has gained an electron. Using a Beryllium-like case as an example, the two processes can be illustrated with equations:

$$1s^2 2s^2 (^1S_0) + e \rightarrow 1s^2 2s 2p (^1P_1) nl \tag{1.1}$$

$$
\begin{aligned}
1s^2 2s 2p (^1P_1) nl \quad &\rightarrow \quad 1s^2 2s^2 (^1S_0) nl + h\nu \quad (Type\,I) \tag{1.2} \\
&\rightarrow \quad 1s^2 2s 2p (^1P_1) n'l' + h\nu' \quad (Type\,II). \tag{1.3}
\end{aligned}
$$
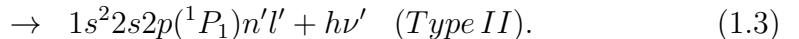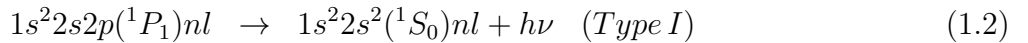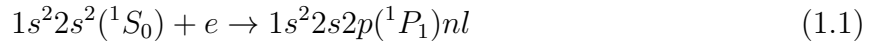
DR was first recognised and quantified by Massey and Bates [5] as a recombination process. It can have an important effect on the ionisation equilibrium, level populations and time evolution of the plasma ions in a variety of astrophysical and laboratory plasmas. Most applications of dielectronic recombination have concentrated on this particular aspect but its importance as a mechanism producing spectral lines has also been investigated, with satellite line spectroscopy being key to many plasma diagnostics [6].

DR always plays a more important role than RR does in high-temperature plasmas. At low temperatures the two processes can be competitive. However, DR is often an important recombination process for ions found in low temperate and low density photoionized plasmas.

The focus on the low temperature DR rate coefficients in this dissertation will be for these photoionized plasmas (e.g. planetary nebulae).

Since the pioneering work by Burgess [7], various theoretical methods have been used to calculate DR rate coefficients of many atomic ions [8, 9]. For example DR rate coefficients based upon the work of Badnell et al. [8] are used in the Atomic Data and Analysis Structure (ADAS www.adas.ac.uk) database to model both laboratory and astrophysical plasmas. There are, however, several problems existing in the current DR databases, particularly for low temperature plasmas. For example, the DR rate coefficient can be very sensitive to the low energy resonance position. Eliminating one resonance near threshold can change the DR rate coefficients by a few order of magnitude, as was found in the case of O^{4+} [10]. This is shown in Fig. 1.2 where the removal of one resonance at 60 meV above threshold changes the DR rate coefficient by two orders of magnitude at low temperatures. Another indication of the importance of this topic is that theoretical calculations for DR rate coefficient may be very difference from the experimental data [11]. Near threshold resonances could be contributing factors to both of these phenomena.

A new mechanism for Dieletronic Recombination was proposed recently by Robicheaux et al. [12]. At low temperatures for specific plasma conditions, it is possible that electrons can capture into below threshold doubly excited states. However, the current definition of DR only counts the contribution of above threshold resonances, so these below threshold contributions are not included in DR databases. The new mechanism suggests that we should re-define the DR rate coefficient to include role of the below threshold resonances. Including the below threshold resonances in the DR calculation was shown to eliminate the hyper sensitivity of the rate coefficient to the near threshold energy positions of doubly excited states for Mg^{8+} [12]. The existence of this new mechanism has not be demonstrated in atomic experiments, because the below threshold resonance contribution can not be measured in
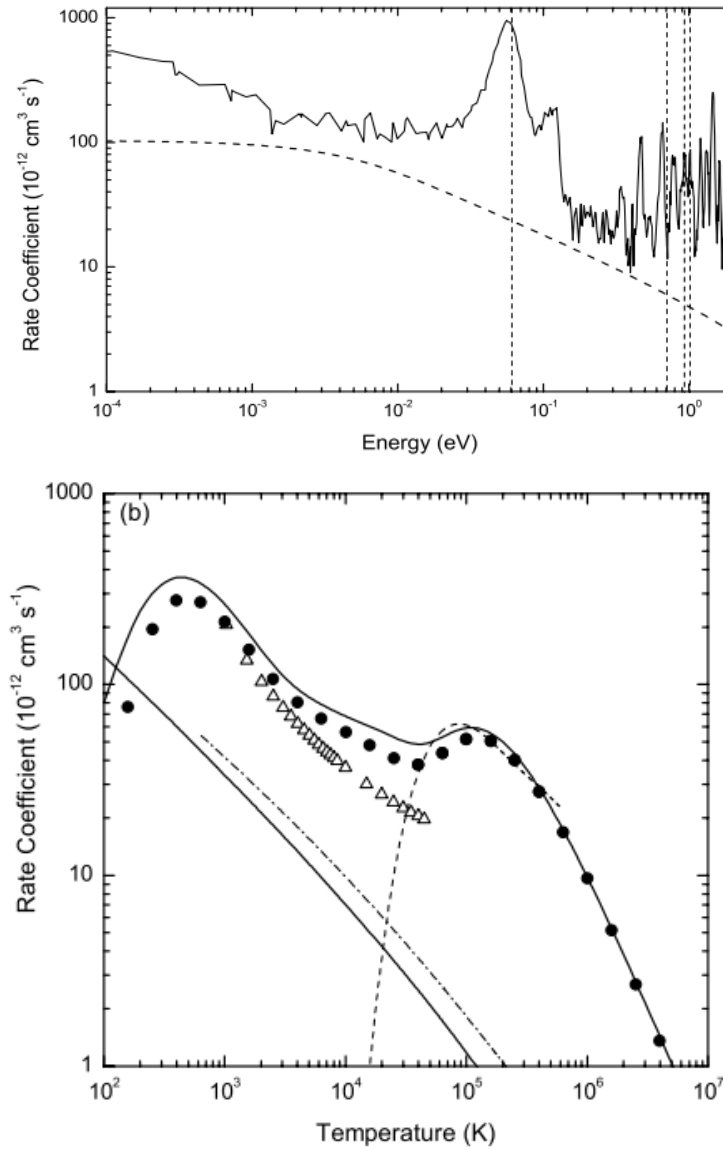
Figure 1.2: Figures taken from Fogle et al. [10]. Top figure shows the measured resonance spectrum for O^{4+}, as measured on the CRYING experiment. The dashed line shows the RR contribution, the solid line shows the DR contribution. Note the large single resonance at 60 meV. The lower figure shows the Maxwellian rate coefficient based upon the measurements. The solid line shows the rate coefficient with the resonance at 60 meV included, the dashed line shows the rate coefficient with this one resonance removed. The circles and the triangles show two theoretical calculations.

traditional beam experiments. It requires the presence of Rydberg electrons for the recombined ion, which provide a source of 'negative energy' electrons. Populating such Rydberg states would be common in plasma environments, but not in atomic beam experiments.

We propose in chapter 4 of this disseration an alternate method to prove the exisitence of below threshold recombination, namely to search for satellite lines from below threshold resonances. The below threshold resonances should undergo radiative decay and a Type I radiation would produce a satellite line that could be measured. Traditional satellite lines have been studied extensively [6], but this would be the first detection of a satellite line populated via below threshold recombination.

So two projects will be included in this dissertation about this topic. Chapter 4 is a description of the search for spectroscopic evidence of below threshold contributions to the dielectronic recombination. Chapter 5 focuses on identifing the ions with near threshold resonances and re-evaluating some of their DR rate coefficients.

1.2.1 A search for possible evidence of the existence of the below threshold Dielectronic Recombination

In chapter 4 of this dissertation we propose that below threshold satellite lines could be used as evidence of below threshold recombination. We describe here what satellite line emission is and how it could serve this purpose. Type I radiative decay in the DR process (i.e. core radiative decay) is the second step of the DR process and can create a photon called a satellite line. Consider the emission from a Be-like ion that is recombining via DR. The Be-like ion will have a strong spectral line corresponding to

$$1s^2 2s2p(^1P_1) \rightarrow 1s^2 2s^2(^1S_0) + h\nu_{res}. \tag{1.4}$$

Starting from the same initial state and considering a dielectronic capture one would have

$$1s^2 2s^2(^1S_0) + e \rightarrow 1s^2 2s 2p(^1P_1)nl \rightarrow 1s^2 2s^2(^1S_0)nl + h\nu_{sat} \quad . \tag{1.5}$$

Note that the frequence of this satellite line photon from the B-like system (ν_{sat}) is usually very close to the resonance line from the Be-like ion (ν_{res}). This is particularly true if the n-shell of the captured electron is high as it will only have a small effect on the wavelength of the photon emitted from the core radiative decay. For this reason it is called a satellite line. If such a satellite line could be detected from a doubly excited state that is below the ionization potential and can only be populated via below threshold recombination, it would serve as strong evidence of this new recombination mechanism. Thus, searching for satellite line emission from below threshold resonance transitions is an optimal way to directly verify the existence of the below threshold resonance DR.

An ideal candidate for searching for the below threshold satellite line should satisfy a number of conditions, these are described further in chapter 4. The main points of note are:

1. The doubly excited state must be just below the ionization potential and be embedded in the 'Rydberg continuum'. This will be described in more detail in chapters 4 and 5. This means that there is only a small energy window below threshold within which the double excited states can contribute to below threshold DR, usually less than 1 eV.

2. The satellite line must be strong, so for satellite lines the core radiative transition should be a dipole allowed transition.

3. The wavelength of the satellite line should be resolvable from the main resonance transition.

After checking different sequences of ions using NIST levels, C^{3+} satisfies all the conditions above and becomes an ideal candidate for this search. Due to the importance of knowing the exact wavelength of the satellite line photon, it is important that one has accurate energies for the below threshold double excited states. Thus our search was limited
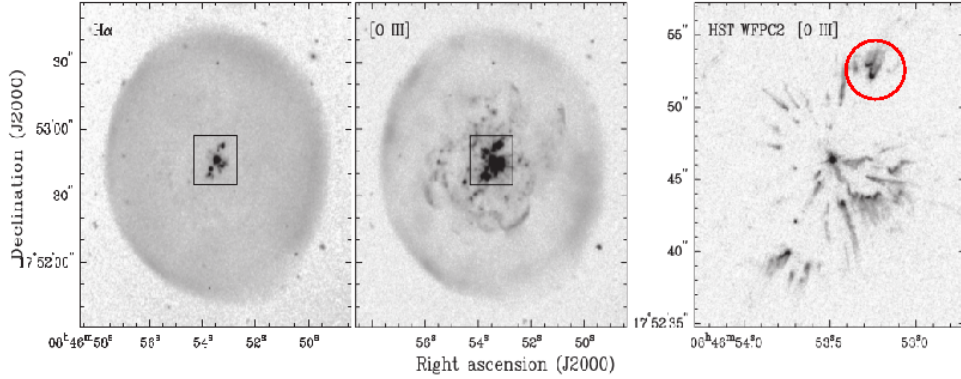
Figure 1.3: Images of Abell 30, figure taken from [13]. The left hand figure shows an Hα image and the center figure shows an O III image. Both of these were taken from ground based observations, the star can be seen in the center of the image. The right hand image shows an O III image with taken using HST WFPC2 and the F502N filter, the knot of interest is circled in red.

to systems with below threshold doubly excited states that had energies listed in NIST [14] with high accuracy. Due to the problems mentioned above, DR theory calculations would have too large an uncertainty to be used for spectroscopic accuracy.

Other conditions also have to be met for below threshold recombination to be possible. The density and temperature of the plasmas also should be in an appropriate range to satisfy the Condition (1) for the 'Rydberg continuum'. An ideal environment for the C^{3+} below threshold satellite line observation is an knot of plasma in the planetary nebula known as Abell 30. Thus our search will focus on this object. Figure 1.3 shows a visible image of this object, more details are presented in Chapter 4 and in Appendix C.

1.2.2 Identification of ions with near threshold resonance in Be-like and Li-like sequences and new Dielectronic Recombination rate coefficients for C^{3+} and Mg^{8+}

The ions with near threshold resonances are those whose DR rate coefficients in current database could be missing large contributions. To solve the problem, we should identify which ions have near threshold resonances. We define the near threshold as the cases where

there resonances falling in the energy region [-$\frac{Z^2}{20^2}$ Ryd:$\frac{Z^2}{20^2}$ Ryd] about the threshold. An important result of this work is the identification of which ions have no near threshold resonances; these can be used in current databases with confidence. The method used in this dissertation to identify the remaining ions that require new DR rate coefficient calculations via a check of the resonance positions. We use both the NIST energy level information and a DR resonance plot generated by the AUTOSTRUCTURE code [16, 17] to look for the cases with resonances in the aforementioned energy range. The NIST energies give us the most accurate resonance positions (but could be missing resonances) and the AUTOSTRUCTURE calculations can provide us with all of the resonances that we are interested in. We examine two sequences, Li-like and Be-like. From the list of cases with potential near threshold resonances, we select C^{3+} and Mg^{8+} to recalculate their DR rate coefficients by the inclusion of below threshold resonance contributions. The population distribution of the negative energy electrons is generated by the ADAS204 code [15]. The DR rate coefficients are calculated by the AUTOSTRUCTURE code [16, 17] for the above threshold resonance contribution and by a modified AUTOSTRUCTURE and a new post-processor for the below threshold resonances. More details are presented in Chapter 5 and Appendix C.

1.3 The importance of electron impact fine-structure excitation in low temperature astrophysical plasmas

When an electron interacts with an atom or ion, one possible process is that it excites this atom or ion. Fine-structure excitation of the levels within the ground term of atoms or ions is a particularly interesting case. They require very little energy to excite, and in environments without enough energy to populate the excited terms they then provide one of the few possible electron cooling mechanisms in plasma. Thus, such transitions act as one of the most important cooling mechanism in most interstellar environments, especially in those regions where electrons are the primary colliders [18]. This process is also important in the analysis of ultraviolet absorption lines. Also, fine-structure transitions are a useful diagnostic

tool for plasmas. Provided there are accurate excitation rate coefficients, various physical quantities, such as electron density and temperature can be inferred from the observed spectrum.

This physical process has been studied extensively. However, an important plasma parameter space has not received much attention, namely very low temperatures such as those in the interstellar medium. In chapter 6, we study this process for Ne^+ and Ne^{2+} using different R-matrix approaches [19]. The temperature that we are interested in extends to 10 K. After comparing different calculations, we recommend a set of data and evaluate an uncertainty on the excitation data.

Chapter 2

COMPARISON OF DIFFERENT QUANTUM MECHANICAL METHODS FOR INNER

SHELL PHOTO-IONIZATION FOLLOWED BY AUGER DECAY

This chapter considers different methods that can be used to calculate the dynamics of an Auger electron being ejected in the presence of a slow moving photo-electron. We are interested primarily in the Post Collision Interaction (PCI) and the effects on the energy and angular distributions of the photo-electron. We will first review earlier approaches, then describe and compare some methods that were developed as part of this project. The aim is to determine a summary of the region of validity of the wide range of methods that are used.

2.1 Background

The phenomenon of photo-ionization followed by Auger decay has been extensively studied in the past decades both theoretically [20–40] and experimentally [3, 4, 39, 41–51]. This is an interesting system to study for several reasons. Firstly, the Auger decay distorts the photo-electron energy distribution. The energy distribution becomes broader, the peak of the distribution decreases and is shifted to smaller energy because of the abrupt increase in the ion's charge after the Auger decay. This phenomenon is one example of post collision interaction (PCI) effects [26]. The PCI implies an account of an interaction between the photo-electron, the Auger electron and the ion field which varies during the Auger decay. This system is also interesting because the strong interaction between the two ejected electrons distorts the distribution of the angle between them. The two electrons interact with each other strongly, particularly when the electron emitted later in time has the larger energy and, thus, must pass the electron emitted earlier. A third reason for interest is

that the photo-electron which has been ionized may be recaptured to a bound state of the ion due to the PCI effect [52–61]. Recapture takes place only for low photo-electron energies.

In earlier studies, various two-body models, which include a classical model [27], a "shake-down" model [28, 29], a semi-classical model [30, 31], a quasi-molecular adiabatic model [32] and a quantum mechanical model [33–35], have been used to describe the interaction of the photo-electron with the ion field. Later, other models were used to approximately include a presence of a third particle - an Auger electron. Ogurtsov proposed a new version of a classical-model to deal with cases when the energies of all the electrons are comparable [36]. Junya Mizuno and co-workers studied this problem by solving the classical Coulomb three-body problem [37]. Niehaus' semi-classical model was reformulated in Ref. [38] to take into account the time it takes for the fast Auger electron to overtake the slow electron. The same effect was considered quantum mechanically in papers [62, 63].

Another group of quantum mechanical approaches [22, 23, 25] considers the problem as a three-body problem and takes into account the Coulomb interactions between three charged particles: two emitted electrons and a receding ion. These models are applied widely to study the PCI effects. Following convention, we refer to them as the SSE approach because they are based on the solution of the Stationary Schrödinger Equation. The SSE approach allows one to obtain the PCI distorted angular dependent cross sections. In this chapter we select the three most common models within the SSE approach to investigate: the Eikonal Approximation (EIA) [22], the Eikonal Approximation with Exact Account of the Electron-Electron interaction (EIAEIE) [23] and the Semi-Classical Approximation (SCA) [25]. The three models have been demonstrated to work well in calculating the energy distribution over a wide energy region, and one of the three, the eikonal approximation with exact account of the electron-electron interaction, has been found to calculate the angular distribution in good agreement with experiment, except for cases with low photo-electron energy.

As with any quantum mechanical three-body problem, the SSE approach has the limitation which comes from the approximate consideration for some of the interactions between

each pair of the particles. This approximation is more accurate when the photo-electron is energetic, but has larger uncertainties in systems with low photo-electron energy, and it is worse if the Auger electron energy is also low. Thus, an approach that can take into account all the interactions more precisely is needed for this energy region. The approach developed in Refs. [20, 21, 64] meets this requirement. It is based on the numerical solution of the time-dependent Schrödinger equation (the TDSE approach), free from any physical sim-plification in interactions between the emitted particles and restricted mainly by numerical implementation. The aim of this paper is to check the applicability of this recently developed approach [20, 21, 64] (particularly to show its use in the low photo-electron energy region) and test its consistency with the SSE approach. To achieve this aim, we compare the two most important physical quantities in studying the PCI effects, the photo-electron energy and angular distributions, calculated by the TDSE and SSE approaches. Our comparisons are for both low and higher photo-electron energies and we also compare some of our calcu-lations in the low photo-electron energy region with experimental data. Note that carrying out the calculations within the TDSE method and using the numerical implementation of the method discussed we have restricted ourselves with some approximations which simplify the calculation dramatically and will be discussed in Sections 2.2 and 2.4. Thus, by com-bining the TDSE and SSE approaches, the PCI effects can be accurately calculated over an extended range, including near threshold photo-electron energies.

The energy and angular distributions are mainly determined by three parameters; these are the excess energy of the incident photon above the threshold which is the photo-electron energy, E_1, the Auger electron energy, E_2, and the energy width of the inner shell vacancy, Γ. E_1 can be adjusted by changing the photon energy, the energy released by the electron which fills the vacancy determines E_2, and Γ is proportional to the inverse of the inner vacancy life-time. So experimentally, we can choose different values for E_1 while E_2 and Γ are determined by the atomic species. We perform calculations of nine cases in our paper: six of them are real cases for the system of Ne 1s photo-ionization followed by KLL Auger

decay (where $\Gamma = 0.01$ and $E_2 = 29.4$ [4]) and the other three are fictitious cases which have no direct experimental significance but will be very helpful in testing the accuracy of the TDSE approach and highlighting its advantage at low photo-electron energy.

The chapter is organized as follows: in Sec. 2.2 we introduce the TDSE approach briefly; the SSE approach models are discussed in Sec. 2.3; in Sec. 2.4, we compare the results calculated by the TDSE and SSE approaches, and we also compare some of these theoretical results with experimental data; the last section contains our conclusion.

Atomic system units are used throughout this chapter unless stated otherwise.

2.2 A brief introduction to the TDSE approach

The whole process of the inner shell photoionization with subsequent Auger decay can be divided into two main steps, before and after the Auger decay. Only the photoelectron (e_1) is emitted from the nucleus before the Auger decay, so the Hamiltonian for the first step is $H_1 = p_1^2/2 + V(r_1, t)$. After the Auger decay, the Auger electron (e_2) is also detached from the ion. The Hamiltonian will be composed of three parts, and can be expressed as $H = H_1 + H_2 + H_3$, where $H_2 = p_2^2/2 + V(r_2, t)$ is for e_2 and $H_3 = 1/r_{12}$ is for the interaction between e_1 and e_2.

The method applied to study this problem in our projects is referred to as the Time-Dependent Schrödinger Equation (TDSE) method [20, 21]. This method is based on the time-dependent close coupling (TDCC) method [64–66] with two main modifications. One is that the technique for the wave function propagation in the TDSE method [20, 21] is an implicit split-operator method, while in the TDCC method the wave function is updated with the leapfrog algorithm [64–66]. Instead of a multipole expansion, the $\cos(\theta_{12})$ in the e-e interaction Hamiltonian operator $1/r_{12}$ is evaluated with a discrete variable in the TDSE method, which is the second modification.

We use two Schrödinger equations to describe the process before and after the Auger decay in the TDSE method. The equation for the process before the Auger decay is a

time-independent Schrödinger equation with an extra term for the photon absorption:

$$(E_1 + i\frac{\Gamma}{2} - H_1)F_1 = D\phi_g \tag{2.1}$$

where E_1 is the initial photo-electron energy, $D\phi_g$ is the dipole operator acting on the orbit that absorbs photon, F_1 is the photo-electron wave function and Γ is the width of the inner vacancy (it is inverse of the life time the inner hole). The potential in H_1 is taken as $-1/r_1$ and $D\phi_g$ is taken to be $r_1 e^{-r_1^2}$, a simple short-range function. The expressions for H_1 or $D\phi_g$ is not in an exact form, but have little influence on the physical quantities in which we are interested. This is because because the important interactions take place far outside the core region. Γ is proportional to the inverse of the inner vacancy's life-time. The wave function of the photo-electron, F_1, has the form of a damped continuum wave at energy E_1; the spatial extent of F_1 increases when E_1 increases or Γ decreases.

Equation (2.2) is the time-dependent Schrödinger Equation with source term that describes the process after the Auger decay. The two-electron wave function $\Lambda(\mathbf{r}_1, \mathbf{r}_2, t)$ is the solution of

$$i\frac{\partial \Lambda}{\partial t} - H\Lambda = S(t)F_1(r_1)F_2(r_2) \tag{2.2}$$

where $S(t)$ is the strength of the source, $F_1(r_1)$ and $F_2(r_2)$ is the source for the photoelectron and Auger electron, respectively. We use an expression from [21] $S(t) = 1/\{1 + \exp[10(1 - 5t/t_f)]\}$ where t_f is the final time of the calculation [21]; this form is chosen to make $S(t)$ start at ~ 0 at t=0 and smoothly transit to 1 well before t_f. The potential in H_1 and H_2 is taken to be $-2/r$, because the ion is double-charged after the Auger decay. We use the wave function before the Auger decay $F_1(r_1)$ as the source term of e_1. For e_2, the continuum wave function at the Auger electron's initial energy E_2 is used as the source term.

The two-electron wave function Λ can be expressed as:

$$\Lambda = \sum_{\ell_1, \ell_2} R_{\ell_1 \ell_2}^{LS}(r_1, r_2, t) \sum_{m_1, m_2} C_{m_1 m_2 0}^{\ell_1 \ell_2 L} Y_{\ell_1 m_1}(\Omega_1) Y_{\ell_2 m_2}(\Omega_2) \tag{2.3}$$

16

where $C^{\ell_1 \ell_2 \ell_3}_{m_1 m_2 m_3}$ is a Clebsch-Gordan coefficient, Ω is the solid angle and $Y_{\ell m}(\Omega)$ is a spherical harmonic. We will approximately consider that e_1 and e_2 have the same angular momentum in Chapters 2 and 3, $\ell_1 = \ell_2 = \ell$. Then Eq. (2.3) is simplified as:

$$\Lambda = \sum_{\ell} \frac{(-1)^{\ell}}{\sqrt{4\pi}} R_{\ell}(r_1, r_2, t) Y_{\ell 0}(\cos \theta_{12}) \tag{2.4}$$

where θ_{12} is the relative angle between the two ejected electrons.

We can extract different physical properties from the two-electron wave-function Λ. The time-dependent position of each electron can be obtained from Λ. At early times, the Auger electron travels behind the photo-electron. After a certain time, the Auger electron will be at large radial distance from the nucleus than the photo-electron and will continue to large distance, perhaps changing the direction of the photo-electron.

With the total wave-function Λ, the energy distribution P_{ϵ_i} can be calculated:

$$A_{\ell}(\epsilon_1, \epsilon_2) = \int \int dr_1 dr_2 \phi^*_{\epsilon_1 \ell}(r_1) \phi^*_{\epsilon_2 \ell}(r_2) R_{\ell}(r_1, r_2, t) \tag{2.5}$$

$$P_{\epsilon_i} = \int d\epsilon_j \sum_{\ell=0}^{\ell_{max}} |A_{\ell}(\epsilon_1, \epsilon_2)|^2 \tag{2.6}$$

where $i, j = 1, 2$ and $i \neq j$ (1 and 2 correspond to the photo-electron and Auger electron, respectively.), ϵ_i is always positive energy, P_{ϵ_i} is the energy distribution, and $\phi_{\epsilon_i \ell}(r_i)$ is electron continuum eigen wave function; for the photo-electron, the continuum wave is evaluated using a potential of $-2/r$ while for the Auger electron the potential is $-1/r$.

We can also calculate the angular distribution of the electrons with positive energy. The angle of interest is the relative angle between the two electrons. The angular distribution, $D_k(\cos \theta_{12})$, can be calculated:

$$D_k = \int \int d\epsilon_1 d\epsilon_2 \left| \sum_{\ell=0}^{\ell_{max}} (-1)^{\ell} Y^*_{\ell 0}(\cos \theta_{12}) A_{\ell}(\epsilon_1, \epsilon_2) \right|^2 \tag{2.7}$$

17

One point that deserves emphasis is that the angular distribution D_k only counts electrons with positive energies and those that are captured to the bound states during the Auger process are excluded.

One particular interesting quantity to study is referred to as the PED which is a probability distribution for the photo-electron energy and relative angle. It can be calculated via:

$$PED = \int d\epsilon_2 \left| \sum_{\ell=0}^{\ell_{max}} (-1)^\ell Y_{\ell 0}^*(\cos\theta_{12}) A_\ell(\epsilon_1, \epsilon_2) \right|^2, \tag{2.8}$$

The other quantity is the angular momentum distribution for the ionized photo-electrons P_ℓ which can be calculated via:

$$P_\ell(t) = \int d\epsilon_2 \int d\epsilon_1 \left| A_\ell(\epsilon_1, \epsilon_2) \right|^2. \tag{2.9}$$

Figure 2.1 displays the angular momentum distribution at different times. The distribution is concentrated in $\ell = 0$ at early times. With the increase of time, the probability for larger angular momentum increases because the interaction between the two electrons becomes stronger. The P_ℓ needs to become small for several ℓ before ℓ_{max}.

We use all of the physical quantities to check the convergence of the calculation. For example we can check if the calculation converges with respect to the time step, the spatial grid width, the energy grid width and the number of angular momenta. Usually larger energy requires a smaller spatial step to achieve convergence because the spatial grid has to be much less than the wave length of the Auger electron. We also find that cases with a stronger interaction require more angular momenta. The number of angular momenta to get converged results is 70 for the case ($E_1 = 0.3, E_2 = 1.0, \Gamma = 0.02$), and for other cases such as ($E_1 = 0.3, E_2 = 29.4, \Gamma = 0.01$) 15 are sufficient for convergence. The interaction between the two electrons is stronger when they have comparable velocities. Also, we can check if these quantities are converged with respect to time. We extend the calculation time
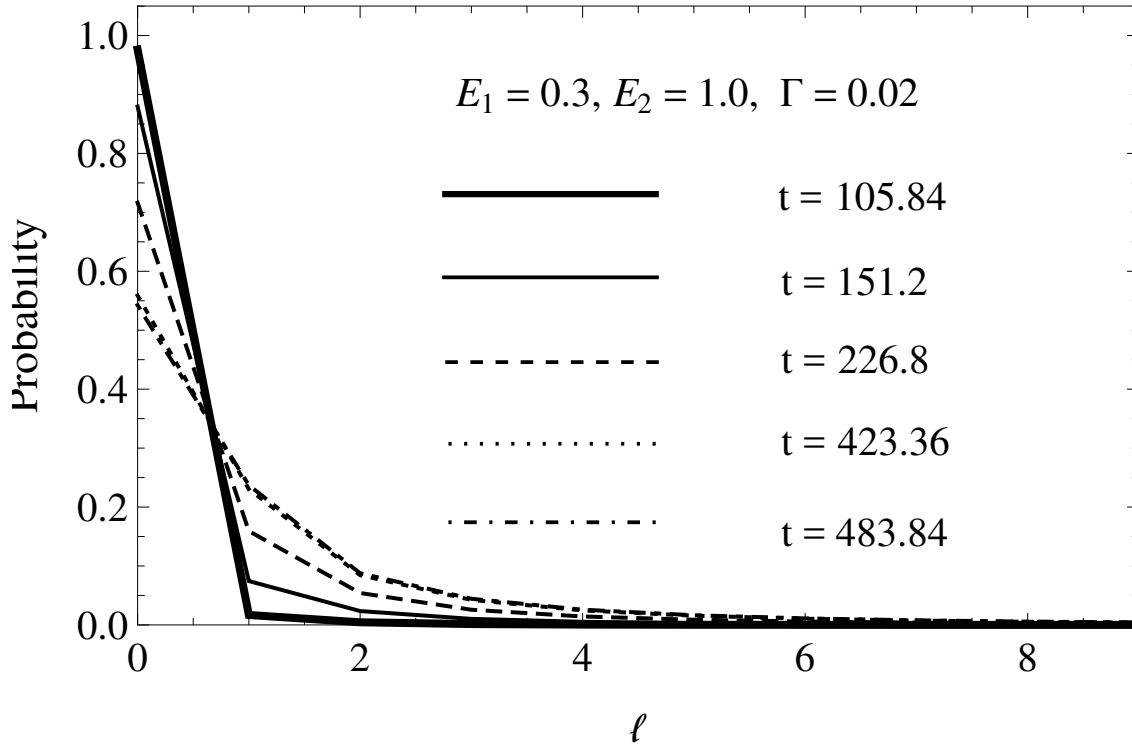
Figure 2.1: The angular momentum distribution at different times. The wave-function is mostly at $\ell = 0$ at early time because the two ejected electrons start with zero angular momentum. At later times, the angular momentum of each electron can increase due to the electron-electron interaction. After $t = 423.36$, the Auger electron passes the photo-electron and thus the angular momentum distribution stays the same.

t_f until the physical quantities are no longer changing. Usually, we can obtain converged photo-electron energy and angular momentum distributions at early times in the simulation. It requires more time for the angular and Auger electron energy distributions to converge.

The advantage of the TDSE approach lies in its accuracy in calculating the different physical quantities. This is a fully quantum mechanical method, and all of the interactions between each pair of charged particles are considered without any simplification which is very important when the two emitted electrons propagate with low energies. The work in Ref. [21] displays the angular distribution comparison between the calculated and experimental data in the system of Neon 1s photo-ionization followed by Auger decay with low photo-electron energy but high Auger electron energy. The good agreement in the comparison demonstrates the validity of this theoretical method in the low photo-electron energy region. Experimental data for cases with both the photo-electron and Auger electron in low energy region are needed to demonstrate the importance of considering all the interactions precisely.

2.3   Models of SSE approach

We will compare results of calculations of the angular and the energy distributions within the TDSE approach with results using the SSE approach. The models which have taken into account the interaction between the receding ion, the photo- and Auger electrons and were evaluated within the SSE approach are the eikonal approximation (EIA) [22], the eikonal approach with account of the exact interaction between the emitting electrons (EIAEIE) [22, 24], and the semi-classical approximation (SCA) [25]. All these models present the amplitude of the process to be proportional to the overlap integral between the photo-electron wave functions calculated before and after the Auger decay:

$$A \sim \left\langle \psi_k \middle| \psi_\varepsilon' \right\rangle \tag{2.10}$$

where $\psi_k(\vec{r})$ is the wave function of the photo-electron with momentum $\vec{k}$ moving in the field of the double charged ion and the Auger electron, $\psi'_\varepsilon(\vec{r})$ (the F_1 in the TDSE approach) is the photo-electron wave function moving in the field of the single charged ion with the complex energy $\varepsilon - i\,\Gamma/2$. These functions are calculated via the solution of the stationary Schrödinger equations.

Evaluating an amplitude within the EIA approximation, it is assumed that the interaction between each pair of charged particles (the photo-electron with the ion and the photo-electron with the Auger electron) occurs mainly at large distances where the kinetic energy is much more than the potential energy of the interacting particles, $W_{kin} \gg W_{pot}$. This condition leads to the limitation of the energies of the slow photo-electron, E_1:

$$E_1 \gg \Gamma^{2/3} \, (E_0/2)^{1/3} \tag{2.11}$$

where E_0 is the atomic unit of energy. On the other hand, the case of similar energies for the photo- and Auger electrons when they are emitted at small relative angles violates the condition of the applicability of the EIA approximation. Note that the inaccurate accounting of the electrons' interaction leads to the impossibility of calculating the total PCI distortion factor for angular distribution of the emitted electrons (when it is integrated over all the energies of the emitted electrons) [24].

The EIA approximation was extended to the case when the emitted electrons have comparable velocities and are ejected at small relative angles. In this case, the interaction between the photo- and Auger electrons has to be taken into account more precisely. This has been done within the EIAEIE approach [23] where the movement of the photo-electron is considered in the eikonal approximation but the Coulomb interaction between the emitted electrons is taken into account exactly within the quantum mechanical approach. The EIAEIE approach allows one to calculate the energy and angular distributions of the emitted

electrons for a wide range of energies and angles for the ejection of the photo- and Auger electrons, except from the cases where the condition in Eq. (2.11) breaks down.

The semi-classical approach, SCA, uses the WKB wave functions for calculating of the overlap integral and leads also to the angular dependent PCI distortion cross section [25]. It can be applied to the case of low energy photo-electron ejection which lies beyond the condition in Eq. (2.11). However, the energy distribution calculation within the SCA method is faced with another restriction, which is

$$0 < v_1/|\mathbf{v}_2 - \mathbf{v}_1| < 1 \tag{2.12}$$

where $\mathbf{v}_1$, $\mathbf{v}_2$ are the velocities of the photo- and Auger electron, respectively. If the relative velocity of the emitted electrons is small and they lie in the region where $v_1/|\mathbf{v}_2 - \mathbf{v}_1| > 1$, the SCA approach can not be used. This restriction is connected with the fact that the point of the stationary phase (this method is used for evaluation of the overlap integral) in the region considered is going to infinity and the stationary phase method breaks down.

An advantage of the SSE approach is the fact that all three models considered here give the analytical expressions for the amplitudes and cross sections that can be used for analysis and calculation of the energy and angular distributions in a wide region of energies and angles of electron emission. A numerical implementation of these formulae is straightforward and reduces to the calculation of some special functions in the complex plane. Note that calculations within the considered models of the SSE approach carried out in the region of their applicability agree quite well with measurements both of energy distributions (see e.g.[39]) and of the angular distributions [44, 45, 49].

Some further examples of the levels of agreement are given here. The line shapes of the 2.7 eV 4d photo-electrons in Xe (Γ= 110 meV) calculated within the EIA approach agree very well with the measured energy distributions in papers [39] and [67]. Also the energy distributions of the 2p photo-electrons in Ar ($\Gamma = 118$ meV) calculated by the EIA model agree

Mthod	Condition	Valid regime
EIA	$E_1 \gg \Gamma^{2/3} (E_0/2)^{1/3}$	High energy regime and the two electrons are ejected at different directions.
EIAEIE	$E_1 \gg \Gamma^{2/3} (E_0/2)^{1/3}$	High energy regime
SCA	$0 < v_1/|\mathbf{v_2} - \mathbf{v_1}| < 1$	Low photo-electron energy regime or large relative velocity beteen two ejected electrons
TDSE	Satisfy computational resources	Low and high enenrgy regime

Table 2.1: Condition summary for different methods

well with the measured ones for the excess photon energies 3 eV, 9 eV and 12 eV but dis-agree for the excess energy 0.85 eV [51]. However, the calculation within the SCA approach [40] shows good agreement with experimental data in this case. The angular dependent energy distributions of the 30.5 eV electrons in Xe 4d-ionization followed by the [1]N_5-$O_{23}O_{23}$ Auger decay were measured in coincidence with the Auger electrons [44, 45] and show good agreement with the calculation within the EIA approach. The angular distribution of the 17 eV 4d-photo-electrons in Xe was measured in coincidence with the 30 eV N_5-$O_{23}O_{23}$ Auger electrons [49] and shows good agreement with the calculations within the EIAEIE approach. The angular distribution of the 13.5 eV 2s photo-electrons emitted due to the resonance photoionization in Neon and followed by the Auger decay ($Ne^{+*}(2s2p^5(^3P)3p(^2S))$ $\rightarrow Ne^{2+}(2s^22p^4(^1D))+e_A$, where the Auger electron has similar energy to the photo-electron) was calculated by the EIAEIE approach in Ref. [47], and the agreement between the calcu-lations and measurements is quite reasonable.

Table 2.1 gives a brief summary of the applicability of different methods.

---

[1]This is a spectroscopic notation where principle quantum numbers are identified by letters. The symbols for n=1 ,2, 3 ... are K, L, M .... In the notation, the first letter is the initial core hole location (initially location of photo-electron), the second letter is the initial location of relaxing electron and the third letter is the location of second hole (initial location of Auger electron). So the notation N_5-$O_{23}O_{23}$ represents that a photon creates a hole at 4d, an electron at 5p fills in this hole and transfer its extra energy to another electron in 5p which will be ejected.

2.4 Comparison between TDSE and SSE approaches

In this section, we compare the photo-electron energy and angular distributions of several cases calculated by the two different quantum mechanical approaches: TDSE and SSE. This comparison will highlight agreement and disagreement of results obtained by the various methods.

Note that some approximations are made in the TDSE approaches. For example, we use $-Z/r$ as the potential in the Hamiltonian. This approximation is accurate when the photo-electron travels far from the nucleus before it interacts with the Auger electron. For very low photo-electron energy ($E_1 \approx 0$), the approximation will not be as accurate. We use a different potential in the calculation:

$$-(Z + (10 - Z)\exp(-r/r_a))/r \qquad (2.13)$$

where r_a is atomic radius, and it is 0.71 for Neon. And we find that the results of this potential are the same as those of the potential $-Z/r$ except for the situation when the initial photo-electron energy is very close to 0. Another approximation is that the expressions for $D\phi_g$ in Eq. (1) and $F_2(r_2)$ in Eq. (2) are replaced by two simple short-range functions. As with the simple approximation to the Hamiltonian, this approximation breaks down for zero initial photo-electron energy or large Γ. We also assume that both ejected electrons start with 0 angular momentum. This approximation is not essential, but it simplifies the calculation dramatically and allows us to use the available computer capacities and carry out the calculation with in a reasonable time. This restriction means that cases with non-zero total angular momentum L are not treated in the current TDSE calculations. However, we expect the general trends for other total angular momenta to be similar to those in this paper because the electrons are at large distance when the interaction occurs. We plan to perform calculations with different total angular momentum in future work by using more refined numerical methods. The main limitation of the TDSE approach is computer

capacity. If an electron's energy is large, a greater number of points for the radial grid is needed to get a converged result; if two electrons have comparable velocities, more angular momenta are required in the calculation. So the current version of the TDSE code becomes computationally intensive when both the ejected electrons have very large velocities or have large and comparable velocities.

The SSE approach contains three different approximations to calculate the energy distribution. The first is the EIA approximation which works for cases when the two ionized electrons have large and different velocities and the relative angle between them is not too small. When the two ionized electrons have large and comparable velocities or the Auger electron is launched near the direction of the photo-electron, the second approximation, EIAEIE, should be applied. The condition in Eq. (2.11) can be used to test if the EIA or the EIAEIE approximation is accurate. The third approximation is the SCA approximation which is accurate for low excess photo-electron energy. The condition in Eq. (2.12) has to be satisfied for this semi-classical approximation. In this paper, only the EIAEIE approximation is applied to calculate the angular distribution. The EIA approximation fails in the calculation of the angular distribution because the interaction between the two ejected electrons is the main reason for the distortion in the angular distribution [24]; the EIA approximation is used when three particles are far apart and their trajectories are straight-lines, so the angular distribution calculated by EIA approximation has little PCI distortion. The reason for not calculating the angular distribution using the SCA approximation is similar, because the interaction between the two ejected electrons is not fully considered in this approximation either. The PCI distortion factor for the angular distribution given by the EIA approach was shown to be 1 (see [24]), and we have a similar conclusion for the SCA approximation, which has been checked by direct numerical calculation. Thus we can compare with the EIAEIE results because it should be the most accurate for the

Case name	Photo-electron energy (E_1)	Auger electron energy (E_2)	Auger width (Γ)
Cases for Energy distribution			
Case 1A	0.0735	2.0	0.01
Case 2A	0.1	29.4	0.01
Case 3A	0.5	29.4	0.01
Case 4A	0.3	1.0	0.02
Cases for angular distirbution			
Case 1B	0.0735	2.0	0.01
Case 2B	0.0735	29.4	0.01
Case 3B	0.05	29.4	0.01
Case 4B	0.3	29.4	0.01
Case 5B	0.4	29.4	0.01
Case 6B	0.5	29.4	0.01
Case for experiment comparison			
Experiment case	0.05	29.4	0.01
Case for diferent range of integration for the angular distribution			
Different range intergrartion case	0.5	2.0	0.02

Table 2.2: All the cases studied in this chapter

For the system studied here, a close comparison between theoretical methods, and with experiment, is critical in developing a full picture of the dynamics. In the following subsections we compare a range of theoretical calculations. At the end of each section we also compare with the available experimental data. Table 2.2 provides a list of all the cases studied in this chapter.

2.4.1   Comparison of the photo-electron energy distribution

First we examine the photo-electron energy distribution. Four typical cases are selected to discuss the similarity and distinction of results obtained by the various approaches. We will also investigate the differences between the results, relating them to the restrictions of these approaches.

The first two cases are Case 1A ($E_1 = 0.0735, E_2 = 2.0, \Gamma = 0.01$) and Case 2A ($E_1 = 0.1, E_2 = 29.4, \Gamma = 0.01$). For Case 1A and 2A, the right hand side of the condition in Eq. (2.11) is $0.01^{2/3}(1/2)^{1/3} \approx 0.0368$. $E_1 = 0.0735$ in Case 1A and 0.1 in Case 2A. Neither of
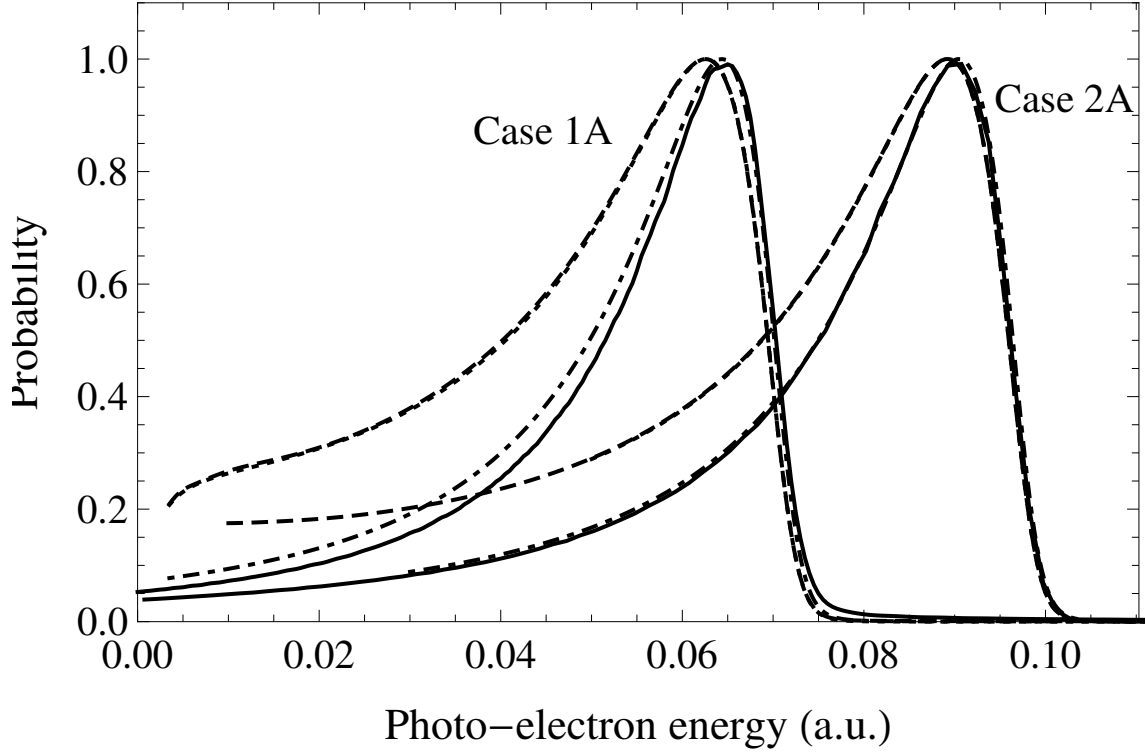
Figure 2.2: The photo-electron energy distribution comparison of different approaches for two cases. The left curves are for Case 1A ($E_1 = 0.0735, E_2 = 2.0, \Gamma = 0.01$), and the right curves are for Case 2A ($E_1 = 0.1, E_2 = 29.4, \Gamma = 0.01$). For both cases the dotted line is the calculation of the EIA approximation of the SSE approach, the dashed line is of the EIAEIE approximation, the dot-dashed line is of the SCA approximation and the solid line is the result of the TDSE approach.

the two values is much larger than 0.0368. **So the EIA and EIAEIE approximations should not work well.** However, the value of $v_1/|\mathbf{v_2} - \mathbf{v_1}|$ in the condition in Eq. (2.12) is approximately $0.161 - 0.237$ for Case 1A and $0.055 - 0.062$ for Case 2A. **The two ranges are both between 0 and 1, and the SCA approximation should give accurate results.** As shown in Fig. 2.2, the PCI distortion in the EIA and EIAEIE approximations is much larger than that in the TDSE approach or the SCA approximation: the shift of the distribution maximum is larger and the left wing of the distribution broadens strongly. This fact is connected with the violation of the condition in Eq. (2.11) in the near threshold region and with underestimation of the potential energy. It leads to a stronger influence of the ionic field variation on the photo-electron propagation, and consequently on the PCI distortion. As the photo-electron energy decreases, the discrepancy between the calculations increases. The disagreement between the results within the EIA and SCA approximations was first noted in Ref. [25]. For both cases, the results of the SCA approximation agrees much better with that of the TDSE approach. The agreement in Case 2A is better than that in Case 1A, and the discrepancy lies in the left wing of the distribution in both cases. These small disagreements can be connected with the approximations which were used in the evaluation of the SCA approximation [25]. The results of the EIA and EIAEIE approximations almost coincide in these two cases. Because the two electrons' velocities are not very close to each other, considering the interaction between the two emitted electrons exactly (or not) makes little difference to the results.

The other two cases selected to discuss the photo-electron energy distribution are Case 3A ($E_1 = 0.5, E_2 = 29.4, \Gamma = 0.01$) and Case 4A ($E_1 = 0.3, E_2 = 1.0, \Gamma = 0.02$). The condition in Eq. (2.11) is satisfied for both cases: $0.5 \gg 0.0368$ for Case 3A and $0.3 \gg 0.0585$ for Case 4A. The value of $v_1/|\mathbf{v_2} - \mathbf{v_1}|$ is approximately $0.115 - 0.150$ for Case 3A and $0.354 - 1.211$ for Case 4A. Case 3A fully satisfies the condition in Eq. (2.12) but Case 4A fails for some angles ($0.913 < \cos\theta_{12} < 1$) . In Case 3A (the right part of Fig. 2.3), the three different SSE approximations give the same photo-electron energy distribution because
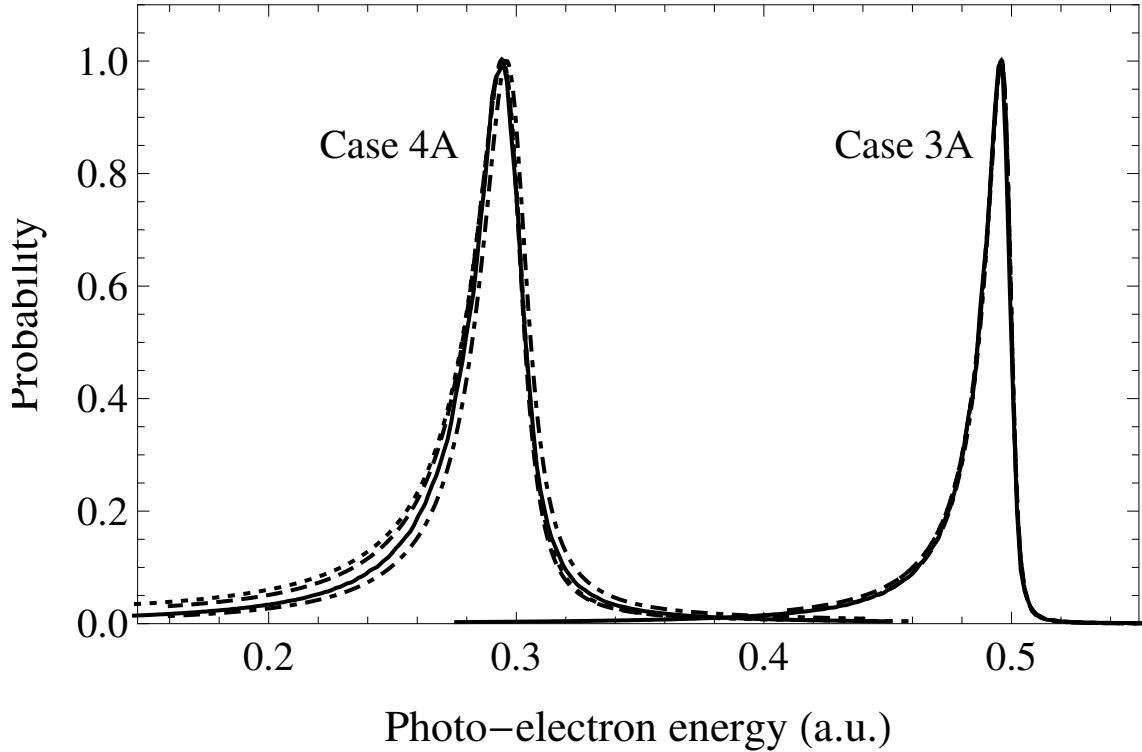
Figure 2.3: The photo-electron energy distribution comparison of different approaches for two cases. The left curves are for Case 4A ($E_1 = 0.3, E_2 = 1.0, \Gamma = 0.02$), and the right curves are for Case 3A ($E_1 = 0.5, E_2 = 29.4, \Gamma = 0.01$). For both cases the dotted line is the calculation of the EIA approximation of the SSE approach, the dashed line is of the EIAEIE approximation, the dot-dashed line is of the SCA approximation and the solid line is the result of the TDSE approach.

both the conditions in Eqs. (2.11) and (2.12) are satisfied, and they agree quite well with the TDSE approach. In Case 4A (the left part of Fig. 2.3), the four results are also close although none of the SSE approximations agree perfectly with the TDSE result. The result of the TDSE approach agrees best with that of the EIAEIE approximation because the condition in Eq. (2.12) is not satisfied for some angles and the two electrons have comparable large velocities. The small difference between the TDSE approach and the EIAEIE approximation also happens in left wing of the distribution because the condition in Eq. (2.11) is not satisfied in the low energy range.

Our theoretical findings can be verified by the available measurements [4]. Fig. 2.4 presents the theoretical and experimental energy distribution comparison for the case $E_1 = 0.05, E_2 = 29.4, \Gamma = 0.01$. The results calculated within the EIA approximations (the thin solid-line) and EIAEIE approach (the dashed-line) coincide with each other, but significantly deviate from the experimental data [4] (symbolized by dots in Fig. 2.4). This is what we expected because this case violates the condition in Eq. (2.11) (E_1 is comparable with the value $0.01^{2/3}(1/2)^{1/3} \approx 0.0368$). However, the condition of Eq. (2.12) is satisfied (the value of $v_1/|\mathbf{v}_2 - \mathbf{v}_1|$ is $0.0396 - 0.043$), and the result calculated by the SCA approximation should be more accurate. The results from the TDSE method (the thick solid-line) and SCA approximation (the dot-dashed-line) agree with each other. They also fit well with the experimental data, and the agreement in the low energy region is better than that in the higher energy region. The difference between the experimental data and the SCA or the TDSE curve may be caused by a yield of occasional electrons (via the capture and re-emission of slow photo-electrons) which are recorded experimentally but not included in the calculations here. Another possible reason for this small disagreement may be associated with the photon energy resolution which is also not included in the calculation. For the resolution of the electron spectrometer, we simulate this function via a Gaussian with permanent FWHM = 170 meV [4] for all energies of the calculated range. However, the real experimental function
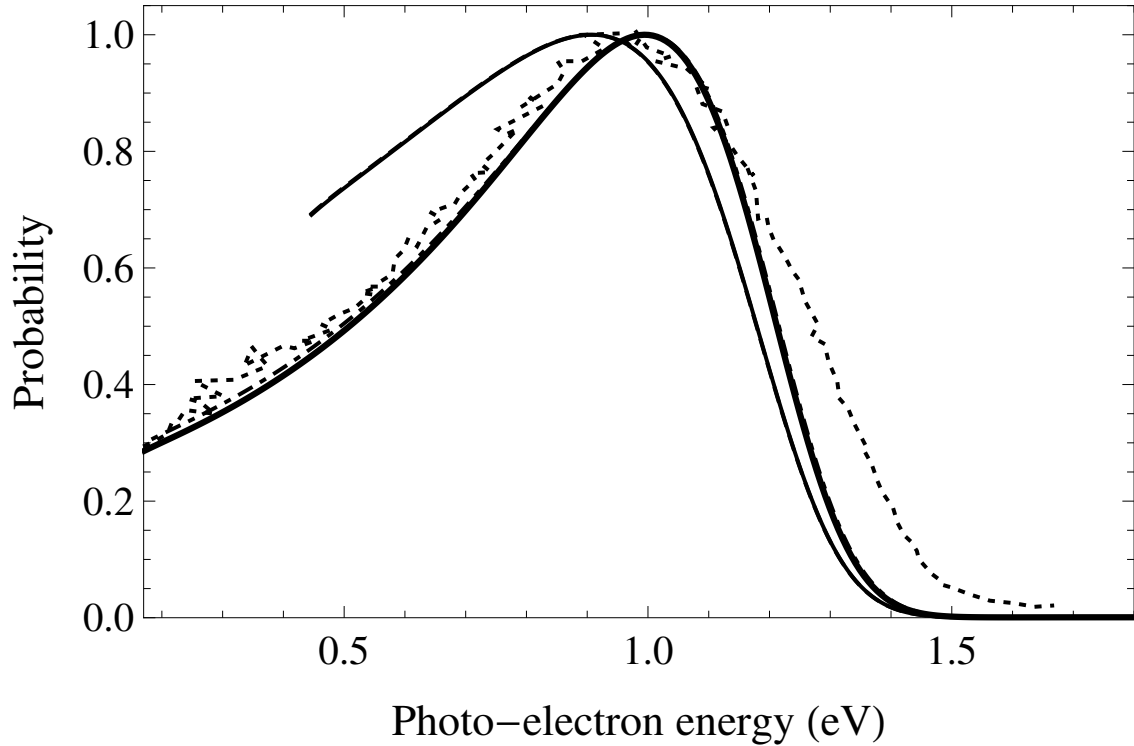
Figure 2.4: The photo-electron energy distribution comparison of theoretical calculations and experimental data for the case of 1s-photoionization of Ne ($E_1 = 0.05, E_2 = 29.4, \Gamma = 0.01$). The dotted line is for the experimental measurement extracted from Ref. [4], the thin solid line for the calculation of the EIA approximation of the SSE approach, the dashed line is of the EIAEIE approximation, the dot-dashed line is of the SCA approximation and the thick solid line is the result of the TDSE approach.

may differ from the function we used and have a more complicated form. That is also a possible reason for the disagreement.

2.4.2 Comparison of the angular distribution

To investigate the angular distribution, we selected cases designed to compare the TDSE approach and the EIAEIE approximation. Any difference between the two approaches should be related to the photo-electron energy E_1 and the Auger width Γ because of the condition in Eq. (2.11). However, we found that the TDSE and EIAEIE approaches gave closer results for larger Auger electron energy which suggests an approximation beyond that captured by the condition in Eq. (2.11).

Cases with low excess photo-electron energy can not satisfy the condition in Eq. (2.11), so the angular distribution calculated by the EIAEIE and TDSE approaches should be expected to have a notable difference. With the increase of the photo-electron energy, the agreement between the two approaches becomes better. For cases with low photo-electron energy, if the Auger electron energy is also small, the agreement between the two methods is worse, compared to cases with larger Auger electron energy. Fig. 2.5 shows the comparison of the angular distribution for the three cases. The solid-lines are the results of the TDSE approach and the dotted-lines are the results of the SSE approach. Case 2B ($E_1 = 0.0735, E_2 = 29.4, \Gamma = 0.01$) has the same Γ and E_2 as Case 3B ($E_1 = 0.05, E_2 = 29.4, \Gamma = 0.01$), but a different E_1. For these two cases, the test for the condition in Eq. (2.11) is $0.0735 \gg 0.0368$ for Case 2B and $0.05 \gg 0.0368$ for Case 3B. Neither of them satisfies the condition, and as a result, the SSE approach does not agree very well with the TDSE approach. Case 2B has the same Γ and E_1 as Case 1B ($E_1 = 0.0735, E_2 = 2, \Gamma = 0.01$), but quite different E_2. The condition in Eq. (2.11) fails in both cases. However, the uncertainty of EIAEIE in Case 1B is much larger than that in Case 2B because the Auger energy is much smaller.

32
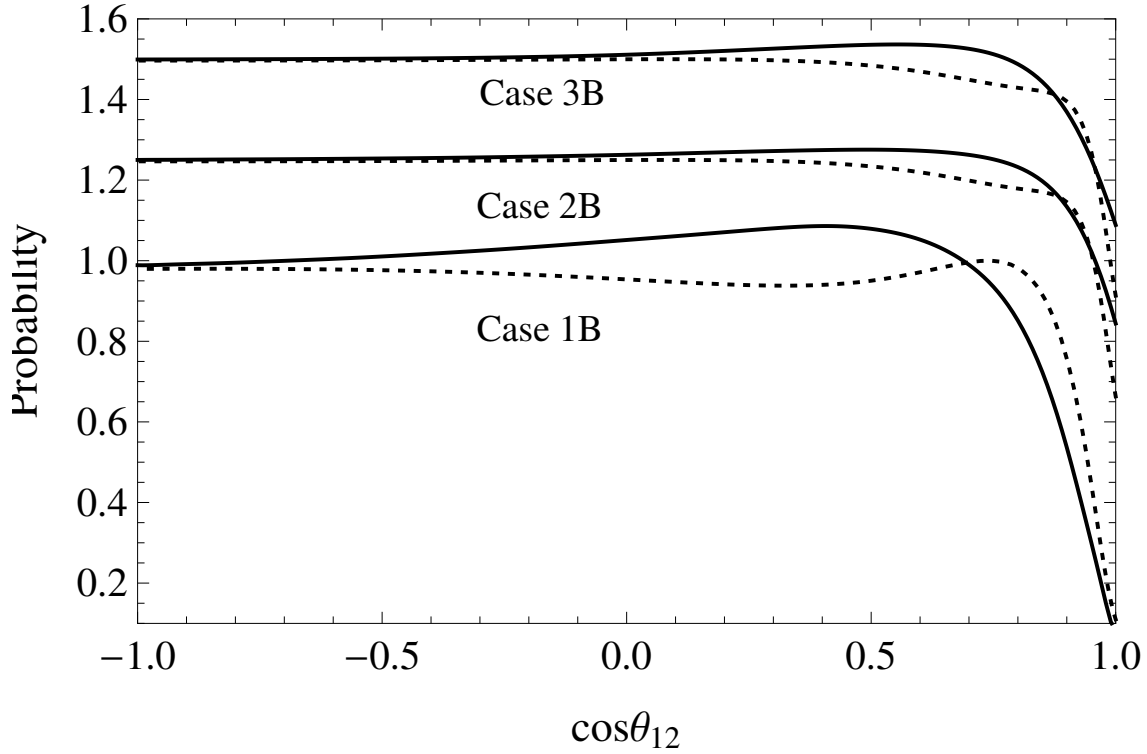
Figure 2.5: The angular distribution comparison of the two approaches for three cases. The solid lines of the three cases are the calculations of the TDSE approach, and the dotted lines are of the SSE approach. Case 1B is ($E_1 = 0.0735, E_2 = 2.0, \Gamma = 0.01$), Case 2B (shifted up by 0.25) is ($E_1 = 0.0735, E_2 = 29.4, \Gamma = 0.01$) and Case 3B (shifted up by 0.5) is ($E_1 = 0.05, E_2 = 29.4, \Gamma = 0.01$).

One reason for this phenomenon may be because the distortion in the angular distribution is mainly caused by the electron-electron interaction which has been considered exactly in the EIAEIE approximation. The interaction between the ion and photo-electron or Auger electron also plays some role in the angular distribution. When the Auger electron has very high energy, the eikonal approximation for the ion-Auger electron interaction used in the EIAEIE approximation is valid, and causes little error. This is the other possible reason for this phenomenon. Thus, we can conclude that, unlike the energy distribution case, the angular distribution calculated by the EIAEIE approximation can be more accurate or close to the TDSE result in a case with low photo-electron energy (i.e. the condition in Eq. (2.11) is not satisfied) but very high Auger electron energy.

For cases with high photo-electron energy, the agreement between the TDSE approach and the SSE approach is better. This is what we expect, because the condition in Eq. (2.11) is satisfied here, and the EIAEIE approximation works well. We divide this energy region into two scenarios. When the two electrons have quite different energies, the disagreement between the two methods lies in the small angle region which can be shortened if we increase the photo-electron energy. Fig. 2.6 shows the angular distribution comparison for three cases. They are Case 4B ($E_1 = 0.3, E_2 = 29.4, \Gamma = 0.01$), Case 5B ($E_1 = 0.4, E_2 = 29.4, \Gamma = 0.01$) and Case 6B ($E_1 = 0.5, E_2 = 29.4, \Gamma = 0.01$). These three cases have the same E_2 and Γ but different E_1. The E_2 in all the three cases is much larger than E_1. The right hand side of the condition in Eq. (2.11) is approximately 0.0368 for all the three cases which means the condition in Eq. (2.11) is fully satisfied. Thus the two approaches agree better in the three cases. The difference between the two approaches starts from $\cos\theta_{12} = 0.74$ in Case 4B, 0.80 in Case 5B and 0.85 in Case 6B. Case 6B has the smallest discrepancy angle range due to its highest E_1. It is unclear where the difference comes from and which method works better for this situation; it may be connected either to the limitation of L = 0 in our version of the TDSE approach or with inaccuracies of the EIAEIE method in this region.
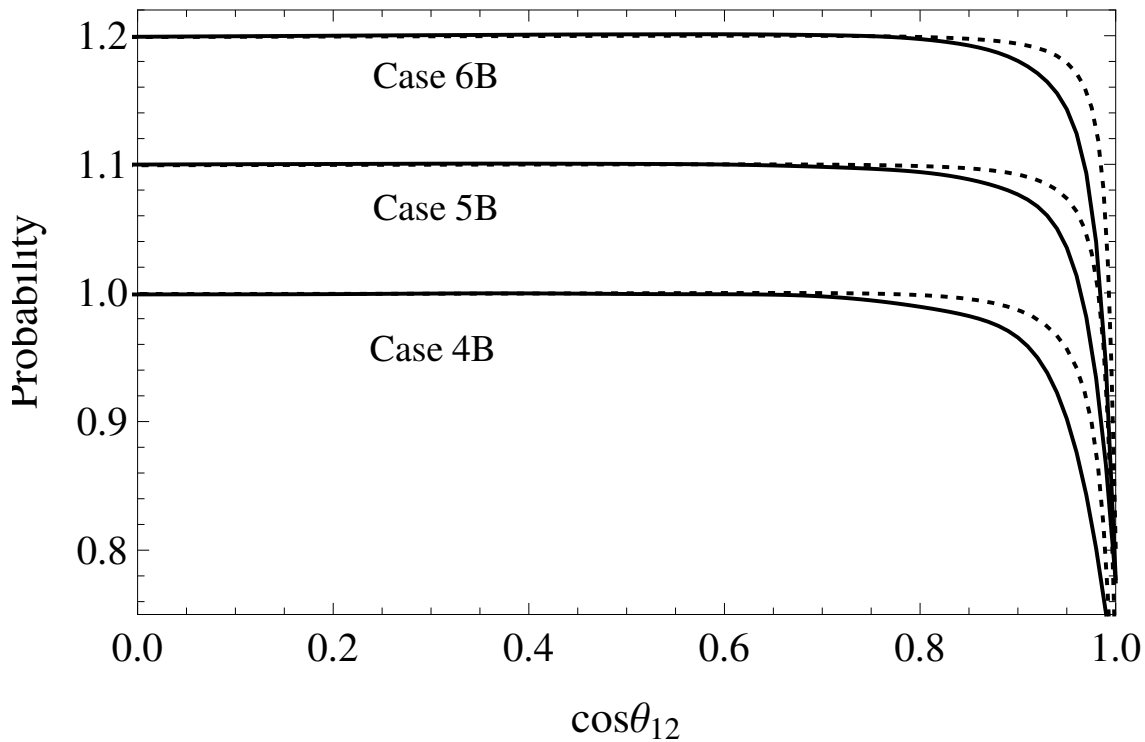
Figure 2.6: The angular distribution comparison of the two approaches for another three cases. The solid lines of the three cases are the calculations of the TDSE approach, and the dotted-lines are of the SSE approach. Two approaches agree well. Case 4B is ($E_1 = 0.3, E_2 = 29.4, \Gamma = 0.01$), Case 5B (shifted up by 0.1) is ($E_1 = 0.4, E_2 = 29.4, \Gamma = 0.01$) and Case 6B (shifted up by 0.2) is ($E_1 = 0.5, E_2 = 29.4, \Gamma = 0.01$).
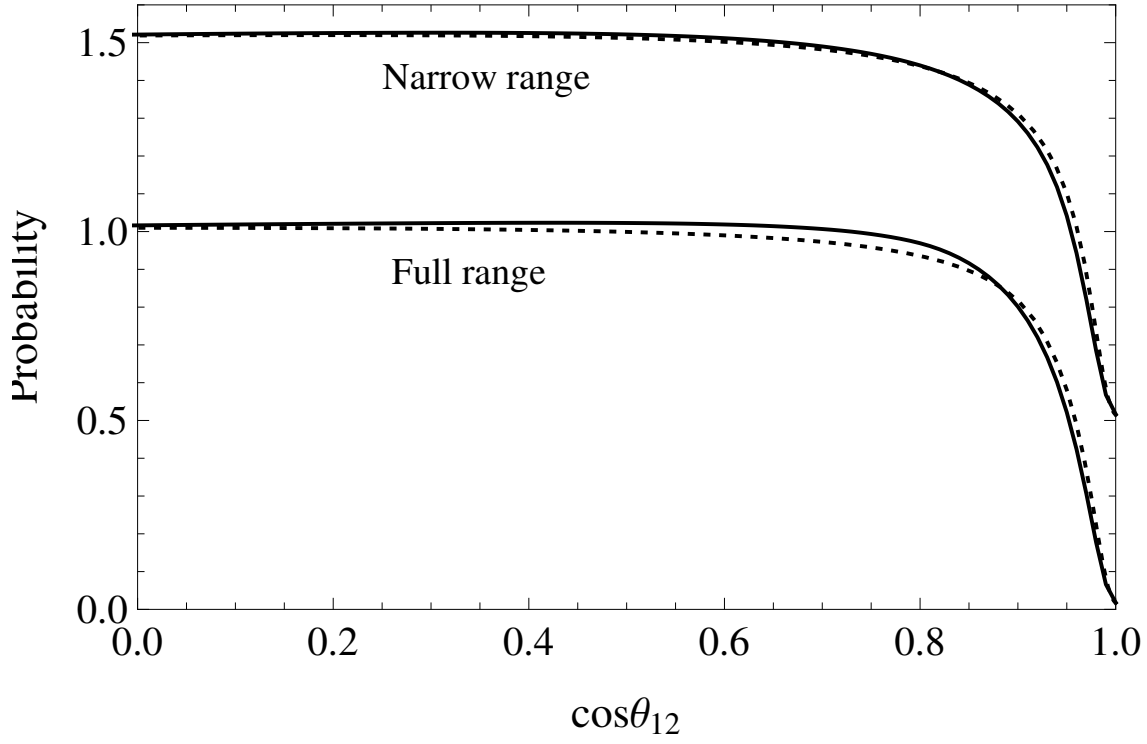
Figure 2.7: The angular distribution comparison of the two approaches for the case ($E_1 = 0.5, E_2 = 2.0, \Gamma = 0.02$) with different photo-electron energy integration range. The solid lines of the ranges are the calculations of the TDSE approach, and the dotted lines are of the SSE approach. The curves marked with "Narrow range" and "Full range" correspond to the photo-electron energy integration range 10 eV-15 eV and 6.2 eV-18 eV, respectively.

As for the second situation, when the two electrons have comparable energies, the difference between the two approaches lies in the position where the angular distribution starts to decrease. The difference for this situation is mainly caused by the inaccuracy of the EIAEIE approximation for small photo-electron energy and by the range of the photo-electron energies included in consideration. We get such a conclusion because the difference is smaller when we recalculate the angular distribution with narrower photo-electron energy integration range (smaller photo-electron energy is excluded in this range). Fig. 2.7 shows the angular distribution comparison for the case ($E_1 = 0.5, E_2 = 2.0, \Gamma = 0.02$) with two different photo-electron energy integration ranges. Substituting values into the condition in Eq. (2.11) gives $0.5 \gg 0.0585$ which indicates the EIAEIE approximation should work well. Agreement between the two methods is better when the photo-electron energy integration range is narrow, 10 eV-15 eV, and the difference becomes larger when we integrate the photo-electron energy from 6.2 to 18 eV because some low photo-electron energies (after the Auger decay) do not satisfy the condition in Eq. (2.11).

In the conclusion of the angular distributions investigation, we select two cases (2B ($E_1 = 0.0735, E_2 = 29.4, \Gamma = 0.01$) and 3B ($E_1 = 0.05, E_2 = 29.4, \Gamma = 0.01$)) to compare the angular distribution calculated by theories and that measured experimentally. The comparison for Case 2B shown in Fig. 2.8 meets our expectation. The TDSE calculation (the solid line) agrees well with the experimental measurement (the dotted line) [21]. Though the condition in Eq. (2.11) is not satisfied in this case, the EIAEIE curve (the dashed line) fits the experimental data nicely. One possible reason is that the inaccuracy of the angular distribution calculated by the EIAEIE approximation is small if the initial Auger electron energy is very high, which has been discussed above. The other reason may be because the integration range of the photo-electron energy for Case 2B is 0.5 eV-2.5 eV, very low photo-electron energies are not included in calculations which reduces the error of the EIAEIE approximation.
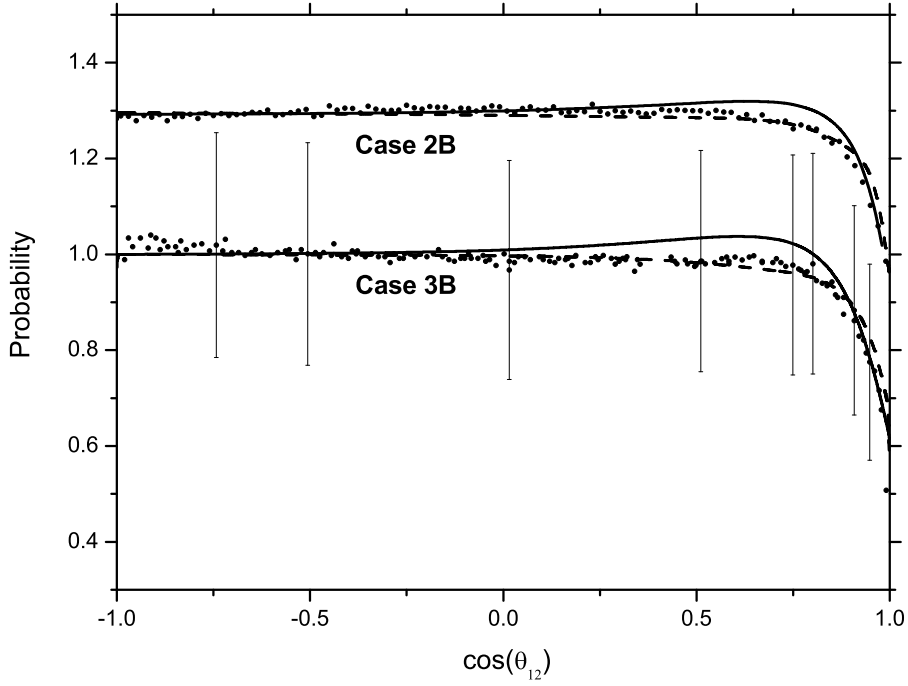
Figure 2.8: The angular distribution comparison of the theoretical calculations and experimental data for the 1s-photoionization of Ne. The dotted lines are the experimental measurement [21] (Case 2B) and [4] (Case 3B), the solid line is the calculation of the TDSE approach, and the dashed line are of the SSE approach. The error bars for statistical inaccuracy are shown for few points in the case 3B. Case 3B is ($E_1 = 0.05, E_2 = 29.4, \Gamma = 0.01$), Case 2B (shifted up by 0.3) is ($E_1 = 0.0735, E_2 = 29.4, \Gamma = 0.01$).

Generally, the theoretical calculations also agree with the experimental data in the comparison of Case 3B displayed in Fig. 2.8. Note that the integration range for photo-electron energy is 0.1 eV - 2.0 eV for the calculated curves, and the theoretical curves were convoluted with Gaussian with FWHM = 2.2° [4]. One surprising result is that the TDSE method's deviation from the experimental data (the dotted line) [4] is larger than that of the EIAEIE calculation, although both the TDSE and EIAEIE curves agree reasonably well with the measured dependence. This unexpected phenomenon can be explained by two reasons. Firstly, the interaction between the photo-electron and Auger electron, which is taken into account exactly in EIAEIE calculations, is the main factor in determining the shape of the angular distribution. Our calculation within the EIAEIE approach neglects the capture of slow photo-electrons, which is important at very low photo-electron energies, and could influence the angular distribution under certain experimental conditions (see, e.g. [57]). However, the measurements [4] do not satisfy these conditions and the EIAEIE results agree quite well with the experimental data. Secondly, our calculations in this paper within the TDSE approach take into account only the angular momentum L = 0 of the pair of the emitted electrons. However, for the Ne 1s case the other momenta L = 1, 2, 3 can contribute to the electron's emission and change the angular distribution slightly.

2.5 Conclusions

In this paper, we performed calculations of different cases within two groups of quantum mechanical approaches. After comparing the calculated and measured photo-electron energy and angular distributions, we can make the following generalizations.

For cases with low photo-electron energy, the TDSE approach describes well both the photo-electron energy and angular distributions. The SCA approximation of the SSE approach gives a similar photo-electron energy distribution as the TDSE approach if the condition of its applicability is satisfied. The other two approximations of the SSE approach, EIA and EIAEIE, are not accurate for the energy distribution because the condition of their

applicability usually can not be satisfied in this energy region. The EIAEIE approach has less inaccuracy in its angular distribution than its energy distribution if the Auger electron has very high energy.

For cases with medium-high photo-electron energy, the EIAEIE approximation of the SSE approach describes well both the photo-electron energy and angular distributions. All the three models of SSE approach give similar energy distributions as long as the conditions of their applicability are satisfied. The TDSE approach is suitable in calculating both the photo-electron energy and angular distributions in this energy region. The agreement between the two approaches is excellent in the photo-electron energy distribution. For the angular distributions, there are only small differences between the two methods. The TDSE approach may break down if both electrons have high and comparable energies. In this case a larger number of angular momenta and radial mesh points are required to get the converged results, requiring large computational resources.

For cases where both electrons have very high energies, the SSE approach can be applied for both the energy and angular distributions, and the TDSE approach breaks down because of the requirement for a huge number of points in the calculation.

By considering an energy region where both methods are applicable, it has been shown that together the TDSE and SSE approaches cover almost all of the energy range for which people might be interested in studying PCI effects. Our theoretical methods are confirmed by the agreement with measurements of the energy and angular distributions of the emitted 1s photo-electrons from Ne. More precise agreement of the TDSE approach and measured angular distributions can be reached both by including higher total angular momenta in the calculation and carrying out measurements with less statistical inaccuracy.

Chapter 3

THE STUDY OF INNER SHELL PHOTOIONIZATION FOLLOWED BY AUGER

DECAY IN THE LOW PHOTOENERGY REGIME

In this chapter we consider a particular interesting part of the parameter space for Auger and photo-electron dynamics. We focus on very low energy photo-electrons and the impact of the photo- and Auger electrons interaction on the energy and angular distribution in this regime the photo-electron ca be recaptured by the ion, or has its energy or direction significantly altered.

3.1 Background

The physical process of photo-absorption followed by sequential double ionization has been studied extensively in the past decades [4, 21, 68–82]. The first electron emitted from the nucleus is called the photo-electron because its ionization is due to photo-absorption. If the photo-electron originates from an inner shell, a second electron may undergo an Auger decay and be emitted (referred to as the Auger electron). How quickly the photo- and Auger electrons escape from the atom, and the period between the two ionizations, are two important factors in determining the subsequent dynamics. The initial energy of the Auger electron (E_2) and the Auger width (Γ) (proportional to the inverse of the time interval between the two ionizations) only depend upon the chosen atomic system. The initial photo-electron energy (E_1) is a function of the incident photon energy and the ionization potential. In summary, the atomic species and the incident photon energy co-determine the whole physical process.

During the past decades, this problem has been investigated within different atomic systems, namely, $4d_{3/2,5/2}$ photo-ionization following $N - OO$ Auger decay in Xe [68–74],

Ar 3d photo-ionization followed by Auger decay [78, 79], 1s or 2s photo-ionization with subsequent Auger decay in Ne [4, 21, 75–77], and $3d_{5/2,3/2}$ photo-ionization followed by Auger decay in Kr [81, 82]. These papers covered a wide energy range. Xe is one of the most frequently used atom species in studying this problem. The $4d_{5/2}$ photo-ionization in Xenon with subsequent $N_5 - O_{2,3}O_{2,3}$ Auger decay was selected to study the energy and/or angular distributions in References [68–74]. For this system, the initial energy of the Auger electron (E_2) was ~ 30 eV, and the Auger width (Γ) was ~ 0.12 eV. The initial photo-electron energy (E_1) was E_p-67.548 eV with a variable E_p (E_p is the incident photon energy and 67.548 eV is the binding energy of $4d_{5/2}$ [83]). E_1 was 27 eV in [68, 69] where the influences of the Post-Collision Interaction (PCI) on the energy and angular distributions for a particular ejection angular range were studied. E_1 was 30.0 eV in the work of Viefhaus et al. [70], they showed that the triple differential cross section can fully vanish because of destructive interference. Scherer et al. [71] considered the energy distribution measurement of two coincident electrons with nearly the same energy and direction, and three different initial photo-electron energies, 28.97 eV, 29.97 eV and 30.97 eV, were studied. The first coincident angular distribution was measured in Ref. [73] where E_1 was 29.9 eV. Sheinerman et al. experimentally and theoretically investigated the PCI phenomena with the same atomic system in Ref. [74], and the initial photo-electron energy was as low as 2.67 eV. In the same reference, other Xe systems, such as $4d_{3/2}$ photo-ionization with subsequent decays $N_4 - O_{2,3}O_{2,3}$ and $N_4 - O_1O_{2,3}$, were also included in their investigations, where E_2 was $\sim$ 32 eV and 16 eV, respectively, the energy for $4d_{3/2}$ was -69.537 eV, and Γ was ~ 0.104 eV for the intermediate state.

Inner-shell photo-ionization followed by Auger decay is a three-body problem, and can not be solved exactly in an analytical way. However, some approximations can be made to convert it to a two-body problem if neither of the two electrons have low energies. If the energy of one of the two electrons is low, for example E_1 is very low and the Auger electron is ejected with a high velocity, the interaction between the ion and photo-electron

has to be fully considered during the whole process. In this situation, this problem can also be solved analytically by approximately treating the e-e interaction and the interaction between the Auger electron and ion. Different cases with low initial photo-electron energy have been investigated in Refs. [75, 78, 79, 81, 82]. Because the e-e interaction was not fully considered, only the energy distribution was calculated and the angular distribution was rarely involved. The main purpose of this paper is to investigate how the angular distribution behaves when the photo-electron is emitted with extremely low energy.

To achieve this goal, we perform calculations with a numerical method [1, 20, 21] and refer to this as the Time-Dependent Schrödinger Equation (TDSE) method in which all Coulomb interactions between each pair of particles are fully taken into account. To confirm the validity of the results, we also redo the calculations with a Classical Trajectory Monte Carlo (CTMC) method. The chosen system in this paper is Kr $3d_{5/2}$ photo-ionization with subsequent $M - NN$ Auger decay, and the photo-electron energy is between 0.0 eV-1.0 eV. We select this system because it has small Γ (~ 0.088 eV) and lower E_2 (~ 2 a.u.), which are within the limitations of the TDSE method, see the discussion in Section **3.2**.

The chapter is organized as follows: in Section **3.2**, we briefly review the two theoretical methods used in this paper, TDSE and CTMC; Sec. **3.3** shows the energy and angular distributions for the system Kr $4d_{5/2}$ photo-ionization following $M - NN$ Auger decay; the last section presents the conclusion.

Atomic units are used throughout unless stated otherwise.

3.2 Theoretical methods

3.2.1 Approximations for the TDSE method

Here, we discuss the approximations used in the TDSE method. Our results are insensitive to different expressions for the short range functions $D\phi_g$ and F_2. The short range potetial in the Hamiltonia is $-Z/r$. The correlation with other electrons can not be neglected when the photo- or Auger electron travels close to the nucleus. We redid our calculations

with an expression $-(Z + (Z_t - Z)\exp(-r/r_a))/r$ for the potential instead (r_a and Z_t are the atomic radius and number, respectively, $r_a = 1.66$ a.u. and $Z_t = 36$ for Kr). Compared with the previous results, there are only small changes in the angular distributions for cases $E_1 = 0.0$ eV and 0.1 eV, and almost no changes for other cases in this paper. We also assume that both the emitted electrons start with zero angular momentum. During the subsequent electron dynamics, the two electrons have the same angular momentum magnitude because the total angular momentum (which is zero) is conserved. Due to the expected complexity, we did not perform calculations for other total angular momentum values. This approximation is expected to work well in the chosen system. The small Auger width means that the photo-electron has a longer time to travel away from the nucleus before the Auger decay. Meanwhile, the initial Auger electron energy is not high which postpones the strongest interaction between the photo and Auger electrons. The validity of the zero total angular momentum approximation will be increased if the two electrons meet far away from the nucleus. Moreover, we focus on those electrons that remain escaping from the ion, which makes this approximation more accurate.

3.2.2 Classical Trajectory Monte Carlo method

The TDSE method described above has been proven to be valid in studying inner shell photo-ionization followed with Auger decay problems [1, 21]. However, it is the first time that this method is applied to the extremely low photo-electron energy region, which is of particular interest for the scenarios studied here, where the calculated angular distributions have unusual shapes. Thus, it is desirable to check the results with a completely different theoretical method. We simulate the process with a CTMC approach [20].

In our classical simulation, the photo-electron is emitted from the nucleus at $t = 0$, with a random energy selected from a normal distribution $\exp(-(E - E_1)^2/2\sigma^2)$, where E_1 is the initial photo-electron energy used in the quantum mechanical method and σ equals $\Gamma/2\sqrt{2\ln 2}$, with a random direction chosen from flat $\cos\theta$ and flat ϕ; the Auger electron is

launched at $t = t_2$, where t_2 is chosen from an exponential distribution $\Gamma \exp(-\Gamma t)$, with a random energy selected from a normal distribution $\exp(-(E - E_2)^2/2\sigma^2)$ where E_2 is the initial Auger electron energy used in the TDSE method, with a fixed direction $\theta = \pi/2$ and $\phi = 0$. Note that we make the two electrons propagate from a small finite radius (0.001 au) to avoid the infinite Coulomb potential and velocity at the starting point, and the two electrons' positions are updated using Newton's Second Law until the relative angle distribution will not change. The relative angle between the two electrons θ_{12} is calculated via $\cos\theta_{12} = \frac{\vec{v_1}\cdot\vec{v_2}}{v_1 v_2}$.

3.3 Results and discussion

The system chosen in this paper is Kr $3d_{5/2}$ photo-ionization followed with $M - NN$ Auger decay where Γ is ~ 0.088 eV and E_2 is ~ 2 a.u.. We will study the photo-electron energy and angular distributions in this system by changing the photon energy. The cases included in this paper are $E_1=$ 1.0 eV, 0.5 eV, 0.25 eV, 0.125 eV, 0.1 eV and 0.0 eV. We first investigate in Subsection **3.3.1** the changes to the photo-electron energy distributions, and then in Subsection **3.3.2** consider the changes to the relative angular distributions.

3.3.1 The photo-electron energy distribution

Figure 3.1 displays the photo-electron energy distribution after the Auger decay for different initial photo-electron energies. Fig. 3.1 (a) is for cases $E_1=1.0$ eV (dot-dashed line), 0.5 eV (dotted line), 0.25 eV (dashed line), 0.125 eV (thin-solid line) and 0.1 eV (thick-solid line); Fig. 3.1 (b) is for the case $E_1=0.0$ eV which needs a greater energy range to show the complete distribution. For each case, the energy of the photo-electron might be expected to be symmetrically centered on the initial photo-electron energy E_1 before the Auger decay [4]. After the Auger decay, the maximum of the distribution is shifted to smaller energy, and the distribution becomes asymmetric. As shown in Fig. 3.1 (a), the shift of the distribution peak is δE=1.0-0.88=0.12 eV for the case $E_1=1.0$ eV, δE=0.5-0.33=0.17 eV for the case $E_1=0.5$ eV, and δE=0.25-0.05=0.2 eV for the case $E_1=0.25$ eV. The peaks for the

other three cases are shifted to the negative energy region, their shifts can not be calculated here.

This phenomenon is mainly caused by the abrupt change in the ion's charge when the Auger decay happens. The increase in the ion charge reduces the ion potential by $1/r_0$, where r_0 is the distance the photo-electron travels away from the nucleus before the Auger electron is launched. Cases with larger initial photo-electron energy have smaller shifts of the distribution peak because the life-time of the intermediate state is approximately the same for each case and the larger initial photo-electron energy causes larger r_0. Within the same case, the shift in energy of $1/r_0$ is smaller if the photo-electron has larger energy, which can explain why the energy distribution is broader and asymmetric, and why the tail of the left side of the distribution lasts longer than that of the right side.

The interaction between the photo- and Auger electrons also has some influence on the shift of the energy distribution. The Auger electron will transfer part of its energy to the photo-electron when it passes by. The stronger the interaction is, the more energy the photo-electron will obtain. We have performed calculations for some cases with the same initial photo-electron energy and Auger width but different initial Auger energies. The shifts of the distribution peak δE are not the same, though the energy shifts caused by the change of the ion charge would be expected to be the same. The reason is that their e-e interaction strengths are different. Lower initial Auger energy means that the Auger electron can interact with the photo-electron for a longer time, more energy will be transferred to the photo-electron energy which makes the shift δE smaller.

Figures 3.1 (a) and (b) also show that a small portion of photo-electrons are captured to bound states after the Auger decay if the photo-electron has a relatively high initial energy E_1; however, when E_1 becomes smaller, more and more photo-electrons will stay at bound states. We expect that the angular distribution profiles of cases E_1=1.0 eV and 0.5 eV will be determined by the strength of the interaction between the photo- and Auger electrons and
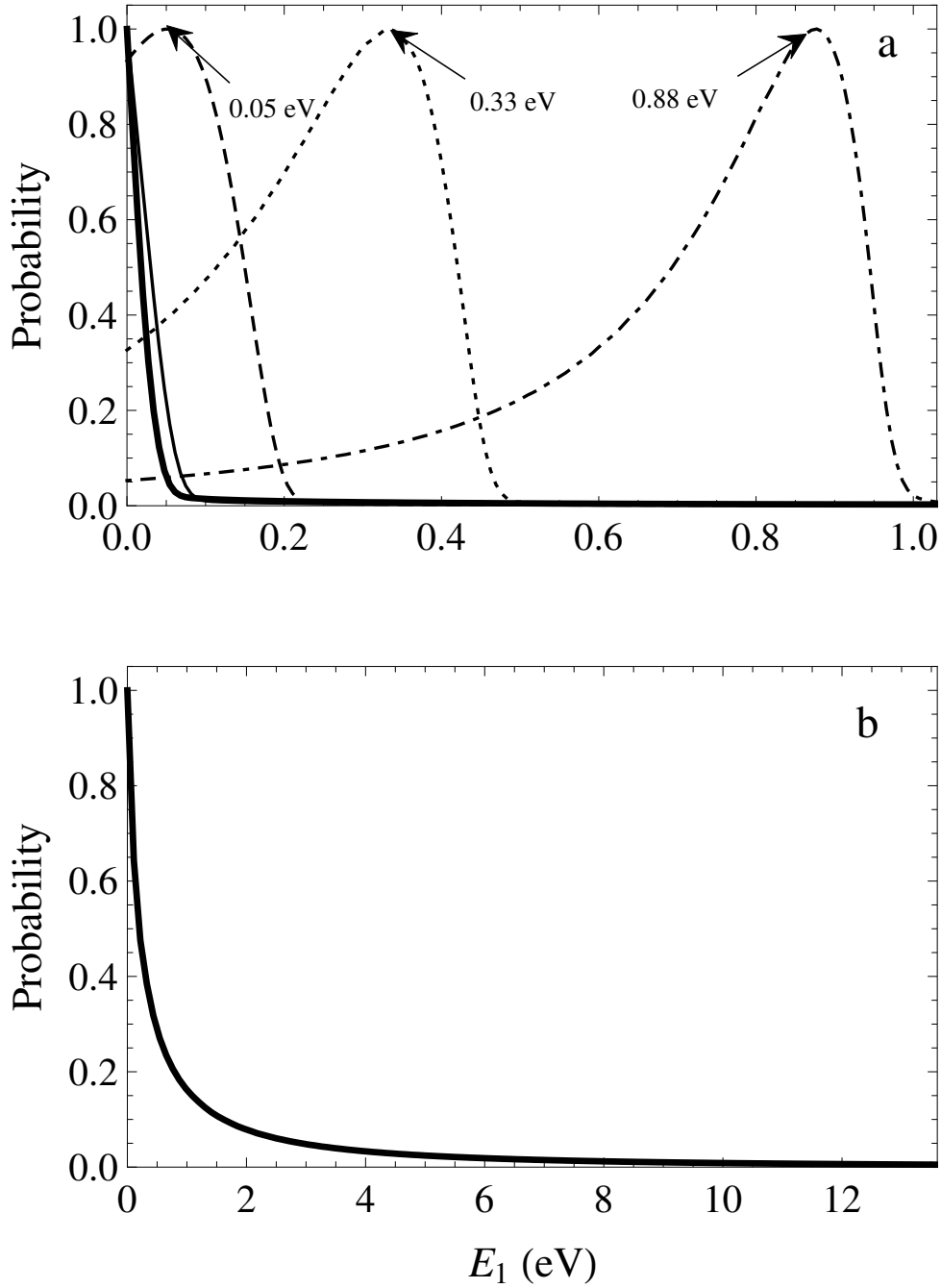
Figure 3.1: The photo-electron energy distributions (normalized by dividing by the maximum probability in positive energy range) for cases E_1=1.0 eV (a, Dot-dashed line), 0.5 eV (a, Dotted line), 0.25 eV (a, Dashed line), 0.125 eV (a, thin solid line), 0.1 eV (a, thick solid line) and 0.0 eV (b, thick solid line). The arrows point to the energy with maximum probability which are 0.88 eV for the case E_1=1.0 eV, 0.33 eV for the case E_1=0.5 eV and 0.05 eV for the case E_1=0.25 eV.

have a normal profile, while the captured photo-electrons will seriously distort the angular distributions of the other 4 cases.

3.3.2 The angular distribution discussion

The electron-electron interaction is usually considered as the main factor in determining the shape of the relative angular distribution. When the two ejected electrons travel in the same direction, the fast Auger electron will push the slow photo-electron away by a small relative angle and pass by it. Thus in the angular distribution, the probability at $\cos\theta_{12}=1$ is much lower than that of the other relative angular positions and the probability at a small non-zero relative angle is higher. If the two ejected electrons travel with a larger relative angle, they do not interact significantly with each other making the distribution flat at those angular positions. As shown in Fig. 3.2, the curves for cases $E_1=1.0$ eV (Dot-dashed line) and 0.5 eV (Dotted line) have the overall features stated above. The strength of the interaction will change the depth of the hole at $\cos\theta_{12}=1$ and the height of the convexity nearby. This is not the focus of this paper. Instead we investigate the effects from those captured photo-electrons, which affects the shape of the angular distribution when E_1 is extremely low.

Next, we investigate how the capture of the photo-electrons reshapes the angular distribution. We refer to this factor as the capture factor below. As shown in Fig. 3.1, more and more photo-electrons are captured by the ion as one decreases the initial photo-electron energy. Correspondingly, the angular distributions (shown in Fig. 3.2) are distorted by the capture factor to varying degrees. The influence of this factor on the angular distribution appears as a sharpening of the curve at the angular position with the highest probability or in the creation of a nearby peak. This phenomenon happens because the angular distributions shown in Fig. 3.2 only count the photo-electrons with positive energy, but exclude those captured by the nucleus which are distributed unevenly over the relative angular position. The photo-electrons at the angular position with the highest distribution probability are
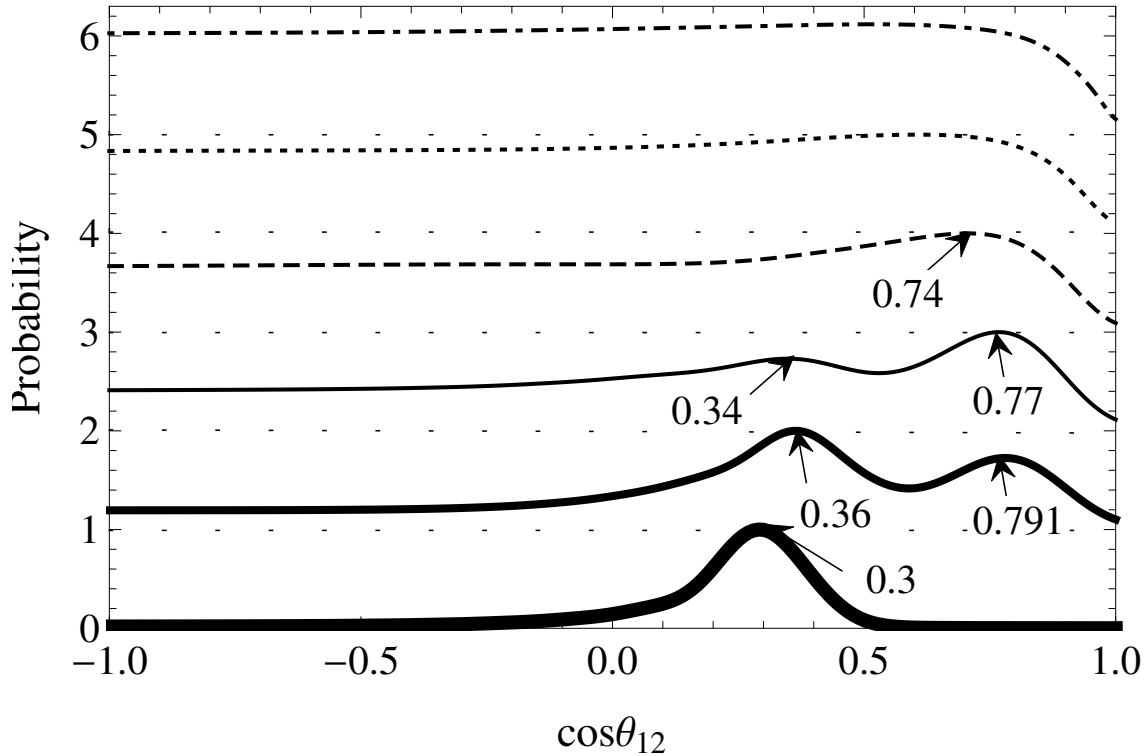
Figure 3.2: The angular probability distributions calculated by the TDSE method (normalized by dividing by the maximum probability) for cases E_1=1.0 eV (Dot-dashed line, shifted up by 5.0), 0.5 eV (Dotted line, shifted up by 4.0), 0.25 eV (Dashed line, shifted up by 3.0), 0.125 eV (thin solid line, shifted up by 2.0), 0.1 eV (thicker solid line, shifted up by 1.0) and 0.0 eV (the thickest solid line). The arrows point to the angular positions of peak(s) which are $\cos\theta_{12}$=0.74 for the case E_1=0.25 eV, $\cos\theta_{12}$=0.34 and 0.77 for the case E_1=0.125 eV, $\cos\theta_{12}$=0.36 and 0.791 for the case E_1=0.1 eV and $\cos\theta_{12}$=0.3 for the case E_1=0.0 eV .

49

usually more energetic because they have strongly interacted with the Auger electron and gained more energy. They are unlikely to be captured to the nucleus and the possibility for photo-electrons at other angular positions being captured is high, which results in one or two sharper peaks at the angular distribution.

We analyze the angular distributions displayed in Fig. 3.2 in more detail. For the case E_1=1.0 eV (Dot-dashed line), almost no photo-electrons are captured by the nucleus. Its angular distribution is with the expected shape. A small part of the photo-electrons are captured for the case E_1=0.5 eV (Dotted line). The capture factor exerts little influence on the angular distribution, and the shape is close to a standard one. When the initial photo-electron energy decreases to E_1=0.25 eV (Dashed line), the angular distribution has a sharp peak in the angular position near 0 relative angle. The capture factor starts to play an important role in the angular distribution shape. For cases E_1=0.125 eV (thin Solid line), 0.1 eV (thicker Solid line) and 0.0 eV (the thickest Solid line), most photo-electrons do not have enough energy to escape. Their angular distributions show that the probability of a large range of angular position is low, because only a small portion of the photo-electrons escape the capture of the nucleus and are largely centered around the peak of the distribution. For cases E_1=0.125 eV and 0.1 eV, the successfully ejected photo-electrons come from two sources: part of them (Component 1) are those with positive energy at the momentum when the Auger decay happens, and the other part (Comp. 2) are those with negative energy when the Auger decay happens but that gain enough energy for ionization from the Auger electron while being passed. These two components of the ejected photo-electrons correspond to the two peaks in their angular distributions. The left peak in the angular distribution is for Comp. 2 and the right one is for Comp. 1. The reason for this conclusion is as follows. Those photo-electrons with negative energy at first will interact with the Auger electron at a small radius and they can be pushed to a larger relative angular position. However, for the photo-electrons with positive energy at first, the strongest e-e interaction happens at a larger radius and the interaction will disappear when the photo-electrons are pushed to a

small relative angle because the distance between the two electrons is large. We believe the two sources also exist in cases E_1=0.25 eV and 0.0 eV, but only one peak appears in their angular distributions because the numbers of ejected photo-electrons from the two sources are not comparable. Comp. 1 dominates among the ejected photo-electrons for the case E_1=0.25 eV, and most ejected photo-electrons come from Comp. 2 for the case E_2=0.0 eV.

Two physical quantities may be helpful in demonstrating the explanations above. One is the PED which displays the distribution of the photo-electron energy and relative angle, and the other is the angular momentum distribution for those ejected photo-electrons P_ℓ. We show PED for two cases in Fig. 3.3, the upper figure is for the case E_1=0.125 eV and the lower figure is for the case E_1=0.0 eV. The color indicates the size of the probability. There are two bright spots in the plot for the case E_1=0.125 eV and one bright spot for the case E_1=0.0 eV which correspond to two peaks or one peak in their angular distributions shown in Fig. 3.2. The main purpose for this plot is to demonstrate that the photo-electrons with higher energy are centered on the peak area for which the capture factor plays an important role in reshaping the angular distribution.

Figure 3.4 shows the angular momentum distributions for the ejected photo-electrons of different cases which include E_1=1.0 eV (red Dot-dashed line), 0.5 eV (green Dotted line), 0.25 eV (blue Dashed line), 0.125 eV (thin solid line), 0.1 eV (thicker solid line) and 0.0 eV (the thickest solid line). For all of the cases, the maximum probability in each angular momentum distribution is at $\ell = 0$. This behavior is reasonable because we assume that the photo-electron starts with 0 angular momentum and its angular momentum remains the same during the following time propagation, except for interacting with the Auger electron when both particles are emitted in a similar direction. Fig. 3.4 also shows that the proportion of the ejected photo-electrons with high angular momentum is larger in the low E_1 cases, which demonstrates our explanation for the unusual shape in the angular distribution. For the cases with very low E_1, a large part of those photo-electrons that successfully escape from the nucleus are due to the strong interaction with the Auger electron which lead to the

52
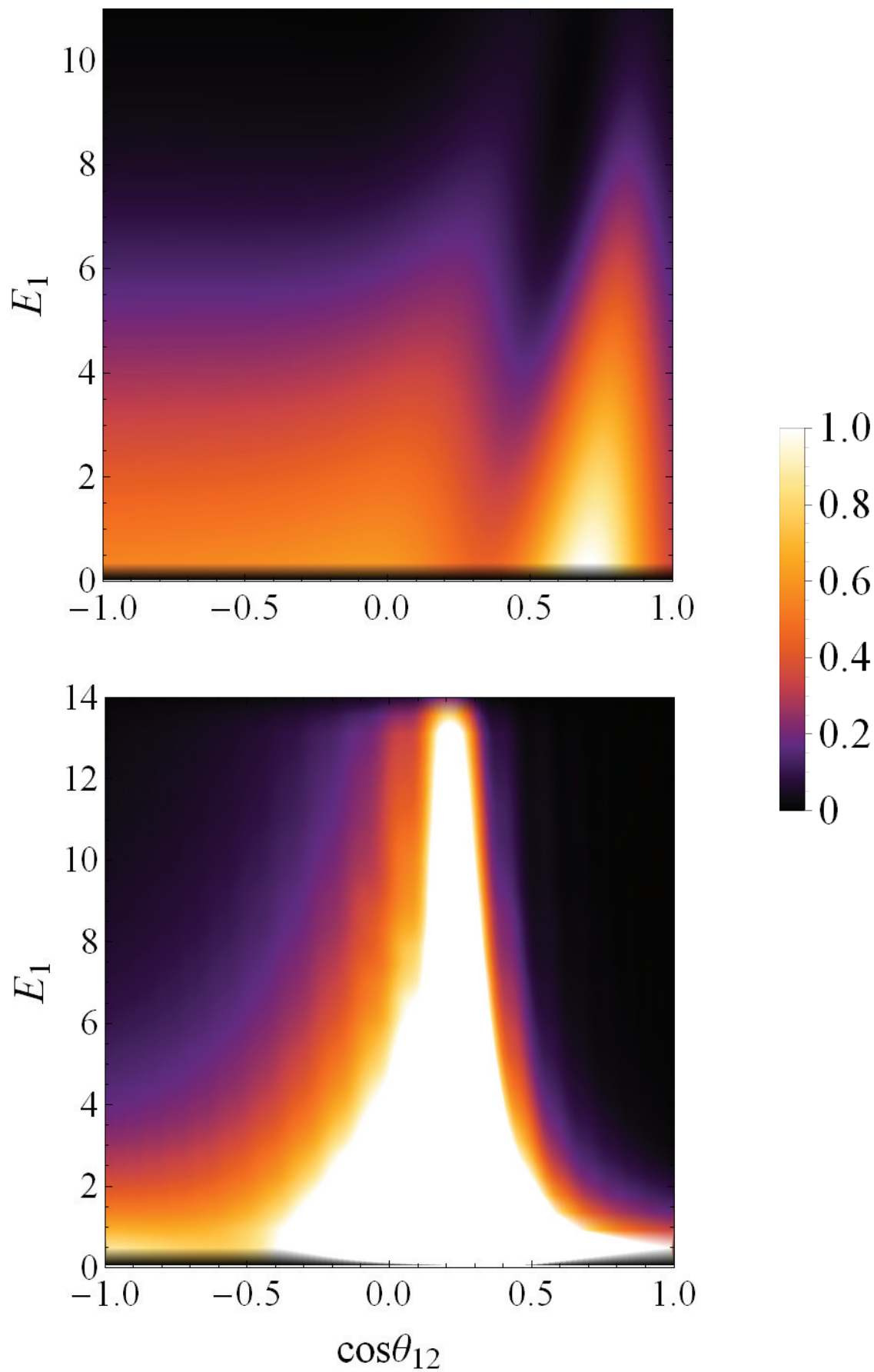
Figure 3.3: The physical quantity PED for cases E_1=0.125 eV (the upper figure) and 0.0 eV (the lower figure).

phenomena that more ionized electrons are distributed at higher angular momenta. In the angular momentum distribution, there is a second peak for cases E_1 =0.0 eV, 0.1 eV and 0.125 eV. The peak position is at ℓ=4 for the case E_1=0.0 eV, ℓ=7 for the case E_1=0.1 eV and E_1=6 for the case E_1=0.125 eV. There is no regularity for the position of the second peak, but we can conclude that cases with lower E_1 have a sharper second peak.

We simulate the whole process with a completely different theory - the Classical Trajectory Monte Carlo method. Fig. 3.5 displays the angular distributions for cases E_1=1.0 eV (Dot-dashed line), 0.5 eV (Dotted line), 0.25 eV (Dashed line), 0.125 eV (thin solid line), 0.1 eV (thicker solid line) and 0.0 eV (the thickest solid line). The main differences between Fig. 3.5 and Fig. 3.2 lie in two points. One is that the probability at $\cos\theta_{12}$=1 is not exactly 0 in Fig. 3.2 for cases with non-zero initial photo-electron energy, however, it is very close to 0 in Fig. 3.5. This difference comes from the different descriptions of particles in quantum and classical mechanics. In quantum mechanics, electrons are also waves which make it possible for the two ejected electrons to move in the same direction, while in classical mechanics the photo-electron has to be pushed aside and then the Auger electron can pass by. The other point is that the angular positions of the peaks are slightly different and the relative heights of the two peaks for the case E_1=0.125 eV are different. A possible explanation is that the captured photo-electrons move in an elliptical orbit in quantum mechanics, while in our classical theory they oscillate along the radius.

There are two points that are worthy of note. One is that the situation with two peaks in the angular distribution does not always happen. We did not find cases with two peaks in the angular distribution if they have a large Γ. A possible reason is that the ejected photo-electrons from the two sources are not separated far enough for the short traveling time before the Auger decay, and Comp. 1 and 2 of the ejected photo-electrons mix together. The other point is that the calculations performed in this paper do not consider re-emission of those non-ejected photo-electrons which may happen during the experiment because the ion may be left at an excited state and can transfer energy to the captured photo-electrons
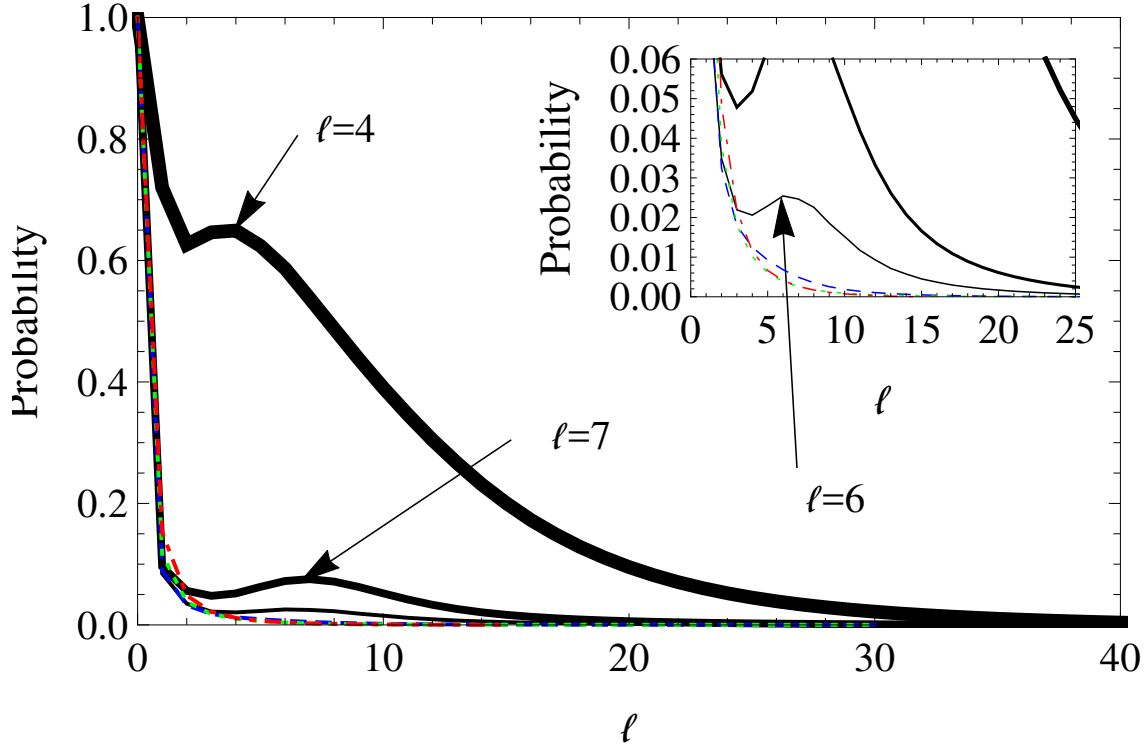
Figure 3.4: The angular momentum distributions for the ejected photo-electrons (normalized by dividing by the maximum probability) of cases E_1=1.0 eV (red Dot-dashed line), 0.5 eV (green Dotted line), 0.25 eV (blue Dashed line), 0.125 eV (thin solid line), 0.1 eV (thicker solid line) and 0.0 eV (the thickest solid line). The arrows point to the angular momentum positions of the second peak which are ℓ=6 for the case E_1=0.125 eV, ℓ=7 for the case E_1=0.1 eV and ℓ=4 for the case E_1=0.0 eV .
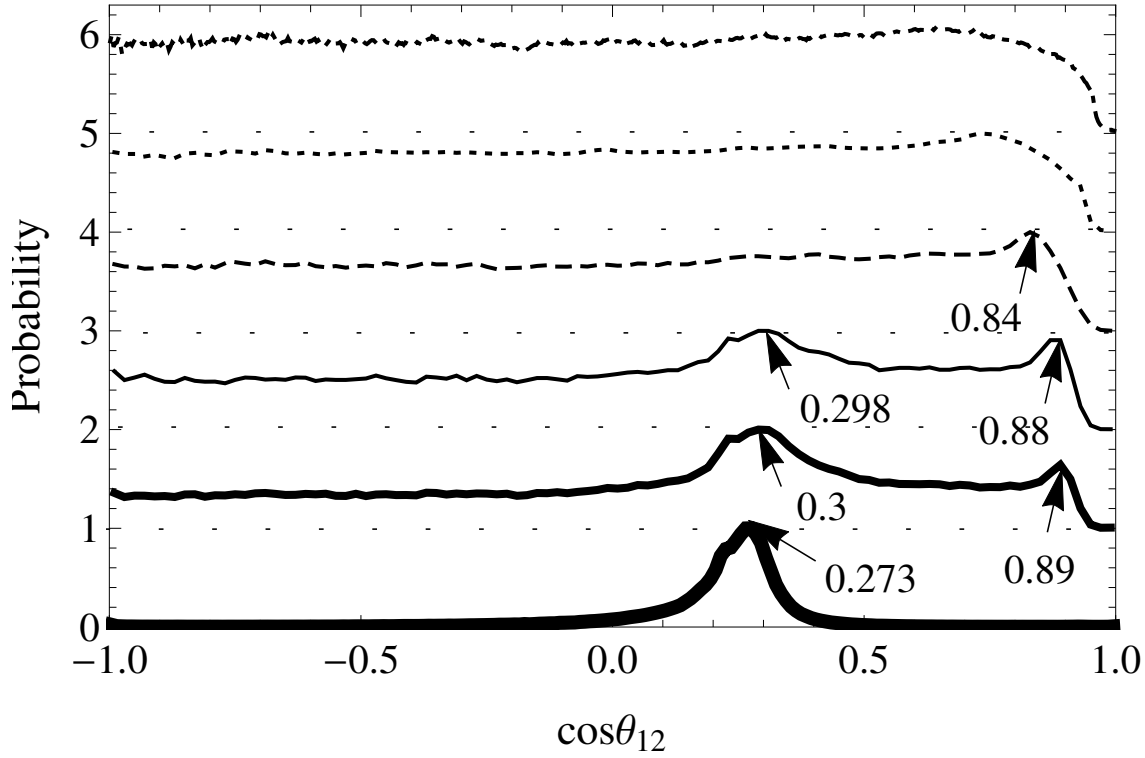
Figure 3.5: The angular probability distributions calculated by the CTMC method (normalized by dividing by the maximum probability) for cases E_1=1.0 eV (Dot-dashed line, shifted up by 5.0), 0.5 eV (Dotted line, shifted up by 4.0), 0.25 eV (Dashed line, shifted up by 3.0), 0.125 eV (thin solid line, shifted up by 2.0), 0.1 eV (thicker solid line, shifted up by 1.0) and 0.0 eV (the thickest solid line). The arrows point to the angular positions of the peak(s) which are $\cos\theta_{12}$=0.84 for the case E_1=0.25 eV, $\cos\theta_{12}$=0.298 and 0.88 for the case E_1=0.125 eV, $\cos\theta_{12}$=0.3 and 0.89 for the case E_1=0.1 eV and $\cos\theta_{12}$=0.279 for the case E_1=0.0 eV .

to make them ionize. In order to obtain the angular distribution with similar features shown in Fig. 3.2, those re-emitted photo-electrons have to be excluded.

3.4   Conclusions

We investigated the scenario of photo-ionization followed by Auger decay in the extremely low photo-electron energy region. The system chosen was Kr $3d_{5/2}$ photo-ionization followed with $M - NN$ Auger decay in which Γ is ~ 0.088 eV and E_2 is ~ 2 a.u.. We have performed calculations of the energy and angular distributions for cases $E_1 = 1.0$ eV, 0.5 eV, 0.25 eV, 0.125 eV, 0.1 eV and 0.0 eV. The energy distribution shifts to smaller energies because of the abrupt decrease in the ion potential. The shift becomes larger when the initial photo-electron energy is decreased. For the angular distribution, the capture factor plays an increasingly important role in the shape of the distribution with the decrease of the initial photo-electron energy, with a peaked profile being predicted for very low energy cases.

Chapter 4

A SEARCH FOR EVIDENCE FOR BELOW THRESHOLD DIELECTRONIC

RECOMBINATION USING USING SATELLITE LINES

4.1 Background

As mentioned in chapter 1 certian low temperature DR rate coefficients are hyper sen-
sitive to the presence of near threshold resonances. A resolution to this problem has been
proposed by Robicheaux et al. [12]. They pointed out that traditional dielectronic capture
rates occur through a mixing of doubly excited states above the ionization potential (e.g.
$1s^2 2s 2p nl$) with continuum states (e.g. $1s^2 2s^2 kl$ - where kl represents a continuum electron).
An analogous process seems likely, with doubly excited states just below the ionization po-
tential mixing with high lying Rydberg states (e.g. $1s^2 2s^2 nl$), allowing dielectronic capture
into those doubly excited states. That is, there would be an analytic continuity of the Auger
rate for states above the ionization potential

$$A^a_{above} \propto |\langle \Psi_{1s^2 2s 2p nl} | 1/r_{12} | \Psi_{1s^2 2s^2 kl} \rangle |^2 \tag{4.1}$$

through to states just below the ionization potential

$$A^a_{below} \propto |\langle \Psi_{1s^2 2s 2p nl} | 1/r_{12} | \Psi_{1s^2 2s^2 nl} \rangle |^2 \tag{4.2}$$

The *dielectronic capture rate coefficient* into a single resonance (j) using detailed balance
from the Auger rate for the above threshold resonances is

$$\alpha_j^{above}(T_e) = \left(\frac{4\pi a_o^2 I_H}{k_B T_e} \right)^{3/2} \frac{\omega_j}{2\omega_i} e^{-E_c/(k_B T_e)} A^a_{j,E_c}, \tag{4.3}$$

where the exponential term is due to the Maxwellian distribution of the free electrons. The equivalent below threshold dielectronic capture rate coefficient into level i is

$$\alpha_i^{below}(T_e) = \left(\frac{4\pi a_o^2 I_H}{k_B T_e}\right)^{3/2} \frac{\omega_j}{2\omega_i} e^{-E_c/(k_B T_e)} f(E_c) A_{j,E_c}^a, \qquad (4.4)$$

where E_c is the energy below threshold, so is a negative number and $f(E_c)$ is the Saha-Boltzman deviation factor, which gives the deviation of the negative energy electron distribution function from its expected thermodynamic value. Note that

The conditions for this below threshold recombination process to be possible are

1. The doubly excited state must mix with the Rydberg states. The high-n Rydberg states will have overlapping energies due to their Heisenberg uncertainty, forming a pseudo-continuum. Thus, the doubly excited state must be embedded in this Rydberg continuum.

2. The population distribution of the Rydberg states is the equivalent of the free-electron distribution function. Thus, the 'negative energy' electron distribution function must have significant population.

For this first condition, we use an ADAS code called ADAS204 which calculates excited populations up to high principal quantum number (typically n=500). It uses semi-classical and semi-empirical rate coefficient data, along with higher quality dielectronic recombination rate coefficient data from the DR project [8]. The code uses collisional-radiative theory to solve for the excited populations, see [15] for more details. This code was modified to calculate the lifetime (τ = collisional+radiative lifetime) for each of the excited states. An energy uncertainty was then calculated for each n-shell based upon the Heisenberg uncertainty relationship

$$\Delta E \Delta \tau \geq \hbar/2. \qquad (4.5)$$
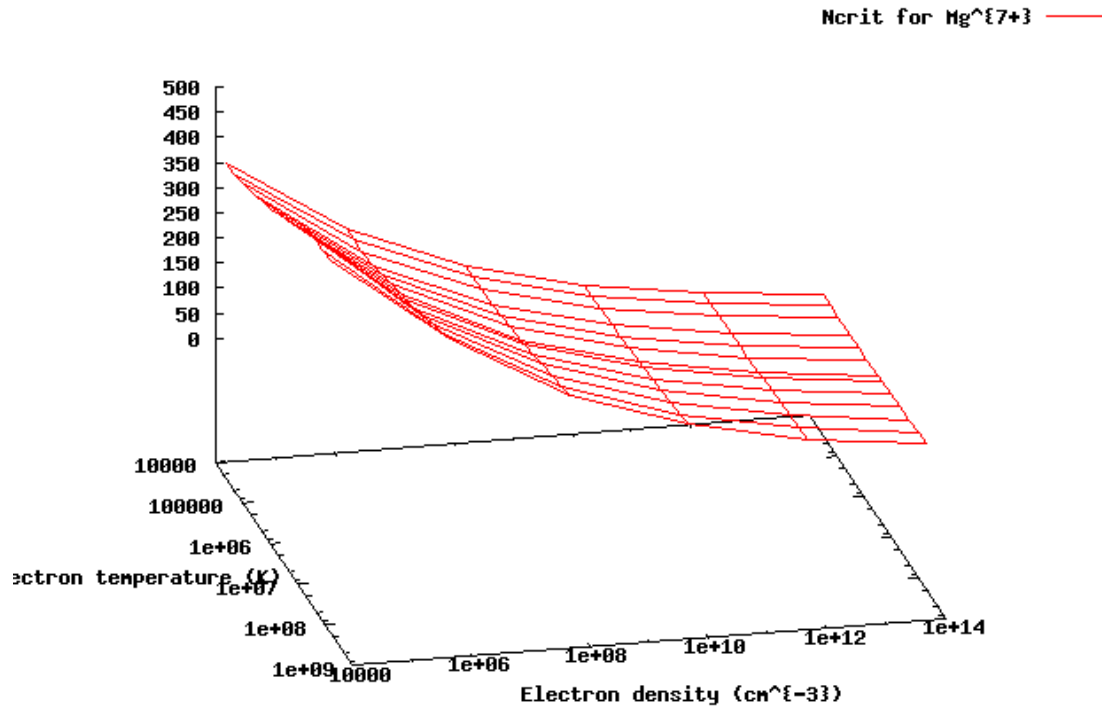
Figure 4.1: Plot for Mg^{7+} of the critical n-shell at which the Rydberg continuum is expected to start, as a function of the plasma electron temperature and density.

From this a critical n-shell can be determined above which the Rydberg states will form a pseudo-continuum. That is, where the energy spacing between adjacent n-shells is smaller than their Heisenberg energy uncertainty. This critical n-shell will be a function of both electron temperature and density. Fig 4.1 shows a plot of the critical n-shell for Mg^{7+}.

For the second condition, we require the population distribution of these 'negative energy' Rydberg states to be significant at the energy of the doubly excited state. ADAS204 also evaluates the Rydberg populations, and is used to generate the distribution function used in our below threshold DR rate coefficient calculations. Fig 4.2 shows an example of such negative energy distribution functions. Note that the distribution function is calculated as a function of the principal quantum number, it is then transformed into an energy distribution function via

$$E = -\frac{Z_1^2 I_H}{\nu^2} \tag{4.6}$$

where I_H is the Rydberg constant and ν is the effective principal quantum number. ν includes a correction for the quantum defect (μ). That is, $\nu = n - \mu$.

Chapter 5 will contain a survey of Li-like and Be-like ions to identify ions that meet the above conditions and require re-evaluation of their rate coefficients. In this chapter we focus on identifying ions that have near threshold resonance **and which may produce strong satellite line emission from the below threshold doubly excited states**. As part of this chapter we determine the closest Rydberg n-shell to the doubly excited state. If this number is above the value set by condition (1) above, and the Rydberg population is significant (condition (2) above), then the ion in question is investigated further. However, we have four additional conditions which have to be met for these satellite lines to be used as evidence of below threshold recombination.

3. The Type I radiation (i.e. core radiative decay) for the doubly excited state must be an electric dipole core radiative decay, otherwise the satellite line would be too weak to be observed.

4. Cascades from higher n-shells should not be a significant populating mechanism of the below threshold doubly excited state. Otherwise it would not be certain that the level was being populated by below threshold recombination. That is, it could be populated via an above threshold dielectronic caputer which then cascades down to the below threshold state.

5. There must be NIST energies for the doubly excited below threshold state. This gives us confidence that the line is genuinely just below the ionization potential and allows accurate wavelengths to be calculated.

6. The satellite line must be resolvable from the non-satellite line of the parent ion.

If all of these conditions are met, then we list this ion as a promising candidate for a spectroscopic study. Note that we do not use the energy levels from DR calculations in this chapter because the uncertainty in theory is too large to allow spectroscopic accuracy in the wavelength calculations. With many of the lines emitting in the UV and visible, we require accuracies of a 0.1% or better in the energies to be able to identify the spectral lines from their wavelengths. Thus, we rely on NIST energies for the work described in this chapter.

The rest of this chapter is organized as follows. We introduce our methodology for searching for promising below threshold satellite line candidates and give some tables of results in in Sec. 4.2. Sec. 4.3 outlines the theory for the modeling of satellite line intensities. In Sec. 4.4, we compare modeled satellite line with existing spectra. The last section is a summary and outlook for the future work.

4.2   Search for likely elements and ion stages to verify the exist of the below threshold

We have investigated several sequences, but only display the Li-like and Be-like sequences in Tables 4.1 and 4.2. In these tables the ion stage, the below threshold doubly excited configuration and its below threshold energy are given. We also show the n-shell for the closest (in energy) Rydberg configuration, to help determine if the doubly excited state is embedded in the Rydberg continuum (condition 1 above). Note that this quantum number n is determined from ($n=\sqrt{13.6 \times Z_1^2/E_{res}}$). We also note in the table whether it is a promising candidate for satellite/valence line observation and the main satellite/valence wavelengths are included (conditions 3 – 6 above).

After analysis, we conclude that C^{3+}, F^{6+}, C^{2+} and N^{3+} satisfy all the conditions and can serve as candidates for the observation of satellite/valence lines. We select C^{3+} as the strongest candidate and as a useful illustration on how other systems could be investigated.

For C^{3+}, the main resonance line comes from transitions $1s^22p$ ($^2P_{1/2}$)→$1s^22s$ ($^2S_{1/2}$) and $1s^22p$ ($^2P_{3/2}$)→$1s^22s$ ($^2S_{1/2}$), with wavelengths of 1550.77 Åand 1548 Å, respectively. The

below threshold states of C^{3+} within the Rydberg continuum are $1s^22p(^2P)4d(^3F)$ at 0.051 eV below threshold, $1s^22p(^2P)4d(^1D)$ at 0.053 eV below threshold and $1s^22p(^2P)4p(^1D)$ at 0.0748 eV below threshold. Such close proximity to the ionization potential was the primary reason C^{3+} was chosen for further study. These states seem likely to be within the Rydberg continuum. The below threshold satellite lines formed by transition from these states are listed in Table 4.3. Satellite lines of above threshold resonance are should also be observed and their wavelengths are listed in Table 4.4. The above threshold terms are $1s^22p4d(^3D)$ $1s^22p4f(^3G)$, $1s^22p4f(^3F)$, $1s^22p4d(^3P)$, $1s^22p4d(^1F)$, $1s^22p4f(^3D)$ and $1s^22p5p(^1P)$. Note that NIST may be missing near threshold doubly excited states for some of the ions that we are investigating. Thus, the following list should not be treated as comprehensive, but a list of ions that can be investigated with some confidence that they have below threshold resonances.
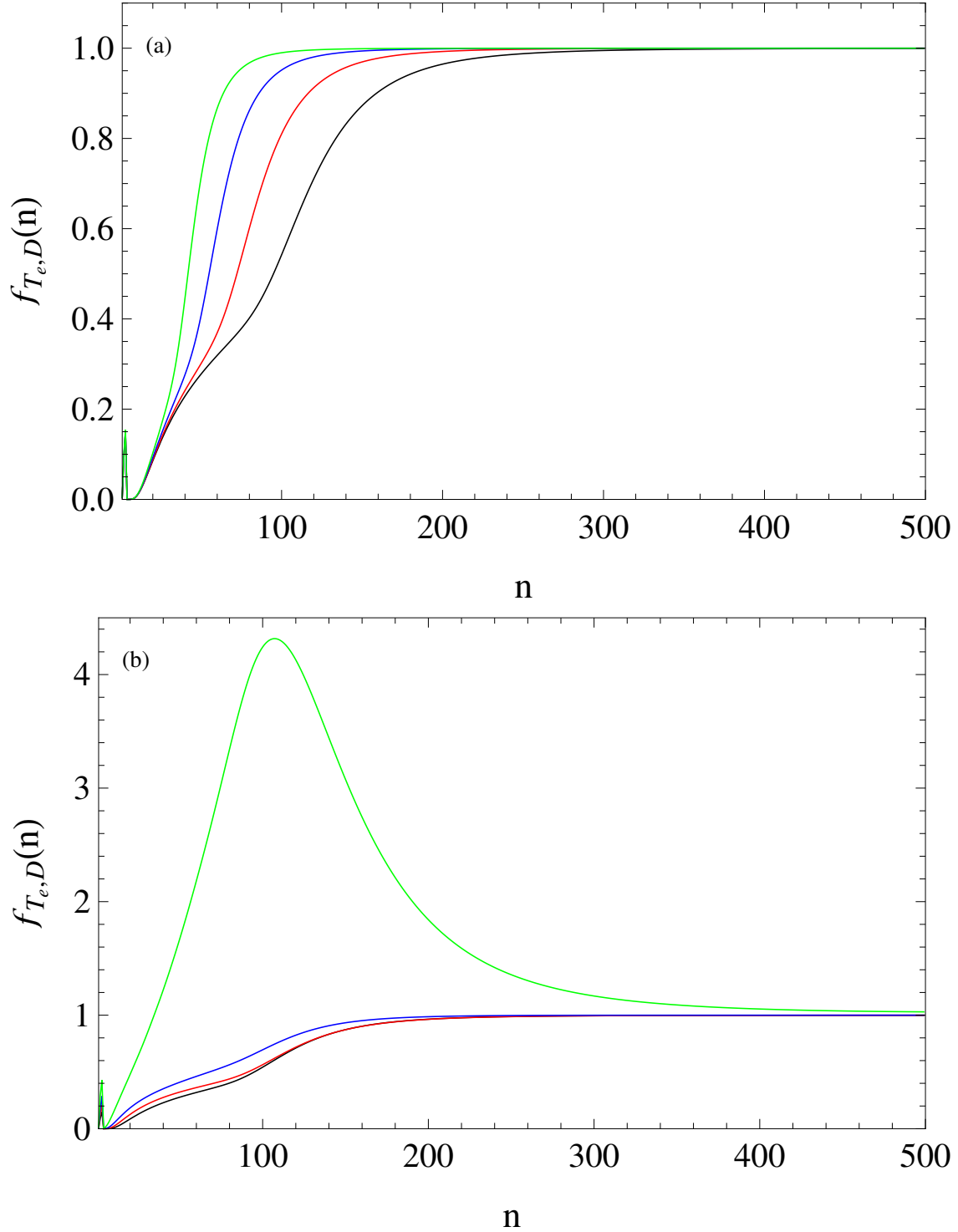
Figure 4.2: C^{3+} deviation of population distribution for different densities and temperatures. The black, red, blue and green solid lines in (a) are corresponding to densities 2.19×10^4, 2.19×10^5, 2.19×10^6 cm^{-3} and 2.19×10^7 with the same temperature 4500 K (0.39 eV), respectively. And in (b) these lines are for temperatures 4500K (0.39 eV), 6300 K (0.54 eV), 9000K (0.78 eV) and 13500 K (1.16 eV) with the same density 21900 cm^{-3} respectively.

Ion stage	Resonances	Energy below (eV)	Rydberg n	Promising?	Reason	Wavelength of Main line (A)	Wavelength of Satellit line (A)	Wavelength of Valence line (A)
B^{2+}-B^+	2p3d(^{3}P)	0.2697	14.2	No	Not in Ryd-cont			
C^{3+}-C^{2+}	2p4d(^{3}F)	0.051	49	**Yes**		1550.77,1548.19	1552.8,1623.0	
	2p4d(^{1}D)	0.053	48	**Yes**			1553.0,1623.25	
	2p4p(^{1}D)	0.0748	40.5	**Yes**			1474.0,1581.4	
	2p4p(^{3}P)	0.233	22.9	No	Not in Rydberg continuum			
	2p4p(^{3}D)	0.529	15.2	No				
N^{4+}-N^{3+}	2p4d(^{1}P)	3.264	8.2	No	Not in Ryd-cont			
O^{5+}-O^{4+}	2p5d(^{1}F)	1.52	12	No	Not in Ryd-cont			
F^{6+}-F^{5+}	2p6p(^{3}P)	0.036	117	**Yes**		890.79,883.11	885.795	
	2p6p(^{3}D)	0.15	57	**Yes**				
Ne^{7+}-Ne^{6+}	2p6p(^{3}S)	2.82	15.3	No	Not in Ryd-cont			
Na^{8+}-Na^{7+}	2p6d(^{1}F)	5.9	12.1	No	Not in Ryd-cont			
Mg^{9+}-Mg^{8+}	2p7d(^{1}F)	2.14	22.7	?				
Al^{10+}, Si^{11+} P^{12+}, S^{13+}		>40		No	Not in Ryd-cont			

Table 4.1: Table of Li-like ions showing the presence of below threshold doubly excited states with the energies provided by the NIST database [14].

Ion stage	Resonances NONE CLOSE	Energy below (eV)	Rydberg n	Promising ?	Reason	Wavelength of Main line (A)	Wavelength of Satellite line (A)	Wavelength of Valence line (A)
B^+-B				No	Not in Ryd-cont			
C^{2+}-C^+	$2s2p(^3P)3d(^4D)$	0.0144	61.5	**Yes-V**		190.87	196	64.1-65.1 986.3-989.2
		0.11	22.2	**Yes-V**				
N^{3+}-N^{2+}	$2s2p(^3P)4p(^2D)$	0.1563	28	**Yes-V**				
O^{4+}-O^{3+}	$2p^2(^3P)3d(^4S)$	0.93	15.3	No	Not in Ryd-cont	75.87-76.2	67.48,70.2 72.49,75.3	
	$2p^2(^3P)3d(^4D)$	1.11	14.1	No	Not in Ryd-cont			
F^{5+}-F^{4+}	$2s2p(^3P)5d(^4P)$	1.94	13.2	No	Not in Ryd-cont			
Ne^{6+}-Ne^{5+}	$2s2p(^3P)5d(^2F)$	5.834	9.2	No	Not in Ryd-cont			
Na^{7+}-Na^{6+}	$2p^2(^3P)4d(^4P)$	1.656	20.1	No	Not in Ryd-cont +perhaps hard to resolve from main line	49.23-49.978	48.42 48.43 48.56 48.57 49.00,49.15	
Mg^{8+}-Mg^{7+}	$2s2p(^1P)5d(^2D)$	1.538	23.8	No	Not in Ryd-cont+perhaps hard to resolve from main line	36.8076	36.3822	
Al^{9+}, Si^{10+}, P^{11+}, S^{12+}		>30		No	Too far below threshold			

Table 4.2: Table of Be-like ions showing the presence of below threshold doubly excited states with the energies provided by the NIST database [14].

4.3 Modeling of the satellite line intensity

The satellite lines we are interested in are from the transition C^{2+} $1s^2 2p4l$-$1s^2 2s4l$, where l are p, d or f. The satellite line intensity is related to that of main line. The main line is from the transition C^{3+} $1s^2 2p(^2P_{3/2,1/2})$-$1s^2 2s(^2S_{1/2})$. Considering first the intensity of the main (resonance) line:

$$I_{2p-2s}^{C3+} = N_{2s}^{C3+} \left(\frac{N_{2p}^{C3+}}{N_{2s}^{C3+}} \right) A_{2p-2s}^{C3+} \tag{4.7}$$

where N_{2s}^{C3+} is the ground state population of C^{3+}, $(N_{2p}^{C3+}/N_{2s}^{C3+})$ gives the fraction of the C^{3+} ions in the excited 2p state and A_{2p-2s}^{C3+} is the Einstein A coefficient for the 2p$\to$ 2s transition. If the plasma is in a low density environment, then coronal conditions hold for the excited populations. Thus, the only excitation mechanism of the excited states is collisional excitation from the ground (described by a collisional excitation rate coefficient q_{2s-nl}^{C3+}, and the only depopulating mechanism is spontaneous emission from the excited states. In these circumstances, the line intensity simpifies to

$$I_{2p-2s}^{C3+} \approx N_{2s}^{C3+} \frac{N_e q_{2s-2p}^{C3+}(T_e)}{A_{2p-2s}^{C3+}} A_{2p-2s}^{C3+} \tag{4.8}$$

$$= N_e N_{2s}^{C3+} q_{2s-2p}^{C3+} \tag{4.9}$$

Considering next the satellite line intensity, the focus is on systems where the doubly excited state can only be populated from dielectronic capture (α_i) from the N_{2s}^{C3+} ground state and it is only depopulated via Auger breakup (A^a) back to this state and radiative decay (A^r) to a lower level of C^{2+}. This is analogous to the Coronal expression for excited states, but based upon a different driving populating mechanism. It is also likely to be valid up to higher electron densities than the coronal approximation due to the large Auger rates that determine the timescales.

If level i is the doubly excited state then the rate of change of population in the doubly excited state is given by

$$\frac{dN_i^{C2+}}{dt} = N_{2s}^{C3+} N_e \alpha_i - N_i(A^a + \sum_{j<i} A_{i\to j}^r) \qquad (4.10)$$

The doubly excited state will reach a steady state value very quickly because the Auger rates are very large. So we can set $(dN_i^{C2+})/(dt) = 0$ in the previous equation and solve for the doubly excited population density N_i.

$$N_i = \frac{N_e N_{2s}^{C3+} \alpha_i}{A_{i\to 2s}^a + \sum_{j<i} A_{i\to j}^r} \qquad (4.11)$$

This can be used to generate a satellite line intensity via

$$I_{2p4l\to 2s4l}^{Satellite} = \frac{N_e N_{2s}^{C3+} \alpha_i}{A_{i\to 2s}^a + \sum_{j<i} A_{i\to j}^r} A_{2p4l\to 2s4l}^r. \qquad (4.12)$$

It is useful to consider the ratio of the satellite line to the resonance line:

$$\frac{I_{2p4\ell\to 2s4\ell}^{Satellite}}{I_{2p\to 2s}^{Main}} = \frac{\frac{N_e N_{2s}^{C3+} \alpha_i}{A_{i\to 2s}^a + \sum_{j<i} A_{i\to j}^r} A_{2p4l\to 2s4l}^r}{N_{2s}^{C3+} (\frac{N_{2p}^{C3+}}{N_{2s}^{C3+}}) A_{2p-2s}^{C3+}} \qquad (4.13)$$

Which can be evaluated using a collisional-radiative calculation for the C^{3+} excited populations and a set of Auger and radiative rates. The plasmas of interest in this work are mostly low density (e.g. planetary nebulae). So the coronal approximation is expected to be valid. In this case the line ratio of the satellite line to the main line becomes:

$$\frac{I_{2p4l\to 2s4l}^{Satellite}}{I_{2p\to 2s}^{Main}} = \frac{\frac{N_e \alpha_i}{A_{i\to 2s}^a + \sum_{j<i} A_{i\to j}^r}}{q_{2s-2p}^{C3+}} A_{2p4l\to 2s4l}^r \qquad (4.14)$$

The work of Pindzola et al. [122] contains below threshold recombination rate coefficients for C^{3+} recombining into C^{2+}. Thus, we use those Auger and radiative rates, along with C^{3+} electron-impact excitation rates in a code that was written to evaluate the satellite line intensities relative to the resonance line intensities.

Note that the driving population mechanism for both the satellite line and the resonance line intensity is the ground state of C^{3+}. Thus, the line ratio just depends upon the 2s-2p collisional excitation rate in C^{3+}, the Auger and radiative rates for C^{2+}, and the negative energy distribution function. It should thus be possible to make a direct comparison of the satellite line intensity and the nearby resonance line. Note that if the densities are higher than coronal conditions allow, but not high enough for collisional-redistribution of the populations in the doubly excited state, then the more general equation (4.13) should be used, with a collisional-radiative calculation giving the C^{3+} excited populations.

This more general approach was also included in the spectral modeling code, and reproduced the coronal line intensity ratios at low electron densities. Results from this code will be shown in section 4.4. Figure 4.3 shows the satellite line intensities compared with the C^{3+} resonance line intensities for a range of electron temperatures. Note that below about 0.8 eV the satellite lines would become stronger than the resonance lines.
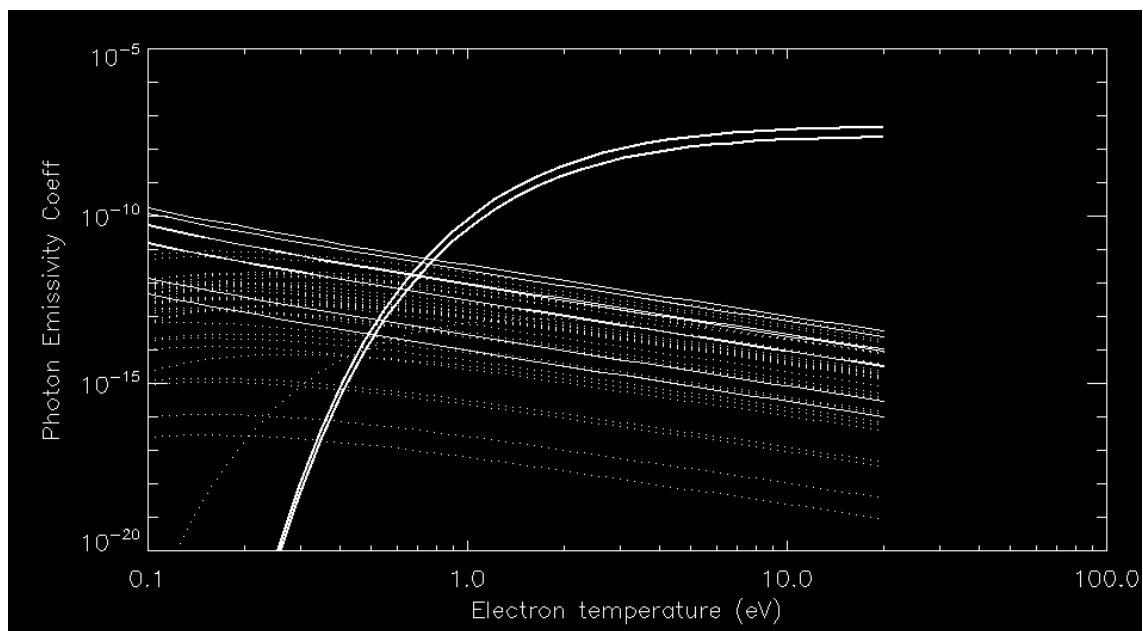
Figure 4.3: Figure showing the relative intensities of the below threshold satellite lines in comparison with the C^{3+} resonance line intensities. The thick solid lines show the intensities of the two resonance lines. The thin solid lines show the intensities of the below threshold satellite lines and the dotted lines show the intensities of the above threshold satellite lines.

Ion stage	Resonances	Comments
Below threshold satellite line		
$1s^22p(^2P)4d(^3F)$-$1s^22s4d(^3D)$	1553.38 (4-3), 1553.38 (2-3), 1552.81 (2-2), 1552.44 (2-1), 1553.38 (3-3), 1552.81 (3-2)	1 May be in the same observing range as the main lines. 2 Promising line for observatio
$1s^22p(^2P)4d(^3F)$-$1s^22s4d(^1D)$	1623.02A (4-2, 2-2, 3-2)	Weak because spin changes
$1s^22p(^2P)4d(^1D)$-$1s^22s4d(^3D)$	1553.6 (2-3), 1553.0 (2-2), 1552.7 (2-1)	1 May be in the same observing range as the main lines. 2 Weak because spin changes.
$1s^22p(^2P)4d(^1D)$-$1s^22s4d(^1D)$	1623.25	Promising line for observation
$1s^22p(^2P)4p(^1D)$-$1s^22s4p(^3P)$	1471.1 (2-2), 1474.0 (2-1)	Weak because spin changes
$1s^22p(^2P)4p(^1D)$-$1s^22s4p(^1P)$	1581.43	Can not be resolved from above threshold satellite line

Table 4.3: Below threshold satellite lines for C^{2+}

4.4 Comparison with existing observations

As noted above, C^{3+} was selected as a good candidate for a search for below threshold satellite lines. This ion has doubly excited states above and below threshold that could produce satellite lines. All of these are $1s^22p$ nl doubly excited states with strong core radiative decay rates via a 2p-2s core decay. Thus, the branching ratio to populate the below threshold states via cascades from the higher levels is extremely small. The densities are also too low for collisional redistribution to populate these states from nearby levels. That is, the only mechanism to populate the below threshold states is below threshold dielectronic recombination. Thus, an observation of a satellite line from one of these below threshold states should be strong evidence of the below threshold recombination mechanism. Table 4.3 gives a detailed list of the spectral lines that could be emitted from the below threshold doubly excited states and Table 4.4 gives a list of the spectral lines from the above threshold doubly excited states.

Ion stage Above threshold satellite line	Resonances	Comments
$1s^22p4d(^3D)-1s^22s4d(^3D)$ $1s^22p4d(^3D)-1s^22s4d(^1D)$	1508.62 (1-1), 1508.97 (1-2), 1508.976 (3-2), 1509.50 (3-3),1508.62 (2-1), 1508.62 (2-1), 1508.62 (2-1), 1508.97 (2-2),1509.50 (2-3) 1575.19	
$1s^22p4f(^3G)-1s^22s4f(^3F)$ $1s^22p4f(^3G)-1s^22s4f(^1F)$	1512.51 (4-3), 1512.70 (4-4), 1512.37 (3-2), 1512.51 (3-3),1512.70 (3-4), 1512.70 (5-4) 1528.5	
$1s^22p4f(^3F)-1s^22s4f(^3F)$ $1s^22p4f(^3F)-1s^22s4f(^1F)$	1511.30 (2-2), 1511.43 (2-3), 1511.02 (3-2), 1511.16 (3-3),1511.35 (3-4), 1510.46 (4-3), 1510.66 (4-4) 1527.14	
$1s^22p4d(^3P)-1s^22s4d(^3D)$ $1s^22p4d(^3P)-1s^22s4d(^1D)$	1490.72 (0-1), 1490.72 (2-1), 1491.06 (2-2), 1491.58 (2-3),1490.7 (1-1), 1491.06 (1-2) 1555.56	
$1s^22p4d(^1F)-1s^22s4d(^3D)$ $1s^22p4d(^1F)-1s^22s4d(^1D)$	1484.86 1548.9	
$1s^22p4f(^3D)-1s^22s4f(^3F)$ $1s^22p4f(^3D)-1s^22s4f(^1F)$	1477.88 (3-2), 1478.01 (3-3), 1478.19 (3-4), 1476.72 (2-2),1476.84 (2-3), 1476.4 (1-2) 1492.10	
$1s^22p5p(^1P)-1s^22s5p(^3P)$ $1s^22p5p(^1P)-1s^22s5p(^1P)$	1582.41 1558.3	Blended with below threshold satellite line 1581.43

Table 4.4: Above threshold satellite lines for C^{2+}
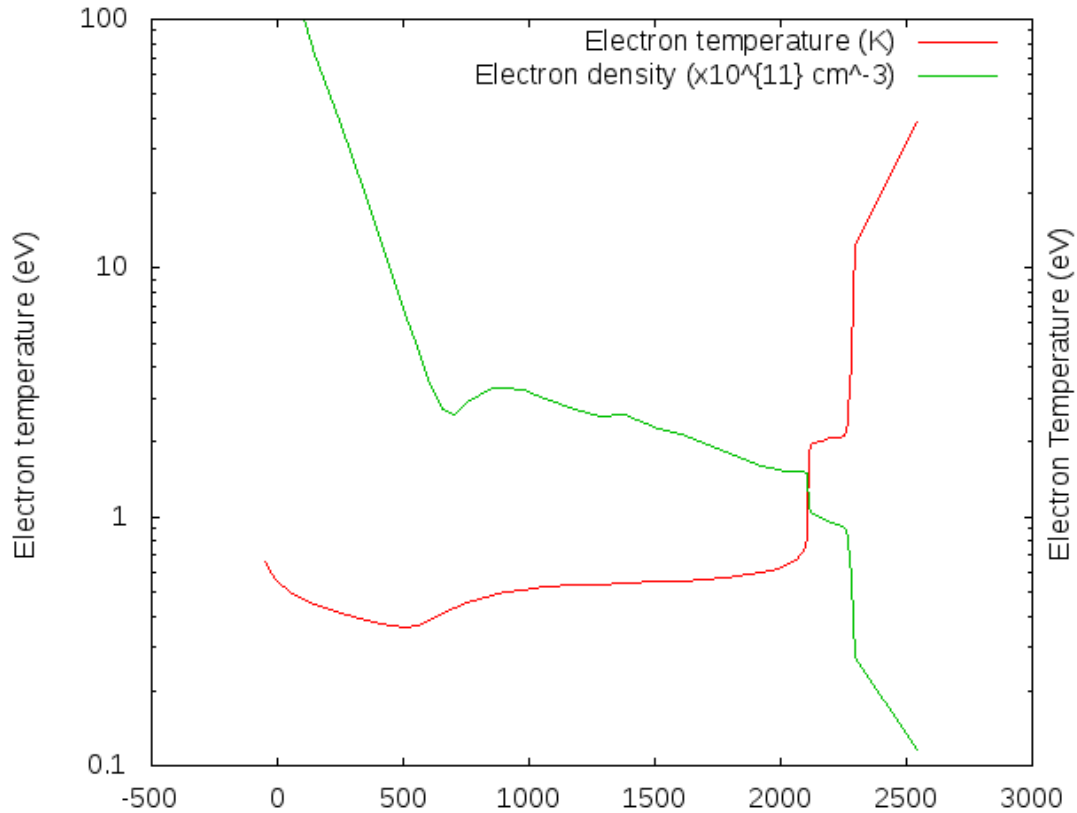
Figure 4.4: Solar atmosphere temperature and density profile, taken from Vernazza and Averett [127].

One of the challenges with observing the lines shown in these tables is that they emit in the Extreme Ultraviolet. Thus, ground based observations are unlikely to detect them. We also require high wavelength resolution due to the proximity of the satellite lines from the main C^{3+} resonance line. Thus, we look at two case studies. The first is a solar atmosphere observation using the SUMER instrument on the SOHO telescope. This is a collisionally ionized plasma with a sharp temperature gradient. Figure 4.4 shows the temperature and density profile from the Vernazza et al. [127] of the solar atmosphere.

The second example is of a low density photoionized plasma in planetary nebula Abell 30, with observations from the IUE instrument [121]. The wavelength resolution is much lower in these observations, but the plasma conditions are much more suitable for the observation of these below threshold satellite lines.

4.4.1 First case study: emission from the solar atmosphere

High resolution EUV observations were taken of the solar atmosphere and a comrehensive line identification taken by Curdt et al. [128]. Figure 4.5 shows the spectrum in the wavelength region of interest. The two strong C^{3+} resonance lines are strong and resolvable. There are numerous weak spectral lines at nearby wavelengths. Fig. 4.6 shows a synthetic (stick plot) spectrum plotted on the observed spectral lines. These results are shown for an electron temperature of 0.8 eV. Note that there are spectral features that line up with the predicted below threshold satellite lines. Curdt et al [128] identify these as either being Fe II lines or high-n shell transitions of Si I. The latter identification seems unlikely due to the very high n-shells involved.

A more serious problem with the above comparison is that the C^{3+} ions would not exist at 0.8 eV in the solar atmosphere. In a collisionally ionized plasma one would expect C^{3+} to exist closer to 8 eV. Thus, we constructed a line of sight model that includes the temperature and density profile of the solar atmosphere, using the model of Vernazza et al. [127]. That is, we use the equation

$$I_{i \to j} = \int_0^{3000km} N_e(r) \left(\frac{N_{2p}^{C3+}}{N_{2s}^{C3+}} \right) \left(\frac{N^{C3+}}{N_C^{TOT}} \right) N_C^{TOT}. \tag{4.15}$$

In this case the satellite line intensities become a lot smaller than the C^{3+} resonance lines, see Figs. 4.5 and 4.6. This is due to the C^{3+} fractional abundance peaking at the part of the atmosphere where the electron temperature is about 8 eV, at which temperatures the satellite lines are very weak. It seems unlikely that below threshold satellite lines would be strong in any collisionally ionized plasmas. An interesting caveat to this is discussed in chapter 5, where we show a rise in the negative energy distribution function for high electron temperatures.

Note that the resonance lines peak in intensity at the upper part of the atmosphere, where the temperature is large enough for C^{3+} to form. The satellite line in this model would

C IV 2p–2s lines

C III below threshold satellite lines

C3+ fractional abundance/1.e6
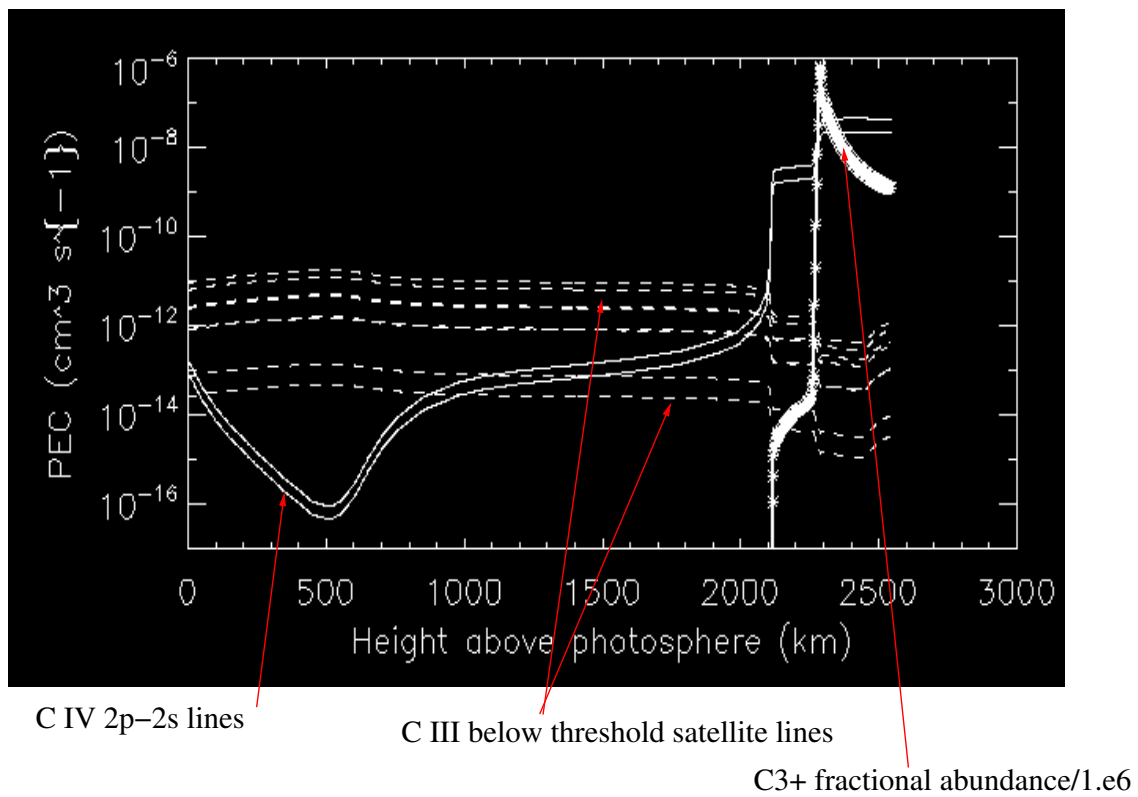
Figure 4.5: Plot of the emissivity of the C^{3+} resonance lines and the C^{2+} satellite lines through the solar atmosphere.
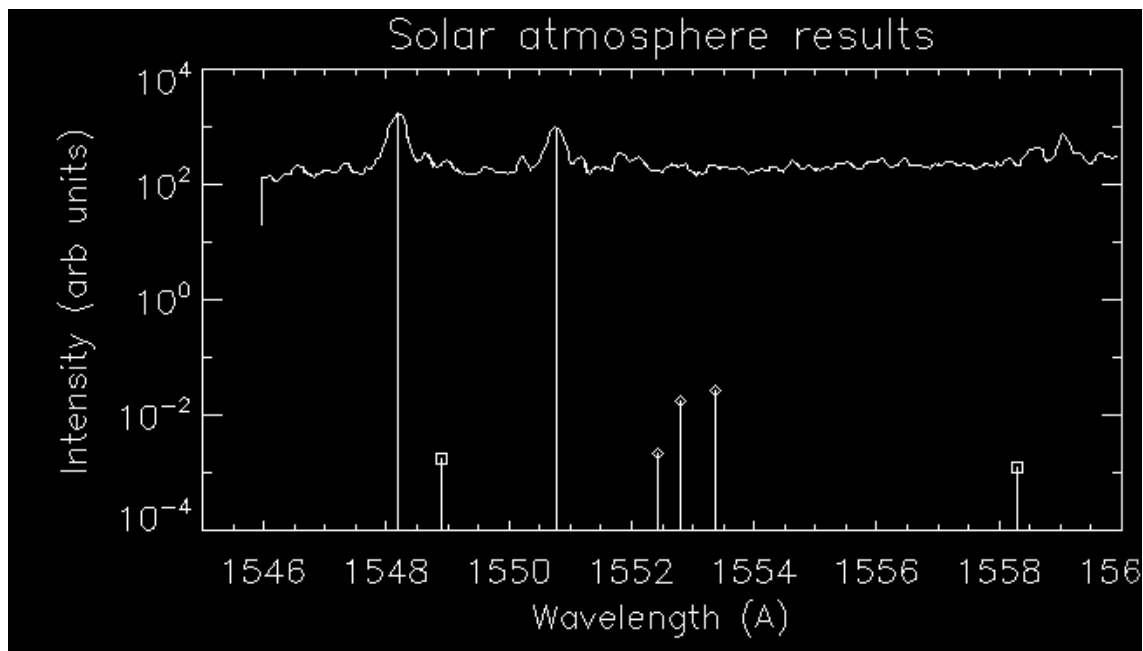
Figure 4.6: Line intensity of the C^{3+} spectral lines, normalized to the observed SUMER spectrum. Also shown on the plot are the satellite line intensities. All calculated intensities have the line of sight temperature and density profile included.

be much too small to be observed. Figure 4.6 shows the intensity of the satellite lines once the line of sight temperature distribution has been accounted for.

This seems likely to be the case for all collisionally ionized plasmas for C^{3+}. Thus, one would either need an ion which exists at a lower temperature (i.e. at a temperature closer to that where the satellite line intensities would be strong), or a plasma that has a different mechanism for generating the higher charge states of C. Astrophysical photo-ionized plasmas such as planetary nebulae are good candidates for this latter option. The light from the star can photoionize the ions in the surrounding gas cloud to higher charge states, while the gas cloud has a low electron temperature. Thus, we will consider such an example next for our search.
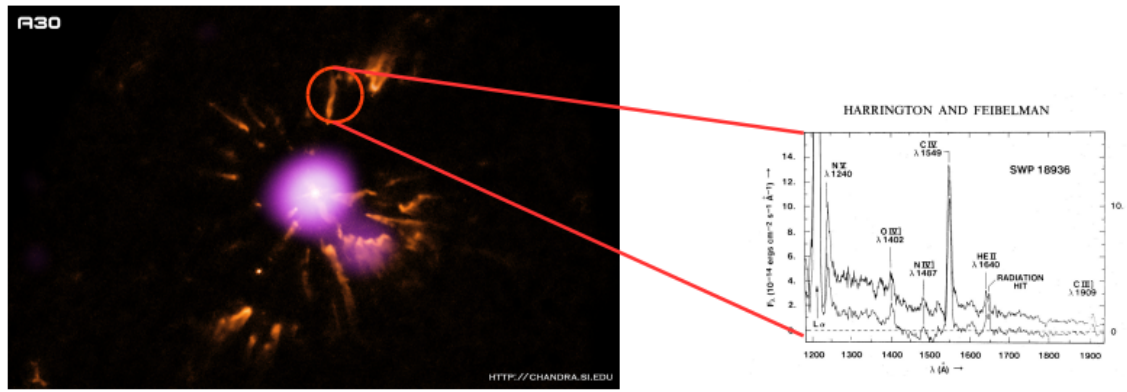
Figure 4.7: Hubble Space Telescope image of Abell 30, with the knot of plasma that is of interest marked. Also shown is the UV spectrum taken from Harrington and Feibelman [121].

4.4.2 Second case study: emission from a plama knot in Abell 30

There are a set of planetary nebulae referred to as 'born again planetary nebulae'. They provide an excellent environment to search for below threshold satellite lines. Figure 4.7 shows some images of these born again nebulae. They have hydrogen-deficient knots of plasma which were ejected by a late thermal pulse and are embedded in a fast stellar wind [119]. Thus, there is a large H-rich outer nebula which surrounds irregularly shaped H-deficient structures closer to the star. These inner knots will have increased abundances of carbon and there is already observational evidence of the C^{3+} resonance lines [121].

The temperature in these knots is subject to some debate, see Harrington and Feibelman [121]. Harrington and Feibelman [121] showed that the electron temperature derived from C IV λ 1549 / C III λ 4650 lines in knot 3 was 10,600K, Similarly the T_e derived from the C III λ 1909 / C II λ 4267 lines was 7,800 K. However, these were in marked contrast from the temperatures derived from Ne IV lines (which gave T_e=18,300 K), or from O III lines (which gave T_e = 16,400 K). They speculate that one solution to this discrepancy would be *"to postulate the existence of some as yet undiscovered process which augments the carbon recombination lines"*. Harrington and Feibelman also point out that the line intensity of CII λ 1909 is uncommonly weak compared with the C IV λ 1549 Å line. They look for a

mechanism to reduce the intensity of the λ 1909 Å line, but cannot find a good candidate. A different possibility is that the 1549 Å line is enhanced through the presence of satellite lines that could not be resolved in the IUE spectrum used by Harrington and Feibelman [121]. Thus, it may be that unresolved spectral lines could explain some of the discrepancies in existing studies of the knots in Abell 30.

Note that we require spectra of just the knot(s). If light from the star is included, the spectra would be dominated by the strong stellar spectral lines and the weak satellite lines would not be detectable. This limits the spectra available for such a study. After a search through the NASA databases, one such UV observation was obtained. The IUE spectromter was used to observe knot number 3 in Abell 30 and reported by Harrington and Feibelman [121]. The raw data was downloaded and processed in the same manner as reported by Harrington and Feibelman [121]. This required removing signals at the bottom of the detector that had let in some stray stellar light. The remaining spectra was estimated to contain a 3.6% contamination of stellar light. Thus, separate IUE observation of just the star was used to subtract this background stellar light. The resulting spectrum can be see in in Fig. 4.8. In the synthetic spectrum, we used the model described above, with the Auger and radiative rates of Pindzola et al. [122]. For the comparison with the measured spectrum we have convolved the synthetic spectrum with the intrument resolution of IUE. Note that while the satellite line intensity is predicted to be significant, the resolution of the IUE observations is too low to be able to separate the lines. The observed line profile does have an asymmetry to it at the correct position, but the uncertainties are too large to draw any definite conclusions.

Thus, we believe that this is a promising object for future high resolution UV measurements. Figure 4.9 shows a synthetic spectrum for a higher resolution instrument. We have used to resolution of the STIS instrument on the Hubble Space Telescope. The below threshold satellite lines would be easily resolvable.
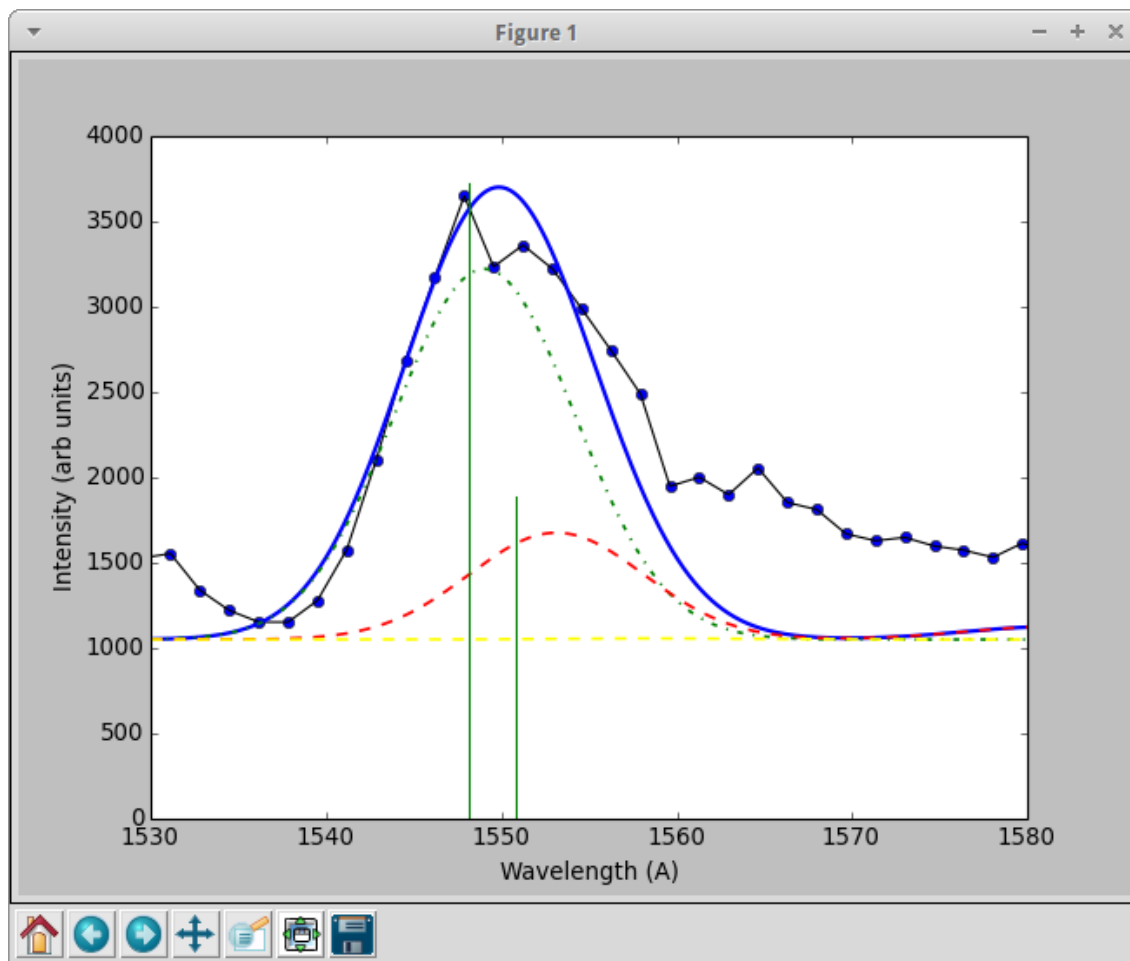
Figure 4.8: Synthetic spectrum compared with the Abell 30 IUE spectral measurements of Harrington and Feibelman [121]. The red line is the below threshold satellite line contribution, the green shows the resonance lines and the blue shows the total line intensity.
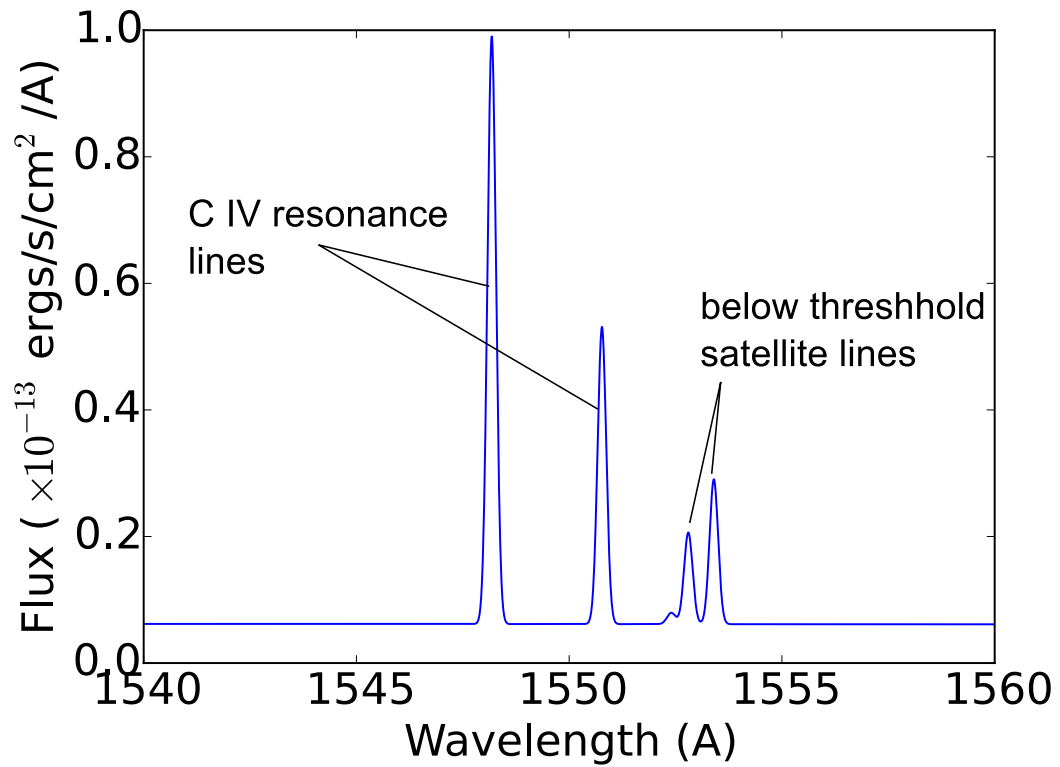
Figure 4.9: Synthetic spectrum of the knot in Abell 30, with the spectral resolution of STIS, assuming an electron temperature of 9,200K.

As a result of this work a proposal was submitted requesting observing time on the Hubble Space Telescope, see Appendix C. It was not selected, but it is our intention to refine the proposal and submit it again.

4.5   Conclusions

In summary, the use of below threshold satellite lines as a means to prove the existence of below threshold satellite lines is a promising avenue of research. We have identified a number of systems that would be interesting to pursue further. Of these, C^{3+} is the most promising though falls in a challenging wavelength range. For C^{3+} it appears to be unlikely that such lines would be observed in collisionally ionized plasmas, but photoionized plasmas have the right plasma conditions. We have completed an initial study of a knot of plasma in Abell 30. While the lines are predicted to be strong, the best available spectroscopic observations are not of high enough resolution to identify the lines. Higher resolution observations of Abell 30, or similar planetary nebulae would be a promising area of future study.

Chapter 5

THE CONTRIBUTION OF NEAR THRESHOLD RESONANCES TO DIELETRONIC RECOMBINATION RATE COEFFICIENT

5.1 Background

In this chapter the focus is on first identifying ions that may be missing contributions to their DR rate coefficients due to near threshold resonances. Once a subset of ions are identified two cases are taken to demonstrate how revised rate coefficients can be evaluated with the inclusion of below threshold recombination. Of particular interest is the finding of Robicheaux et al. [12] for Mg^{8+} that the inclusion of below thresold recombination has the potential to remove the sensitivity of low temperature DR rate coefficients to small changes in the energy positions of the near threshold doubly excited states.

That is, the purpose of this chapter is not to develop a more accurate theoretical method that can calculate near threshold energy level positions, but to investigate the contribution of below threshold resonances to the DR rate and determine if it removes the hyper dependence on resonance position. The process of below threshold recombination has been described in chapter 4. We mention here the two main items that need to be calculated for below threshold DR rate coefficients to be generated: Below threshold Auger rate coefficients and negative energy distribution functions. As mentioned previously, the second of these requirements can be generated by ADAS204. Negtive energy Auger rates are produced by modifying the AUTOSTRUCTURE code [16], so that the appropriate matrix element is evaluated.

We note that there are three possible scenarios in the currently existing data. An ion may have no near threshold resonances (either above or below), in this case the existing DR rate coefficients are expected to be accurate. Note that an useful outcome of this work is the identification of this list of ions. Modelers can then use the DR data for these ions with

confidence. The second scenario is that there are some resonances just below the ionization potential that have been ommitted from current calculations. In this case the DR rates have been underestimated. Lastly, it is possible that there are resonances that are very close to threshold and small changes in the structure can move them either above or below threshold. In this case one would expect existing calculations of such DR rate coefficients to have a large scatter. The inclusion of below threshold recombination should remove much of this sensitivity, while also producing more accurate rate coefficients.

Thus, our first step will be to search for problematic cases, namely ions with near threshold resonances. If an ion has near threshold resonance or resonance within the Rydberg continuum, we consider it as a case of which the DR rate needs to be corrected. In this paper, we will use a combination of the NIST energies [14] and the resonance positions as produced by the AUTOSTRUCTURE code [16] to identify which are the problematic cases in the Li-like and Be-like sequences. After that, we select two examples from these problematic cases, C^{3+} and Mg^{8+}, to investigate. The tools used to calculate the DR rate from below threshold resonances are ADAS 204 and the modified AUTOSTRUCTURE codes. The ADAS 204 code provides us the population distribution function for the negative energy electrons, with which the modified AUTOSTRUCTURE code and post-processor can produce DR rate coefficients for below threshold resonances.

The rest of this chapter is organized as follows. In Sec. 5.2, we introduce the method for identifying the problematic cases, and list those ions for the Be-like and Li-like iso-electronic sequences. Two cases, C^{3+} and Mg^{8+} are selected for re-evaluation of their DR rates with the inclusion of below-threshold resonances in Sec. 5.3. We also propose a possible verification of our corrected rates using experiments in Sec. 5.4. The last section contains a summary and outlook for the future work.

5.2 Identifying ions in Li-like and Be-like sequences with near threshold resonances

We suspect an ion to be a problematic case when it has a near threshold resonance (ie slightly positive energies) or a resonance within the Rydberg continuum (ie. slightly negative energy). A direct way to identify the problem ions is to check if they have either of the two features. The best tool should be the NIST levels, because the NIST values for levels are the most accurate to our knowledge. However, the levels listed on NIST are incomplete. Not all the levels are included, and some important ones are missing. This disadvantage can be remedied by using the resonance distribution produced by the modified the AUTOSTRUCTURE code. The modified AUTOSTRUCTURE code can predict the positions of all possible below and above threshold resonances. However, the values are not as accurate as those from NIST. So we combine both the NIST energy levels and resonance distributions from the modified AUTOSTRUCTURE code for the purpose of identifying ions that require further investigation . If the corresponding NIST energy value can be found, we use the value of NIST. If energy levels are missing in NIST, we use AUTOSTRUCTURE energies instead.

We list levels within an energy range around the threshold for different ions in Tables 5.1 and 5.2 (for the Li-like and Be-like sequences, respectively). The corresponding principal quantum numbers for below threshold levels are also given in the tables, which show us if levels are within the Rydberg continuum. We consider $n \geq 20$ for the Rydberg state as an approximate indication of this criteria. We list the configurations as indicated by the AUTOSTRUCTURE calculation. Only those configurations closest to the threshold are listed. The energy range of the Rydberg continuum will be different for different ions. For the two sequences, the energy range is -0.1 Ryd.– 0.1 Ryd. for ions Be^+ – F^{6+} and B^+ – Ne^{6+}; -0.3 Ryd. – 0.3 Ryd. for ions Ne^{7+} – Al^{10+} and Na^{7+} – Si^{10+}. There are also some columns marked with a '-' in the tables. This is used to mark missing levels in NIST.

Ion	Configuration	Autostructure energies (n-shell)	NIST energies (& n-shell)	Conclusion
Be$^+$-Be				No
B^{2+}-B$^+$	2p3p	-0.029 (n=12)	0.00221	Yes
		0.045	0.0538	
	2p3d	-0.0015 (n=52)	-0.0197 (n=14)	
		0.019	0.0202	
C^{3+}−C^{2+}	2p4s	-0.071 (n=11)	-0.0896 (n=10)	Yes
	2p4p	-0.012 (n=27)	-0.01672 (n=23)	
		0.0071	-0.00549 (n=40)	
	2p4d	0.00016	-0.003862 (n=48)	
		0.003937	-0.003782 (n=49)	
	2p4f	0.020	0.01717	
N^{4+}− N^{3+}	2p5s	0.0164	0.0136	Yes
	2p5p	0.0473	0.0454	
	2p5d	0.0768	0.0847	
	2p5f	0.0894	-	
	2p5g	0.0922	-	
O^{5+}−O^{4+}				No
F^{6+}− F^{5+}	2p6s	-0.0326 (n=33)	-	Yes
	2p6p	-0.0068 (n=73)	-0.0112 (n=57)	
		0.0040	-0.002597 (n=118)	
			0.008657	
	2p6d	0.0053	0.01928	
	2p6f	0.0214	-	
	2p6g	0.0233	-	
Ne^{7+}− Ne^{6+}				No
Na^{8+}− Na^{7+}	2p7s	-0.02528 (n=50)	-	Yes
	2p7p	-0.002385 (n=164)	-	
		0.003339	-	
	2p7d	-0.00883 (n=85)	-	
		-0.00305 (n=145)	-	
		0.004013	-	
	2p7f	0.005939	-	
	2p7g	0.007865	-	
	2p7h	0.007865	-	
	2p7i	0.007865	-	
Mg^{9+}− Mg^{8+}	2p7s	-0.2244 (n=19)	-	Yes
	2p7p	-0.1691 (n=22)	-1.6825* (n=7)	
	2p7d	-0.1547 (n=23)	-0.1569 (n=23)	
	2p7f	-0.156 (n=23)	-	
	2p7g	-0.1586 (n=23)	-	
	2p7h	-0.1586 (n=23)	-	
	2p7i	-0.1586 (n=23)	-	
Al^{10+}− Al^{9+}	2p8s	-0.004414 (n=151)	-	Yes
		0.04759	-	
	2p8p	0.01742	-	
	2p8d	0.03347	-	
	2p8f	0.04631	-	
	2p8g	0.04759	-	
	2p8h	0.04695	-	
	2p8i	0.04759	-	

Table 5.1: Identification for problematic ions in the Li-like iso-electronic sequence

Ion	Configuration	Autostructure energies (& n-shell)	NIST energies (& n-shell)	Conclusion
$B^+ - B$				No
$C^{2+} - C^+$	2s2p3d	-0.023 (n=13)	-0.00084 (n=69)	Yes
	2s2p4s	0.024	0.117	
	2s2p4p	0.073	0.162	
$N^{3+} - N^{2+}$	2s2p3p	-0.008 (n=34)	-0.046 (n=14)	Yes
		0.0191	-0.0847 (n=10)	
	2s2p4s	-0.08614 (n=10)	-0.1274 (n=8)	
	2s2p4p	-0.012 (n=27)	-0.03 (n=17)	
		0.1339	-0.011 (n=29)	
	2s2p4d	0.019	0.0122	
	2s2p4f	0.046	0.039	
$O^{4+} - O^{3+}$	$2p^2 3p$	-0.044 (n=19)	-0.068 (n=15)	Yes
		0.22	0.0045	
	$2p^2 3d$	0.051	0.052	
	2s2p5s	-0.0087 (n=43)	-	
		0.013	-	
	2s2p5p	0.040	0.0379	
	2s2p5d	0.081	0.089	
$F^{5+} - F^{4+}$	2s2p 4p	-0.014 (n=42)		Yes
		0.0066	?	
	2s2p4d	0.095	?	
	$2p^2 3p$	-0.054 (n=22)	-0.705* (n=6)	
$Ne^{6+} - Ne^{5+}$	2s2p6s	-0.066 (n=23)	-	Yes
	2s2p6p	-0.010 (n=60)	-	
	2s2p6d	-0.0024 (n=122)	-	
	2s2p6f	0.0149	-	
	2s2p6g	0.0181	-	
	2s2p6h	0.0188	-	
	$2p^2 4s$	0.026	-	
$Na^{7+} - Na^{6+}$	$2p^2$ 4p	0.0129	-0.32414 (n=5)	Yes
		-0.0138 (n=60)		
	$2p^2 4d$	-0.027 (n=43)	-0.116* (n=21)	
		0.148	-	
	$2p^2 4d$	-0.0425 (n=34)	-	
		0.21	-	
	2s2p5s	0.0434	-	
	2s2p5p	0.133	-0.89* (n=7)	
	2s2p5d	0.213	-0.799* (n=8)	
	2s2p5f	0.255	-	
	2s2p5g	0.256	-	
	2s2p6s	-0.012 (n=64)		
		0.0129		
	2s2p6p	-0.237 (n=14)		
	2s2p6d	-0.199 (n=16)	-0.22 (n=15)	
	2s2p6f	-0.193 (n=16)	-	
	2s2p6g	-0.193 (n=16)	-	

	2s2p6h	-0.2065 (n=15)	-	
	2s2p7s	0.072	-	
	2s2p7p	0.1025	-	
	2s2p7f	0.1388	-	
	2s2p7g	0.145	-	
	2s2p7h	0.152	-	
	2s2p7i	0.154	-	
$Mg^{8+}-$ Mg^{7+}	2s2p5p	-0.207 (n=15)	-	Yes
	2s2p5d	-0.11 (n=21)	-0.113 (n=21)	
	2s2p5f	-0.086 (n=24)	-	
	2s2p5g	-0.0806 (n=25)	-	
	2s2p7s	-0.0711 (n=26)	-	
	2s2p7p	-0.031 (n=40)	-	
	2s2p7d	-0.012 (n=64)	-	
		0.0033	-	
	2s2p7f	-0.016 (n=55)	-	
		0.0072	-	
	2s2p7g	-0.016 (n=55)	-	
		0.0091	-	
	2s2p7h	-0.016 (n=55)	-	
	2s2p7i	-0.016 (n=55)	-	
	2s2p8s	0.22	-	
	2s2p8p	0.245	-	
	2s2p8d	0.268	-	
	2s2p8f	0.278	-	
	2s2p8g	0.278	-	
	2s2p8h	0.289	-	
	2s2p8i	0.288	-	
$Al^{9+}-$ Al^{8+}	2s2p 7s	-0.284 (n=15)	-	Yes
	2s2p7p	-0.24 (n=16)	-	
	2s2p7d	-0.195 (n=18)	-	
	2s2p7f	-0.191 (n=18)	-	
	2s2p7g	-0.191 (n=18)	-	
	2s2p7h	-0.224 (n=17)	-	
	2s2p7i	-0.224 (n=17)	-	
	2s2p8s	0.094	-	
	2s2p8p	0.11	-	
	2s2p8d	0.135	-	
	2s2p8f	0.15	-	
	2s2p8g	0.15	-	
	2s2p8h	0.166	-	
	2s2p8i	0.166	-	
	$2p^24d$	-0.11 (n=24)	-	
	$2p^24f$	-0.021 (n=55)	-	
$Si^{10+}-$ Si^{9+}	2s2p6s	0.04	-	Yes
	2s2p6p	0.122	-	
	2s2p6d	0.19	-	
	2s2p6f	0.23	-	
	2s2p6g	0.23	-	
	2s2p6h	0.23	-	
	2s2p8s	-0.015 (n=73)	-	
	2s2p8p	-0.033 (n=50)	-	
		0.0161	-	
	2s2p8d	-0.0027 (n=173)	-	

		0.035	-	
	2s2p8f	-0.016 (n=71)	-	
		0.0024	-	
	2s2p8g	-0.015 (n=73)	-	
		0.0041	-	
	2s2p8h	0.0041	-	
	2s2p8i	0.0041	-	
	2s2p8k	0.0024	-	
	$2p^2 5s$	-0.225 (n=19)	-	
		0.204	-	
	$2p^2 5p$	-0.02 (n=64)	-	
	$2p^2 5d$	-0.04 (n=45)	-	
		0.004	-	
	$2p^2 5f$	0.035	-	
	$2p^2 5g$	0.11	-	

Table 5.2: Identification for problematic ions in the Be-like iso-
electronic sequence

Table 5.1 shows that Be^+, O^{5+} and Ne^{7+} have neither a near threshold resonance nor a below threshold resonance. The other ions in the Li-like sequence require further attention. From Table 5.2, B^+ is the only non-problematic case. So the current DR rates for ions Be^+, O^{5+}, Ne^{7+} and B^+ are reliable, but the DR rates for other ions need to be recalculated by including below threshold resonances to eliminate their sensitivity to energy position and add the contribution to DR rate from negative resonances. It may turn out that for some of these ions the effect is very small, but we identify them as cases that require a closer investigation.

Besides listing the energy levels in the two tables, we also select several cases to plot their AUTOSTRUCTURE resonance positions to demonstrate our method of checking for near threshold resonances. C^{3+} and Mg^{9+} are two ions chosen from Li-like sequence, and O^{4+} and Mg^{8+} are other two ions selected from Be-like sequence. Later in this chapter we will evaluate new rate coefficients for C^{3+} and Mg^{8+}.

The resonance distributions for the four examples are shown in Figures 5.1 and 5.2 : Fig. 5.1 (a) for C^{3+}, Fig. 5.1 (b) for Mg^{9+}, Fig. 2(a) for O^{4+}, and Fig. 2(b) for Mg^{8+}. The line (black line) at the very top of each ion's plot is the resonance distribution for all configurations. The resonance distribution for all configurations is shifted up by 3.5 eV in

Fig. 5.1 (a), 30 eV in Fig. 5.1 (b), 2.5 eV in Fig. 5.2 (a) and 22 eV in Fig. 5.2 (b). This brings any below threshold resonances into view. The color curves with lower baseline of each plot are used for configuration analysis of those resonances, different colors at the same baseline represent different configurations. Two vertical lines are added to every plot to mark the position of the threshold (E=0) and the critical n-shell position for the high Rydberg states (n=20).

In Fig. 5.1 (a), red, blue, green and yellow curves with 0 baseline are for configurations $1s^22p4s$, $1s^22p4p$, $1s^22p4d$ and $1s^22p4f$ respectively. The configuration $1s^22p4s$ (red line) has two resonances below the threshold, the energy of the resonance closer to the threshold in Table 1. The resonance are not likely to be embedded in the Rydberg continuum, so the $1s^22p4s$ levels will not contribute to the DR rate. The configuration $1s^22p4p$ (blue line) has four resonances, three are below threshold and one is above threshold. The resonance above threshold and the first one below threshold (closest to the threshold) are listed in Table 5.1. We consider the above threshold resonance to be near threshold and the first below threshold resonance is within the Rydberg continuum. The configuration $1s^22p4d$ (green line) has six resonances, and all of them are above threshold. We list the first resonance (closest to the threshold) in Table 5.1, and we consider it to be a near threshold resonance. The configuration $1s^22p4f$ (yellow line) has four resonances above threshold, similarly the first resonance energy position is listed in Table 5.1. In summary, there are near (above) threshold resonances (that can cause the DR rate to be sensitive to the small changes in the energies of the resonances) and resonances in the Rydberg continuum (that can contribute to the DR rate) in the recombination $C^{3+} \rightarrow C^{2+}$, so this is a problematic case and its DR rate needs to be recalculated.

Figure 5.2 (a) and (b) show the resonance distributions for O^{4+} and Mg^{8+}, respectively. In Fig.5.2 (a), configurations $1s^22p^23p$, $1s^22s2p5s$, $1s^22s2p5p$, $1s^22s2p5d$ are represented by red, green, yellow and black lines with 0 baseline. The blue line shifted up by 1 is for the configuration $1s^22p^23d$ which is too weak to see if blended with other configurations. Red,
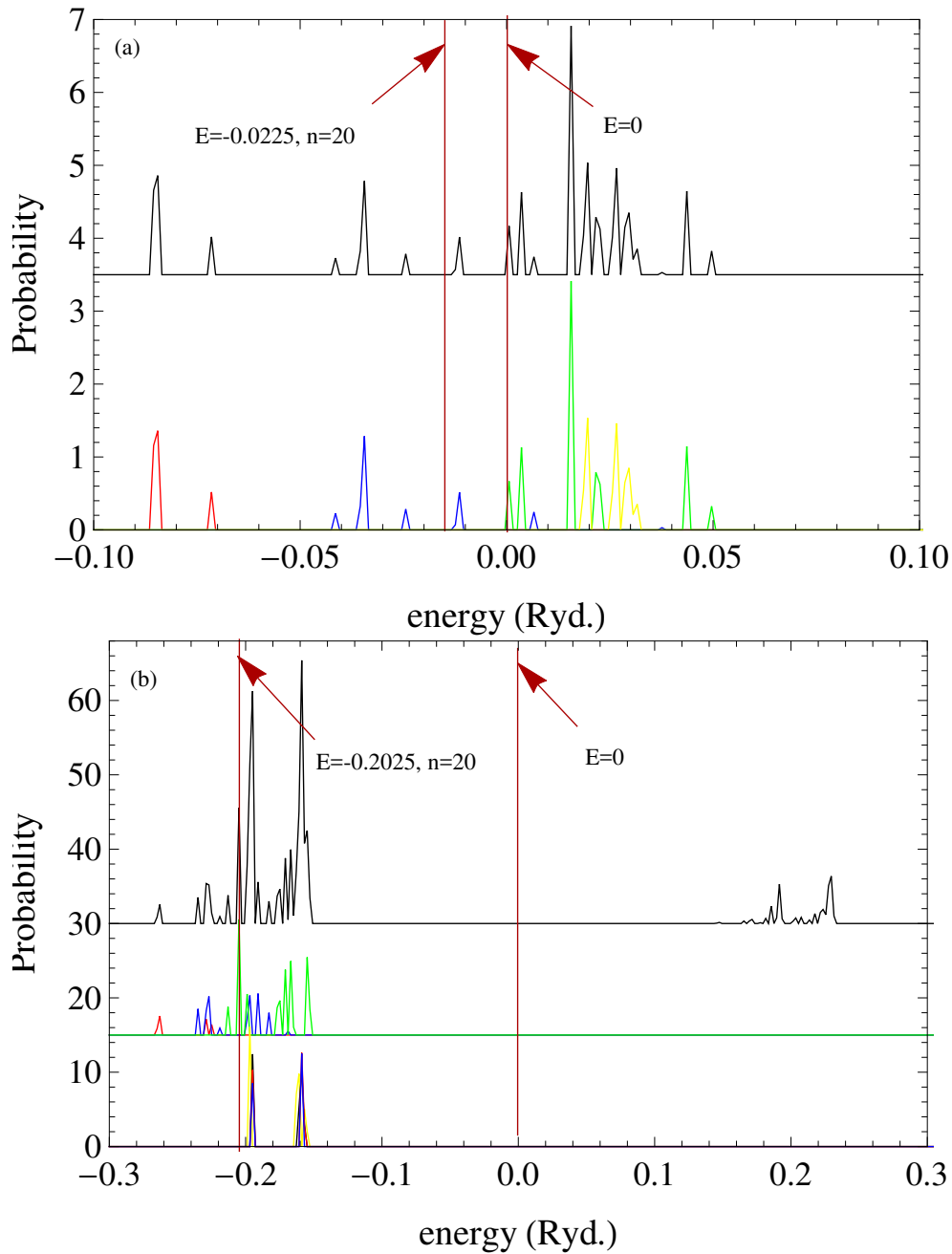
Figure 5.1: The resonance distribution for C^{3+} (a) and Mg^{9+} (b). In (a), red, blue, green and yellow curves with 0 baseline are for configurations $1s^2 2p4s$, $1s^2 2p4p$, $1s^2 2p4d$ and $1s^2 2p4f$ respectively. The configuration $1s^2 2p4s$ (red line) has two resonances below the threshold. In (b), red, blue, green lines with 15 baseline represent configurations $1s^2 2s2p7s$, $1s^2 2s2p7p$ and $1s^2 2s2p7d$ respectively. Configurations $1s^2 2s2p7f$, $1s^2 2s2p7g$, $1s^2 2s2p7h$ and $1s^2 2s2p7i$ are for yellow, black, red, blue lines with 0 baseline.
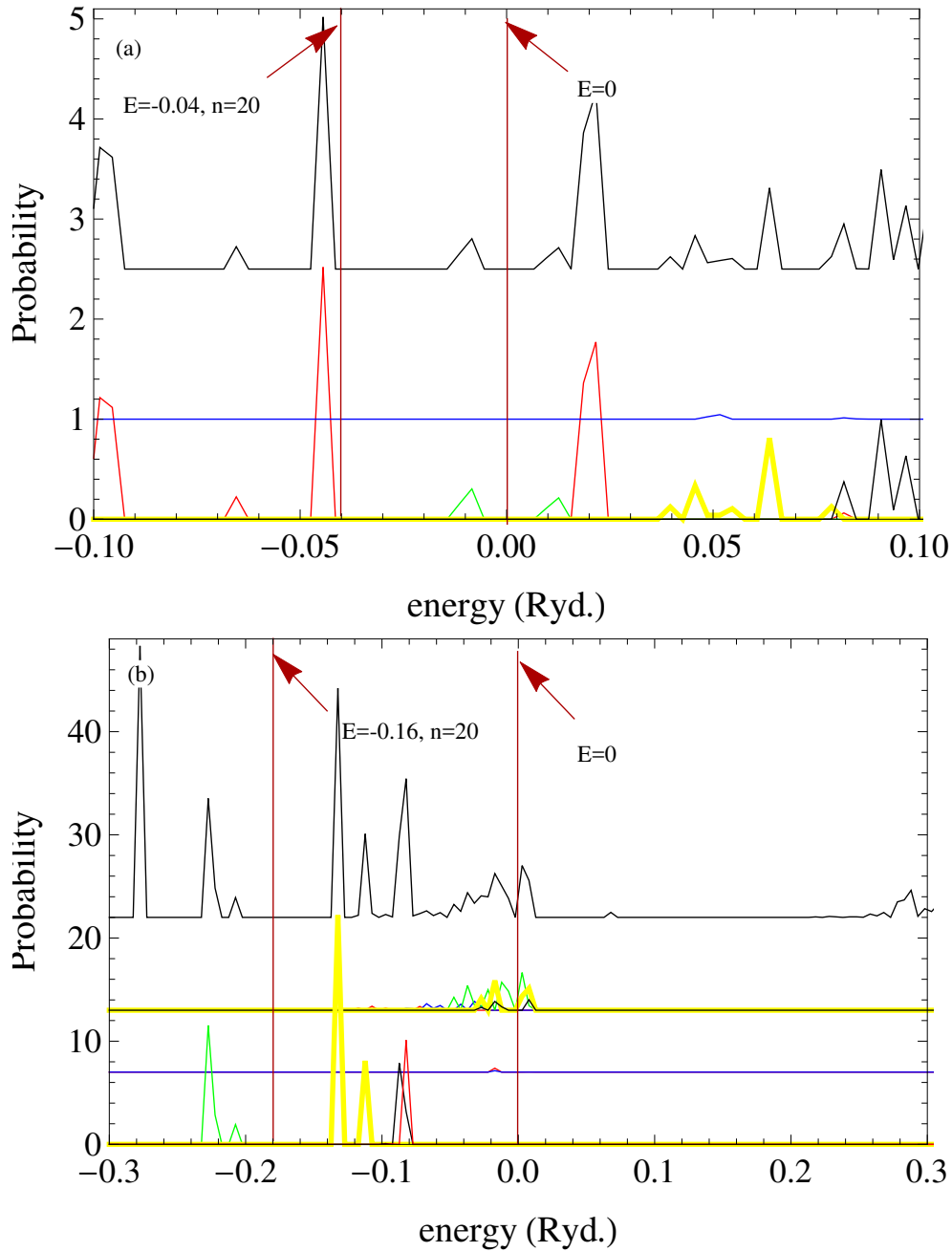
Figure 5.2: The resonance distributions for O^{4+} and Mg^{8+} respectively. In (a), configurations $1s^22p^23p$, $1s^22s2p5s$, $1s^22s2p5p$, $1s^22s2p5d$ are represented by red, green, yellow and black lines with 0 baseline. The blue line shifted up by 1 is for the configuration $1s^22p^23d$ which is too weak to see if blended with other configurations. Red, blue, green and yellow and black lines with 13 baseline in (b) are for configurations $1s^22s2p7s$, $1s^22s2p7p$, $1s^22s2p7d$, $1s^22s2p7f$, $1s^22s2p7g$. Red and blue lines with 7 baseline in the same figure are for configurations $1s^22s2p7h$, $1s^22s2p7i$. Green, yellow, black and red lines with 0 baseline are for configurations $1s^22s2p5p$, $1s^22s2p5d$, $1s^22s2p5f$, $1s^22s2p5g$.

blue, green and yellow and black lines (moved up by 13) in Fig. 2(b) are for configurations $1s^22s2p7s$, $1s^22s2p7p$, $1s^22s2p7d$, $1s^22s2p7f$, $1s^22s2p7g$. Red and blue lines (moved up by 7 for clarity) in the same figure are for configurations $1s^22s2p7h$, $1s^22s2p7i$. Green, yellow, black and red lines with are for configurations $1s^22s2p5p$, $1s^22s2p5d$, $1s^22s2p5f$, $1s^22s2p5g$. The two cases shown in Fig. 5.2 both have above and below threshold resonances, so they are cases deserving further investigation into their rate coefficients.

Figure 5.1 (b) displays the resonance distribution for the recombination $Mg^{9+} \rightarrow Mg^{8+}$. Red, blue, green lines (moves up by 15) represent configurations $1s^22s2p7s$, $1s^22s2p7p$ and $1s^22s2p7d$ respectively. Configurations $1s^22s2p7f$, $1s^22s2p7g$, $1s^22s2p7h$ and $1s^22s2p7i$ are for yellow, black, red, blue lines. This case is not likely to be a problematic case because the resonance distribution is blank around the threshold area. We still group it to be a problematic case because of its high atomic number. High atomic number enables it to have wide high Rydberg state range which includes resonances that may contribute to the DR rate coefficient.

There are three points needing explanation before ending this section. The first one is that the NIST energy values can be quite different from that of the AUTOSTRUCTURE resonance positions for several levels, see the numbers marked with (*). The reason could be that the two values may not correspond to the same level, due to difficulty in deciding upon the label to give the level. The second point to note is that the resonance heights for the levels are not the correct values due to the energy shift applied. We shift the resonances to higher energies just to determine their energy positions and identify the problem cases, with the understanding that the heights will no longer be accurate. When we evaluate the rate coefficients we use the calculated energy positions which will have the appropriate heights. The last point is, for the cases identified to be problematic, we are not sure if their recalculated DR rate by including below threshold resonance effects would change much from their current values. For example, if one case identified to be problematic only has above near threshold resonance but no below threshold resonance (like N^{4+}), the recalculated new

91

DR rate should be the same as that in the current data base. However, calculating the DR rate by including the negative resonance can eliminate the sensitivity to the energy position of the DR rate. For another example, if one case identified to be problematic only has below threshold resonance but no near threshold resonance (like Mg^9+), the recalculated new DR rate could be a little larger than the current value because the population at the below threshold resonance should be low. However, we should explore these cases further by the inclusion of the below threshold resonances.

5.3 New DR rate coefficients for C^{3+} and Mg^{8+}

5.3.1 Theoretical method to calculate DR with below-threshold resonances

The total DR rate coefficient between two ion stages is defined as:

$$DR = (\frac{4\pi a_0^2 I_H}{k_B T_e})^{\frac{3}{2}} \sum_j \frac{\omega_j}{2\omega_\nu} e^{-E_c/k_B T_e} \sum_l A_{j,E_c}^a \frac{A_{j\to l}^r}{\sum_h A_{j\to h}^r + \sum_m A_{j\to m}^a}, \qquad (5.1)$$

where a_0 is the Bohr radius, I_H is Rydberg constant, k_B is Boltzmann constant, T_e is the electron temperature, ω_j and ω_ν are the statistical weight of capturing resonance state (j) and the initial state (ν) of the recombining ion, E_c is the the energy of the resonance state j, A^r and A^a are radiative and Auger rates. The first summation is over the possible resonance states (j) (doubly-excited states), the second one is over all possible bound states that the captured electron can stabilize to (l). The summations over h and m are other Auger and radiative channels. Eq. (5.1) is the traditional definition for DR rate coefficient.

To calculate the DR rate coefficient for below-threshold resonances, the definition will be slightly different. The difference is the population distribution. Instead of using Maxwell distribution $e^{-E_c/k_B T_e}$, the distribution for below-threshold resonance is $e^{-E_c/k_B T_e} f_{T_e,D}(E_c)$ where $f_{T_e,D}(E_c)$ is called the deviation of the below threshold distribution from the Saha-Boltzman bound state distribution. Fig. 4.2 shows examples of the deviation of the population distribution for C^{2+}.

5.3.2 Results for C^{3+} and Mg^{8+}

In this subsection, we investigate the effect of the below near threshold resonances on the DR rate coefficient calculation. The dielectronic recombinations of $C^{3+} \rightarrow C^{2+}$ and $Mg^{8+} \rightarrow Mg^{7+}$ are two selected interesting examples to discuss here. For convenience, we refer the DR rate coefficient including both the above threshold and below near threshold resonances in the calculation as the total DR as opposed to the 'above threshold DR calculation'. One significance of including below near threshold resonances in the DR calculation is that it can eliminate the sensitivity of DR to energy positions. So different calculations performed for this subsection include above threshold DR with/without threshold shift or elimination of above near threshold resonances, total DR with/without threshold shift. A comparison of the different calculations allows us to look for this sensitivity.

The recombinations of $C^{3+} \rightarrow C^{2+}$ and $Mg^{8+} \rightarrow Mg^{7+}$ are two typical interesting cases, because both of them have near threshold resonances, while at the same time they have different significant differences. The former one has a short range of near threshold energies and the resonance is below near threshold. For the latter one, the range of near threshold energies is large and has a lot of resonances just below the ionization potential. So including the below threshold resonances would make a large difference for the total DR rate coefficient.

The outer plots in Figs. 5.4 and 5.5 shows the resonance distributions for C^{3+} and Mg^{8+}, respectively. The black and red solid lines overlap except the first four (in the former figure) and first (in the latter figure) resonances because they are eliminated in the calculation of the red line. The black dotted line is the calculation with shifting the threshold to 0.024 (in the former figure) and 0.02 Ryd. (in the latter one) to move the first four and first resonances just below threshold. The inner plot of Figs. of 5.3 and 5.5 are the corresponding above DR rate coefficients for the three different calculations. Both plots show that three above DR rate coefficients merge together at high temperatures, and split at low temperatures. As the temperature becomes lower, the split is larger. In the inner plot of Fig. 5.3, the red solid line deviates from the other two lines at about 5.7 eV. In the inner plot of Fig. 5.5, the
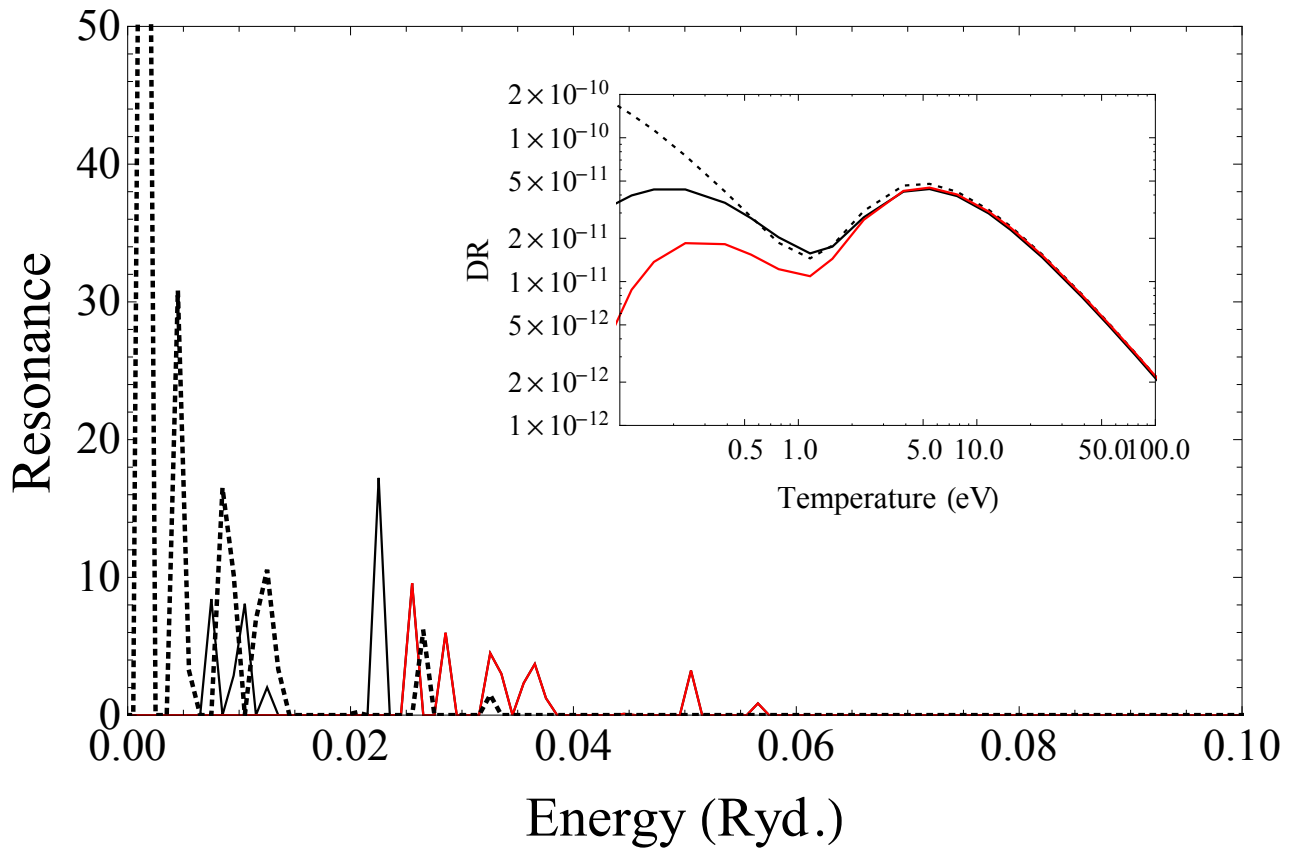
Figure 5.3: Resonance distribution (outer figure)and DR rate coefficient (inner figure) of C^{3+}. The DR rate coefficients shown in this figure are the calculation without below threshold resonance contribution. Black solid line is for the calculation without shift, red solid line is for the calculation eliminating the first four resonances above threshold and black dotted line is for the calculation of shifting the energy position 0.024 Ryd. to threshold.
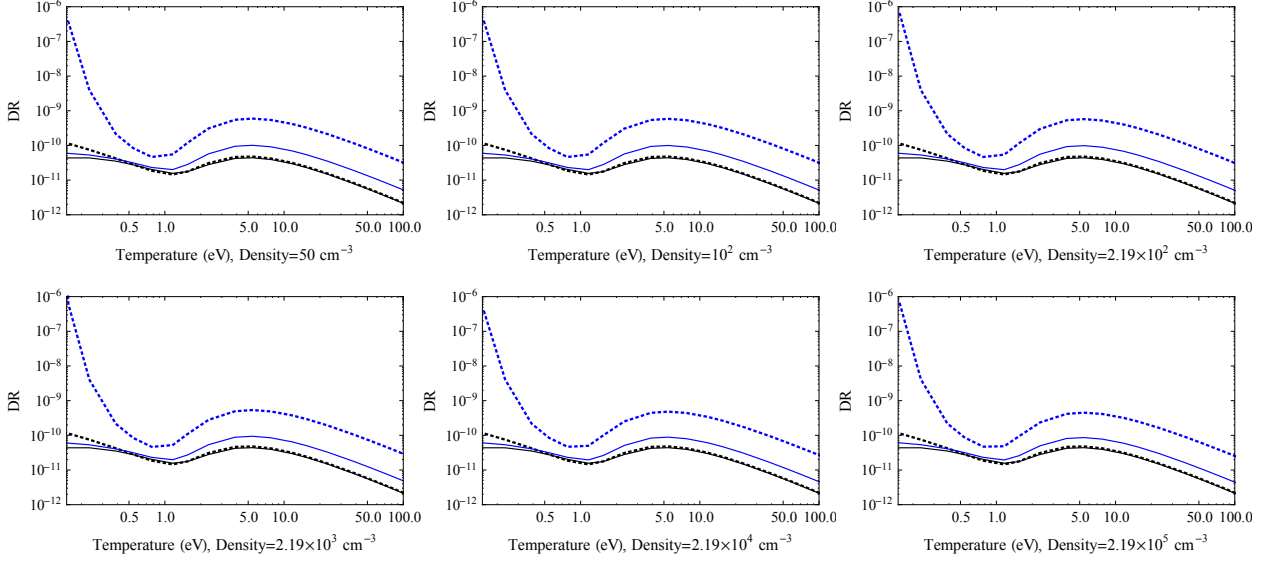
Figure 5.4: DR rate coefficients of different densities for C^{3+}. Black lines are for calculations only including the contribution of above threshold resonance, blue lines are for calculations including both above and below threshold resonances. Solid lines are for calculations without any shift and dotted lines are for calculations of shifting the position 0.024 Ryd. to threshold.

split point of red and black solid lines is at 17.5 eV and 9.2 eV of the red solid and black dotted lines. The differences between the black and red lines in two plots are due to the contribution of the first four and first resonances to above DR. The percentage differences errors are up to 57% and 84% in the two plots respectively. The resonance positions cause the difference between the red solid and black dotted lines in both plots and the percentage differences are up to 67% and 196% respectively. Thus we have two expected conclusions. The above DR is sensitive to energy position as the temperature becomes lower. The near threshold resonances are important at low temperatures. This big percent error between the red solid and black dotted lines is larger than expected. We expect to see a sensitivity to the energy position from the missing near threshold resonances in the DR calculation. However, these two calculations have the same number of resonances in their calculations but different resonances positions. This case is interesting because resonances can move from above to below threshold but other resonances can move out of the sensitive regime. So a third conclusion can be drawn that the effect on above threshold DR from resonance energy

95
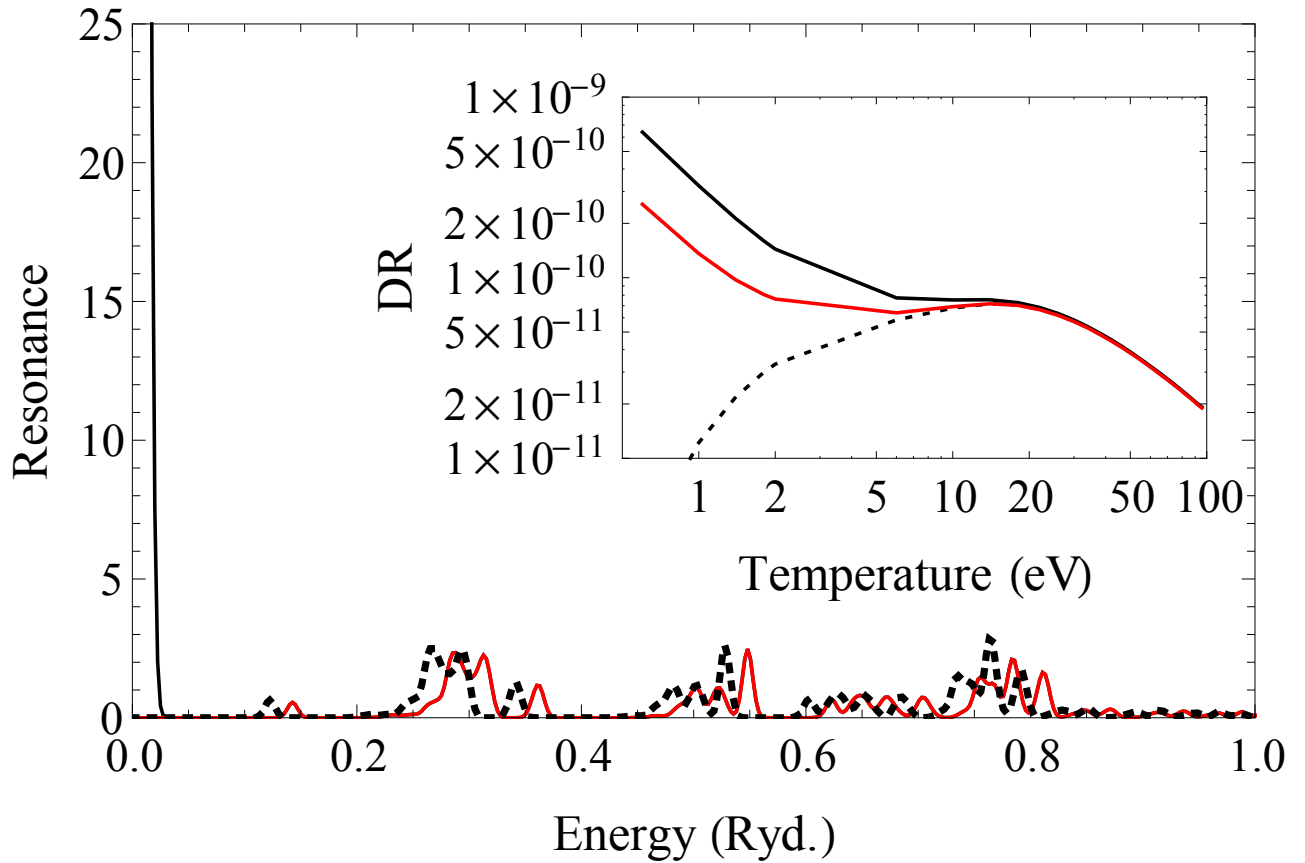
Figure 5.5: Resonance distribution (outer figure)and DR rate coefficient (inner figure) of Mg^{8+}. The DR rate coefficients shown in this figure are the calculation without below threshold resonance contribution. Black solid line is for the calculation without shift, red solid line is for the calculation of eliminating the first resonance above threshold and black dotted line is for the calculation of shifting the energy position 0.02 Ryd. to threshold.
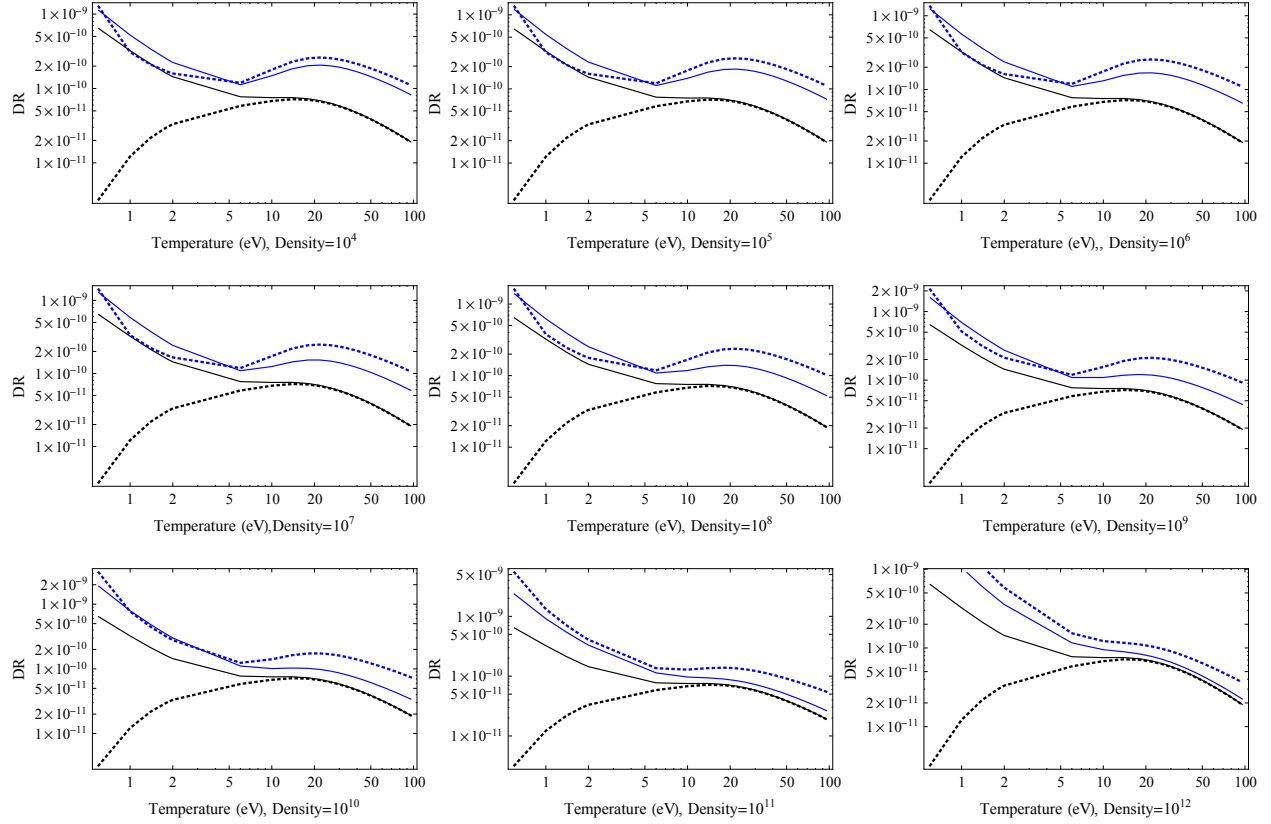
Figure 5.6: DR rate coefficients of different densities for Mg^{8+}. Black line is for the calculation only including the contribution of above threshold resonance, blue line is for the calculation including both above and below threshold resonance. Solid line is for the calculation without any shift and dotted line is for the calculation of shifting the position 0.02 Ryd. to threshold.

position changes can be larger than missing a near threshold resonance. Thus, the size of the sensitivity to missing resonances and resonance positions will depend on the specific case being studied.

Figure 5.6 shows the above DR (black lines) and total DR (blue lines) for different electron densities for Mg^{8+}. The solid lines are for the calculation without any shift and the dotted lines are for the calculation by shifting the threshold by 0.02 Ryd.. The above threshold DR is a function of temperature, but the total DR is also a function of density because the below threshold population distribution is also density dependent. Comparing both total DR lines for each density, the difference is smaller than that between both above threshold DR rate coefficients. This behavior partially supports our previous expectation

97

that including below threshold resonance contributions in the DR rate coefficient calculation can eliminate the sensitivity to the energy position (ie. the differences between the black solid and dotted lines is much larger that the blue solid and dotted lines). More concisely, the conclusion should be that including below threshold resonances contribution in the DR rate coefficient calculation can reduce the sensitivity of the rate coefficient to the resonance energy positions.

5.4 Proposed experimental verification

There is as yet no experimental evidence that verifies the contribution of the below threshold resonances to DR, due to the difficulty in measuring this in beam experiments. We propose an indirect method to prove this effect. After the new DR rate coefficients are calculated, we can use the new data in modeling fractional abundances.These can thus be compared with the results from relative fractional abundances in a plasma environment. Oxygen is a good candidate for this test, because only $O^{4+} \rightarrow O^{3+}$ has near threshold resonances and the effect could be isolated. An experiment with plasma conditions such that below threshold DR was significant could be used to test the predicted abundances of O^{4+} and O^{3+}, to see if the modified rate coefficients can be verified.

5.5 Conclusions

In this paper, we identified ions of Li-like and Be-like iso-electronic sequences with near-threshold resonances using the AUTOSTRUCTURE code and NIST energies. The identification results are presented in Table 5.1 and 5.2. We selected two problematic cases: $C^{3+} \rightarrow C^{2+}$, and $Mg^{8+} \rightarrow Mg^{7+}$ as examples to recalculated their DR rate coefficients including below-threshold resonances using a modified AUTOSTRUCTURE code. Other ions should also have their DR rate coefficients updated and the effects on plasma modeling investigated.

Chapter 6

FINE-STRUCTURE ELECTRON-IMPACT EXCITATION FOR NE$^+$ AND NE^{2+} FOR LOW TEMPERATURE ASTROPHYSICAL PLASMAS

6.1 Background

Electron-impact fine-structure excitation of low charged ions is an important cooling mechanism in most interstellar environments, especially in regions with significant ionization fraction where electron-impact excitation is a strong populating mechanism for the excited states. The lines from these fine-structure transitions can be observed from the infrared (IR) to the submillimeter (submm) by a range of telescopes (e.g., the *Spitzer Space Telescope*, the Stratospheric Observatory for Infrared Astronomy (SOFIA), the *Herschel Space Observatory*, the Atacama Large Millimeter Array (ALMA), etc.). Further, fine-structure excitation due to electron-impact is an important diagnostic tool for the density, pressure, temperature, and/or ambient radiation field, if sufficiently accurate rate coefficients can be obtained. Electron impact fine-structure excitation has been studied fairly extensively for many ions over the past few decades [91–105]. However, almost all of these studies have primarily focused on high energies/high temperatures relevant to collisionally-ionized plasmas and some of the existing fine-structure excitation rate coefficients in current astrophysical codes are still based on a simple model developed by Bahcall & Wolf [106], which may lead to inaccurate results.

For the plasmas of importance in this paper, we require rate coefficients down to approximately 10 K, appreciating that achieving the accuracy in the underlying cross section at this temperature is difficult. Therefore it is important for astrophysical models that collisional calculations are performed down to lower energies and that the associated rate coefficients are updated.

The fine-structure line emissions, Ne II and Ne III, due to electron impact excitation of Ne^+ and Ne^{2+}, respectively, are observed in the IR and known to be very important for probing H II regions. Previous work [18, 107] has proposed that Ne II and Ne III fine-structure lines are appropriate to serve as diagnostics of the source of an evaporative flow, as well as of signatures of X-ray irradiation, so-called X-ray dominated regions (XDRs). This is because hard X-rays have sufficient energy to generate multiple ionization states of neon which can then be collisionally excited. The rate coefficients used in most applications are based on the approximations of Bahcall & Wolf [106]. However, R-matrix methods have been available for these and neighbouring ion stages of Ne. Specifically, collision strengths for the $1s^2 2s^2 2p^5$ ($^2P^0_{3/2}$) - ($^2P^0_{1/2}$) transition of Ne^+ have been calculated using a R-matrix method via the jj omega (JAJOM) approach [93, 94]. The collision strengths of the transitions among levels of the lowest configurations for Ne^{2+} were evaluated by Pradhan [91] and Butler & Mendoza [92], also with an R-matrix method. McLaughlin et al. [108, 109] extended this approach to a large configuration-interaction representation of the target, supplemented by a few extra pseudo-orbitals to improve the target description further. Here, we have re-investigated these two Ne ions for several reasons.

Previous work has focused primarily on higher electron-impact energies than considered here with only a few of their Maxwellian averaged effective collision strengths going below 800 K. This leads naturally to the second focus of the paper, which is the exploration of uncertainty in the rate coefficients at very low temperatures. To this end, three different theoretical level-resolved R-matrix approaches have been applied: the Intermediate Coupling Frame Transformation (ICFT) approach [110], the Breit-Pauli (BP) approximation [111], and the fully relativistic Dirac method [112, 113]. Obstensively, if the underlying electronic structure adopted in each approach was exactly the same there would be little expectation of differences in the collision strengths. However, with the use of different atomic structure codes and the choices made in their use, this invariably leads to small differences in A-values and subsequently, dynamical quantities such as collision strengths.
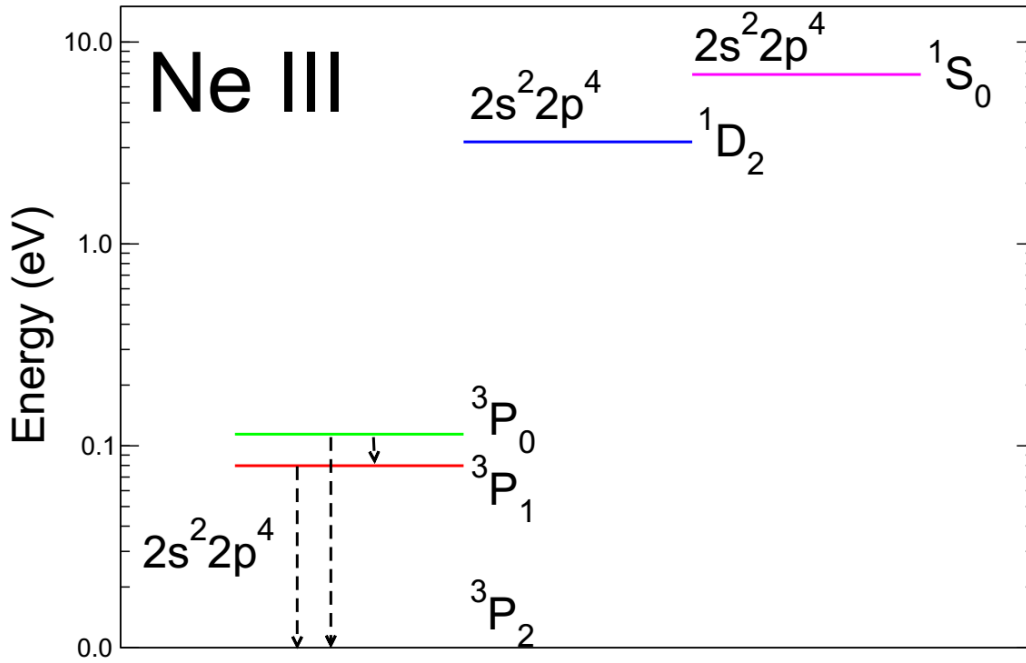
Figure 6.1: Energy diagram for Ne^{2+}. Three transitions are shown: $2s^2 2p^4$ ($^3P_1$) - ($^3P_2$), $2s^2 2p^4$ ($^3P_0$) - ($^3P_1$), and $2s^2 2p^4$ ($^3P_0$) - ($^3P_2$).

Thus, we are interested in the sensitivity of the effective collision strengths to the threshold energy position, the target wave-functions, resonance positions, and anything that can affect the background cross section. We appreciate that the height and position of a single resonance can dramatically affect the results at these temperatures. We shall explore the variation in results to threshold energy and resonance positions by calculating collision strengths where the target energies have been shifted (or not) to NIST energies [14]. Furthermore, we explore the sensitivity of the target wave-function via different target expansions within the BP R-matrix, ICFT R-matrix, and DARC R-matrix methods. After investigating the differences between all calculated effective collision strengths for the same transition, we recommend one based upon our findings.

We focus on excitation at low temperatures in this paper. So for Ne^+, only rates for the transition between the two lowest levels $1s^2 2s^2 2p^5$ ($^2P^0_{3/2}$) - ($^2P^0_{1/2}$) are presented. Also,

the transitions between the three lowest fine-structure levels of Ne^{2+} (see energy diagram in Figure 6.1) are investigated here.

The rest of this chapter is organized as follows. In Sec. **6.2**, we describe the three theoretical methods used in this paper. The calculated results, target energies, Einstein A coefficients, collision strengths, effective collision strengths and excitation rate coefficients for Ne^+ and Ne^{2+} will be discussed in Sec.**6.3**. Sec.**6.4** provides a summary of the results.

6.2   Theory

Level-resolved electron-impact excitation calculations using R-matrix theory, employs a similar formalism whether semi-relativistic or relativistic implementations are used. Ne^+ and Ne^{2+} are not highly charged, therefore both semi-relativistic and fully relativistic methods are equally applicable. The main differences arise from the choices made in the determination of the target orbitals. The atomic structure code AUTOSTRUCTURE [16, 17] generates non-relativistic orbitals whereas the General Relativistic Atomic Structure Package [112, 113] formulates and diagonalises a Dirac-Coulomb Hamiltonian to produce the relativistic orbitals. The former is used in the BP/ICFT [111] collisional calculations and the latter in the Dirac Atomic R-matrix Code (DARC) [112, 114] calculations.

The BP R-matrix method is a set of parallel codes developed from modified serial versions of the RMATRX I codes [111]. Both the BP and ICFT models recouple underlying LS coupling calculations, the former transforms several LS-resolved Hamiltonians into a jK-coupled Hamiltonian, pre-diagonalisation, as opposed to the ICFT approach that transforms unphysical LS-resolved K-matrices into level-resolved collision strengths. In general there has been very good agreement between the ICFT and BP R-matrix methods [99, 110].

The implementations of various flavours of R-matrix theory are used in this study. The review book of Burke [19] provides an excellent overview of non-relativistic (LS coupling), semi-relativistic (BP/ICFT) and relativistic (DARC) electron-impact excitation. The comparison of BP and ICFT results benefits from the use of a completely consistent atomic

Ne$^+$ DARC/BP $n=2$	Ne$^+$ DARC/BP $n=3$	Ne^{2+} DARC/BP $n=2$	Ne^{2+} DARC/BP $n=3$
1s^{2}2s^{2}2p^5	1s^{2}2s^{2}2p^5	1s^{2}2s^{2}2p^4	1s^{2}2s^{2}2p^4
1s^{2}2s2p^6	1s^{2}2s2p^6	1s^{2}2p^6	1s^{2}2p^6
	1s^{2}2s2p^{5}3l	1s^{2}2s2p^5	1s^{2}2s2p^5
	1s^{2}2s^{2}2p^{4}3l		1s^{2}2s2p^{4}3l
			1s^{2}2s^{2}2p^{3}3l
			1s^{2}2p^{5}3l

Table 6.1: Target expansions for Ne$^+$ and Ne^{2+}.

structure as opposed to multiconfiguration Dirac-Fock (MCDF) results from GRASP, though in all cases every effort has been made to optimize the orbitals on the fine-structure levels of the ground term. The DARC calculation employs relativistic orbitals from the initial atomic structure calculations throughout the remainder of the computation. It should be restated that low temperature astrophysical constraints on both our Ne systems means we are pursuing only transitions between the fine-structure levels of the ground term, and that any excited states are included for the main purpose of improving the energy levels of those low-lying states through configuration interaction. Given that the energy separation between the ground state $n=2$ and the excited $n=3$ levels for either Ne$^+$ or Ne^{2+} exceeds 2 Ryd., it is unlikely that Rydberg states attached to the $n=3$ levels would perturb our $n=2$ results.

6.3 Calculation details

6.3.1 Target state calculation

Given the low temperature focus of this paper, only small scale calculations are required for the fine-structure transitions within the ground term. Furthermore, we would like to explore the variation of our results in relation to various configuration-interaction (CI) expansions. Thus, we consider both a small and larger CI expansion for Ne$^+$ and Ne^{2+}, with the configurations described in Table 6.1. The models are referred to as BP $n=2$, DARC $n=2$, BP $n=3$, and DARC $n=3$.

For the ICFT R-matrix method, we only perform calculations for one target expansion, and the included configurations are the same as BP/DARC $n = 3$. This will be used to explore the difference between the BP and ICFT methods.

We also performed optimized BP and ICFT calculations, using orbital scaling parameters to improve the target structure. We use the Thomas-Fermi-Dirac-Amaldi potential, with appropriate scaling parameters. The orbital scaling parameters are λ_{1s}=1.0, λ_{2s}=1.3, λ_{2p}=1.09, λ_{3s}=1.13, λ_{3p}=1.15, λ_{3d}=1.11 for Ne^{2+}, taken from McLaughlin et al. [102]. We refer to these calculations as BP(op) $n = 2/n = 3$ and ICFT(op) $n = 3$ in the following sections.

6.3.2 Scattering calculation

Here we only present details specific to the current R-matrix calculations. The radius of the R-matrix sphere used for Ne$^+$ is 5.40 a.u. for DARC $n = 2$, 19.83 a.u. for DARC $n = 3$, 5.87 a.u. for BP $n = 2$, and 21.60 a.u. for BP $n = 3$. For the ion Ne^{2+}, the radius of the R-matrix sphere is 4.89 a.u. for DARC $n = 2$, 13.28 a.u. for DARC $n = 3$, 5.24 a.u. for BP $n = 2$, 14.35 a.u. for BP $n = 3$, 4.91 a.u. for BP(op) $n = 2$, 14.22 a.u. for BP (op) $n = 3$, and 14.22 a.u. for ICFT(op) $n = 3$. 20 continuum basis orbitals for each angular momentum are chosen for BP/BP(op)/DARC $n = 2$ for both Ne$^+$ and Ne^{2+}, which is more than sufficient to converge the results for the low temperature calculations. All of our models include partial waves from $J = 0$ to 10, which is more than sufficient to converge the cross sections for the energy region for our calculations. An energy mesh of 2.5×10^{-6} Rydbergs for Ne$^+$ and 3.125×10^{-6} Rydbergs for Ne^{2+} ensured resonances were resolved, particularly for the lowest temperatures of subsequent effective collision strengths. We calculate collision strengths up to 0.107 Ryd. for Ne$^+$ and 0.1658 Ryd. for Ne^{2+}, and effective collision strengths from 10-2000 K for both ions. All these parameters are listed in Table 6.2

	Ne$^+$ $n = 2$ DARC, BP	Ne$^+$ $n = 3$ DARC, BP	Ne^{2+} $n = 2$ DARC, BP	Ne^{2+} $n = 3$ DARC, BP
Radius of R-matrix sphere (a.u.)	5.40, 5.87	19.83, 21.60	4.89, 5.24	13.28, 14.35
Continuum basis orbitals for each angular momentum	20	20	20	20
Partial waves J	$0 - 20$	$0 - 20$	$0 - 20$	$0 - 20$
Energy mesh (Ryd.)	2.5×10^{-6}	2.5×10^{-6}	3.125×10^{-6}	3.125×10^{-6}
Energy range (Ryd.)	$0.007 - 0.107$	$0.007 - 0.107$	$0.0058 - 0.1658$	$0.0058 - 0.1658$
Temperature range (K)	$10 - 2000$	$10 - 2000$	$10 - 2000$	$10 - 2000$

Table 6.2: Scattering calculation parameters for different target expansions.

6.3.3 Effective collision strength calculation

The effective collision strength [115, 116] can be calculated from the collision strengths via:

$$\Upsilon_{ij} = \int_0^\infty \Omega_{ij} \exp\left(\frac{-\epsilon_j}{kT_e}\right) d\left(\frac{\epsilon_j}{kT_e}\right), \tag{6.1}$$

where Ω_{ij} is the collision strength for the transition from level i to j, ϵ_j is the energy of the scattered electron, T_e the electron temperature, and k Boltzmann's constant.

The Maxwellian excitation rate coefficient q_{ij} is the coefficient used widely in astrophysics. The relationship between q_{ij} and Υ_{ij} is

$$q_{ij} = 2\sqrt{\pi}\alpha c a_0^2 \left(\frac{I_\mathrm{H}}{kT_e}\right)^{1/2} \frac{1}{\omega_i} e^{-\frac{\Delta E_{ij}}{kT_e}} \Upsilon_{ij}, \tag{6.2}$$

where α is the fine-structure constant, c the speed of light, a_0 the Bohr radius, I_H the hydrogen ionization potential, ΔE_{ij} the energy difference in the fine-structure levels, and ω_i the degeneracy in the lower level. Compared with $q_{ij}(T_e)$, $\Upsilon_{ij}(T_e)$ is a smoother function and can be more accurately interpolated.

6.4 Results and discussion

Astrophysical plasma modellers who study IR/submm observations of low temperature plasmas, such as the interstellar medium, require atomic rate coefficients down to temperatures as low as 10 K. This will place very stringent tests on the accuracy of the atomic

structure and collisional calculations. The excitation rate coefficients will be very sensitive to small changes in the atomic structure. As a result, the structure will impact the rate coefficients through changes in the threshold energy, resonance strengths and positions, and changes in the background cross section. For this reason, we have performed a range of calculations using different methods (BP $n = 2$, DARC $n = 2$, BP $n = 3$, DARC $n = 3$, BP(op) $n = 3$). These will be used to explore the variation of the effective collision strengths, particularly at low temperatures. The purpose of including the $n = 3$ configurations is to improve the energies and transition probabilities for the levels within the ground term.

6.4.1 Bound-state energies and radiative rates for Ne^+ and Ne^{2+}

Our recommended dataset shall be the model that minimizes the difference between that calculation and the NIST A-values and level energies (Kramida et al. 2015). The results are shown in Tables 6.3 and 6.4. The percent error ($\delta\%$) shown is calculated by $\frac{x-x_{NIST}}{x_{NIST}} \times 100\%$ with the NIST data providing the accepted values.

The BP/DARC $n = 2$ and $n = 3$ target expansions give rise to 3 and 108 levels for Ne^+, and 10 and 226 levels for Ne^{2+}. The energies for the levels within the ground term are presented in Table 6.3 and the associated A-values in Table 6.4. In general, the percent errors show that the agreement between theoretical and NIST values is reasonable. The $n = 3$ target expansion results in marginally better energies for both ions and different R-matrix methods compared to the $n = 2$ expansion. For Ne^+, the average percentage error for the BP $n = 2$, BP $n = 3$, DARC $n = 2$, and DARC $n = 3$ target expansions are 1.41%, 0.96%, 3.6% and 0.42%, respectively. While for Ne^{2+}, the corresponding average percent errors for target energies are 8.13%, 6.95%, 3.72% and 3.33%.

Optimized BP calculations are also performed for Ne^{2+}, giving average percentage errors of 3.34% for BP(op) $n = 2$ and 3.20% for BP(op) $n = 3$. The DARC R-matrix method produces better energies than the BP R-matrix method for Ne^{2+} for both $n = 2$ and $n = 3$. The optimized BP calculation for Ne^{2+} dramatically increases the accuracy of the energies.

Config.	Term $(^{2s+1}L_J)$	NIST	BP $n=2$	$\delta\%$	BP $n=3$	$\delta\%$	DARC $n=2$	$\delta\%$	DARC $n=3$	$\delta\%$
$2s^22p^5$	$^2P^0_{3/2}$	0.0000	0.0000	0	0.0000	0	0.0000	0	0.0000	0
	$^2P^0_{1/2}$	0.0071	0.0069	2.82	0.0070	1.91	0.0076	7.2	0.0071	0.84
Avg. $\delta\%$				1.41		0.96		3.6		0.42
$2s^22p^4$	$^3P_2$	0.0000	0.0000	0	0.0000	0	0.0000	0	0.0000	0
	$^3P_1$	0.0059	0.0049	15.75	0.0051	13.01	0.0060	1.59	0.0057	3.11
	$^3P_0$	0.0084	0.0073	13.29	0.0075	10.47	0.0088	4.33	0.0084	0.32
	$^1D_2$	0.2355	0.2348	0.27	0.2454	4.23	0.2521	7.05	0.2664	13.15
	$^1S_0$	0.5081	0.4504	11.36	0.4722	7.06	0.4795	5.62	0.5083	0.05
Avg. $\delta\%$				8.13		6.95		3.72		3.33
			BP(op) $n=2$		BP(op) $n=3$					
$2s^22p^4$	$^3P_2$	0.0000	0.0000	0.00	0.0000	0.00				
	$^3P_1$	0.0059	0.0058	1.47	0.0057	2.64				
	$^3P_0$	0.0084	0.0085	1.22	0.0084	0.05				
	$^1D_2$	0.2355	0.2532	7.52	0.2573	9.25				
	$^1S_0$	0.5081	0.4751	6.48	0.4874	4.07				
Avg. $\delta\%$				3.34		3.20				

Table 6.3: Energy comparison of Ne$^+$ and Ne^{2+} (in Ryd). The configurations and terms listed in the first two columns label different levels. The third column gives the corresponding energies from NIST [14]. The percent error after each theoretical energy indicates the deviation of the theoretical value from the NIST one. The last line of each table is the average error of each theoretical calculation.

Ion	Transition	NIST	BP $n=2$	$\delta\%$	BP $n=3$	$\delta\%$	DARC $n=2$	$\delta\%$	DARC $n=3$	$\delta\%$
Ne$^+$	$2p^5$ ($^2P_{3/2}$) - ($^2P_{1/2}$)	8.59e-3	7.84e-3	8.68	8.07e-3	6.1	8.16e-3	5.01	6.22e-3	27.64
Ne^{2+}	$2p^4$ ($^3P_2$) - ($^3P_1$)	5.84e-3	3.57e-3	38.85	3.93e-3	32.7	5.86e-3	0.42	5.11e-3	12.56
	$2p^4$ ($^3P_1$) - ($^3P_0$)	1.10e-3	9.10e-4	17.2	1.00e-3	8.8	1.15e-3	4.95	9.75-4	11.37
			BP(op) $n=2$	$\delta\%$ $\delta\%$	BP(op) $n=3$	$\delta\%)$ $\delta\%)$				
Ne^{2+}	$2p^4$ ($^3P_2$) - ($^3P_1$)	5.84e-3	5.71e-03	2.19	5.51e-03	5.63				
	$2p^4$ ($^3P_1$) - ($^3P_0$)	1.10e-3	1.43e-03	30.2	1.39e-03	25.99				

Table 6.4: Einstein A coefficient (in s^{-1}) comparison for Ne$^+$ and Ne^{2+} with NIST data [14]. Columns as in Table II.

Table 6.4 presents the comparison of Einstein A coefficients for both the Ne^+ and Ne^{2+} transitions. In both cases, the DARC $n = 2$ calculations produce the closest agreement with NIST values. The remainder of the dataset shall be used to gauge the variation between the different calculations. The accuracy of the Einstein A coefficient is not only related to the precision of the target energies, but also depends on the reliability of the target wavefunctions. The optimized BP $n = 3$ calculation does give better target energies and A-values compared with the BP(op) $n = 2$, showing an improvement with CI expansion. This trend is not reflected in the DARC results, see Tables 6.3 and 6.4. We conclude that our recommended dataset is the DARC $n = 2$ calculation which has the most accurate target energies and A-values, and will provide the most accurate collision strengths, effective collision strengths and excitation rate coefficients. We also investigated the differences between an ICFT(op) and the BP(op) calculation for Ne^{2+} using the same structure, noticing no differences in the effective collision strengths.

6.4.2 Collision strengths and effective collision strengths for Ne^+ and Ne^{2+}

To our knowledge, there are no experimental results for the collision strengths for transitions within the ground complex for either of these ion stages. Our goal is to determine the variation in effective collision strengths between our best models as we progress to the very low temperatures required by the astrophysical applications. We have adopted two different approaches to calculating meaningful representative percent differences in our work.

In the first approach we calculate a percentage uncertainty on the effective collision strengths simply using the standard deviation of our three most accurate models as determined from the accuracy of the energy levels and the associated A-values, given by

$$\%\Delta = \frac{\sigma(\bar{x}_{best})}{x_i} \times 100\% \tag{6.3}$$

where $\sigma(\bar{x}_{best})$ is the standard deviation. Secondly, we obtain a percent difference comparing results from our semi-relativistic and fully-relativistic R-matrix methods employing exactly the same set of non-relativistic target configurations. In this case, the percentage difference is calculated by the formula $\frac{x_1-x_2}{(x_1+x_2)/2}\times100\%$.

Figures 6.2 – 6.5 illustrate the collision strengths and effective collision strengths for the fine-structure transitions of both Ne^+ and Ne^{2+}, using the different R-matrix methods. Figures 6.6 – 6.8 explore the effects of shifting the target threshold energies to NIST values.

Sampling a range of calculations allows us to more objectively explore the variation of collision strength in regards to the size of the different CI expansions. As stated earlier, the sizeable energy separation between the $n = 2$ and $n = 3$ levels precludes the possibility of interloping resonances attached to the $n = 3$ levels perturbing the cross sections from transitions amongst the $n = 2$ levels. The influence of resonance contributions to effective collision strengths is only expected for the case of Ne^{2+} due the $2p^4$ subshell supporting 3 levels within the ground state complex, whereas the resonances attached to the upper $J = \frac{1}{2}$ levels of $Ne^+(2p^5)$ lie in the elastic cross section of the Ne^+ ground state.

Figure 6.2 shows collision strengths (top) and effective collision strengths (bottom) for the Ne^+ $2s^22p^5(^2P^0_{3/2})$ - $(^2P^0_{1/2})$ transition. The largest collision strengths come from the BP $n = 2$ calculation, the next lower ones are from the DARC $n = 2$ calculation, then from BP $n = 3$ and DARC $n = 3$. The DARC $n = 2$ calculation is our recommended data set based upon A-value comparisons with the NIST database values. Furthermore, in the absence of experiment, the MCDF approach would be our recommended theoretical model. Subsequent effective collision strengths were generated from the respective collision strengths of each calculation. We note that beyond the current work, a previous large-scale BP R-matrix calculation for Ne^+ has been carried out by Griffin et al. [95]. However, the focus of that work was to provide a large comprehensive data set across a wide range of temperatures, but not at the very low temperatures required by our study. At 1000 and 2000 K, the DARC $n = 2$ effective collision strengths were in best agreement with this previous work. Our
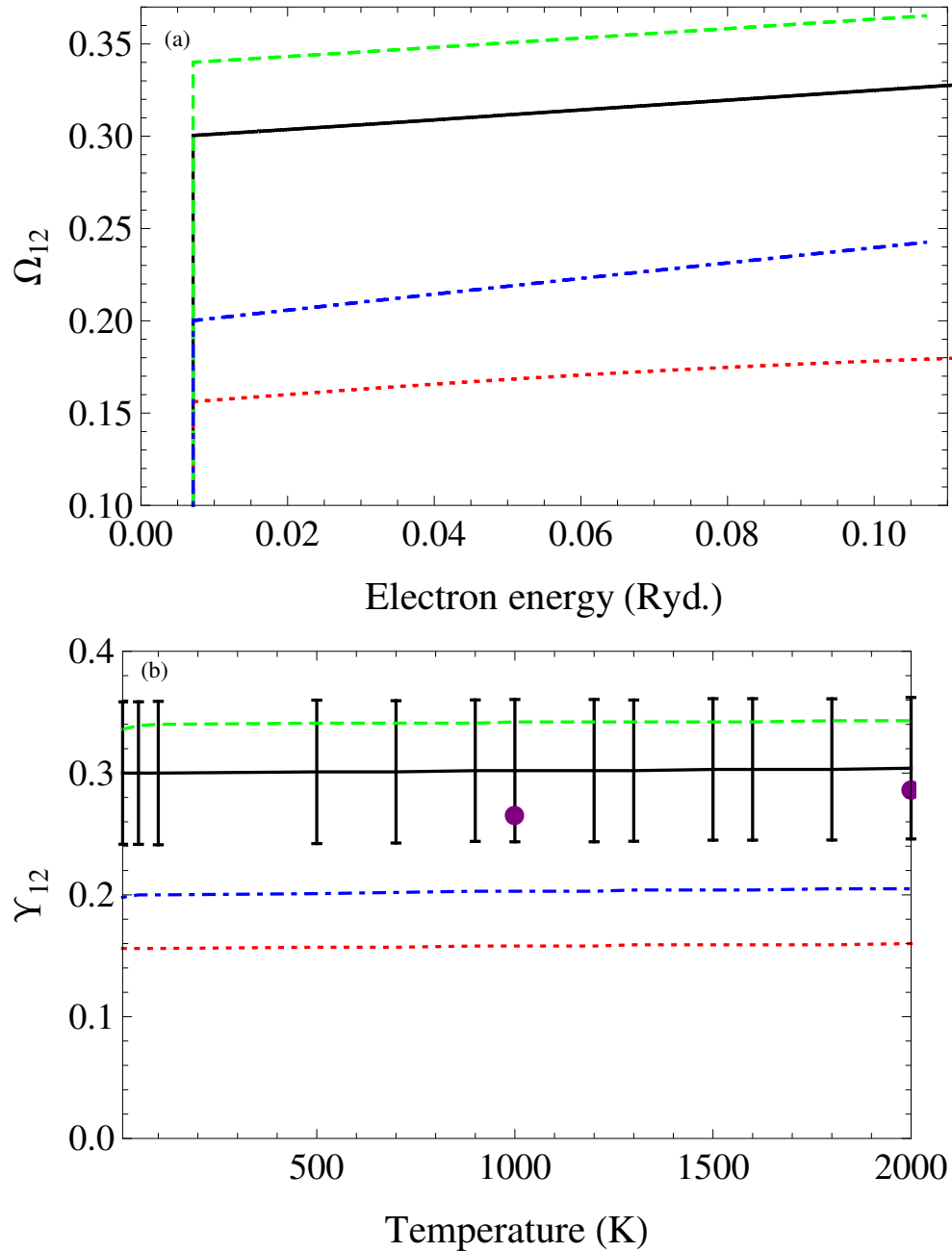
Figure 6.2: Comparison of Ne$^+$ collision strengths (a) and effective collision strengths (b) for the 2s^{2}2p^5 (^{2}P$^0_{3/2}$) - (^{2}P$^0_{1/2}$) transition between different target expansions: DARC $n = 2$ (black solid line), DARC $n = 3$ (red dotted line), BP $n = 2$ (green dashed line), and BP $n = 3$ (blue dot-dashed line). Uncertainty estimates are given for our recommended DARC $n = 2$ results with comparison to the previous R-matrix calculation (purple circles) of Griffin et al. (2001).

effective collision strengths are 0.302 at 1000 K and 0.304 at 2000 K, compared with 0.266 and 0.286 from Griffin et al. [95], as shown in Fig. 6.2, giving differences of 12.7% and 6.1%, respectively. Thus, this supports our independent conclusion that our DARC $n = 2$ effective collision strengths should be the recommended dataset at even lower temperatures, and are tabulated in Table B.1.

Employing the average percentage uncertainty given by Equation (6.3), the $\bar{x}_{best}$ values used to calculate the uncertainty are the BP $n = 2$, BP $n = 3$, and the DARC $n = 2$ results, providing an uncertainty from 19.1-19.6% for our recommended DARC $n = 2$ effective collision strengths, as shown in Figure 6.2.

It is also of interest to consider the differences between the DARC and BP calculations, for the cases when they both have the same configurations. The differences of the effective collision strengths between the DARC $n = 2$ and BP $n = 2$ are 11.3 – 12.1%, while the DARC $n = 3$ and BP $n = 3$ differ by 23.7 – 24.7%, which is consistent with the differences between the A-values from these calculations. We note that, perhaps counterintuitively, the DARC $n = 3$ results drift from the recommended values, however the explanation lies in the fact that the DARC code will endeavour to optimise all orbitals on an equal footing, when in fact we should focus only on the $n = 2$ optimisation at the expense of the $n = 3$ levels.

Figures 6.3 – 6.5 present the collision strengths (top) and effective collision strengths (bottom) for three different transitions of Ne^{2+}, namely, the (^{3}P$_2$) - (^{3}P$_1$) (Fig. 6.3), (^{3}P$_1$) - (^{3}P$_0$) (Fig. 6.4), and (^{3}P$_2$) - (^{3}P$_0$ (Fig. 6.5) transitions. For the collision strengths of the three transitions, the unoptimised BP $n = 2$ result has the largest background, however an optimised structure aligns better with the DARC $n = 2$ result. On the other hand, the previous calculation by McLaughlin et al. (2011), which extended down to 2000 K appears to be consistent with the DARC $n = 3$ result. The difference between our DARC $n=2$ and McLaughlin et al. (2011) are attributed to the fact that that our DARC $n=2$ calculation was focused on generating accurate data only for fine structure transitions within the ground term, while McLaughlin et al. [102] results were focused on higher temperatures and higher
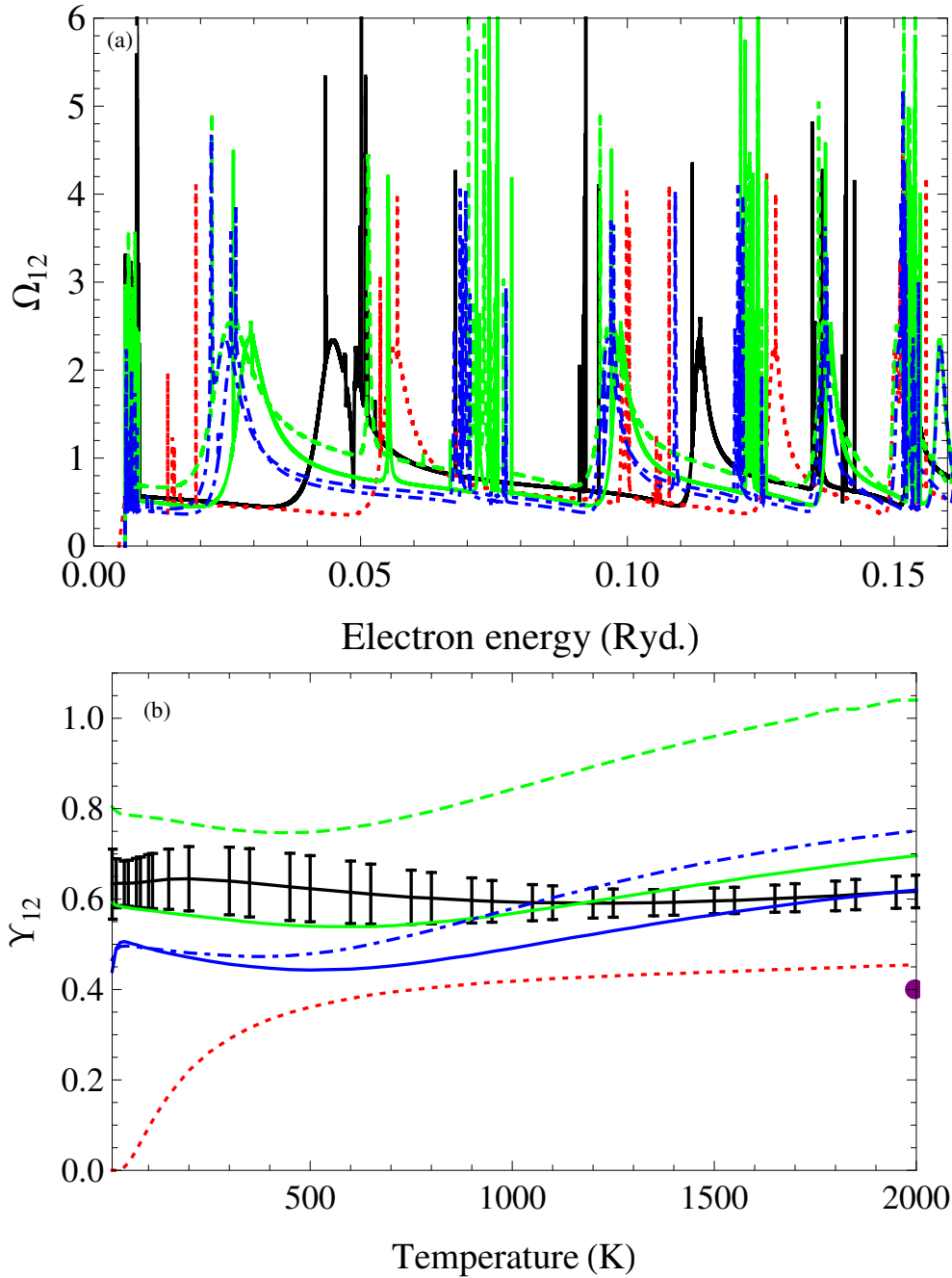
Figure 6.3: Comparison of Ne^{2+} collision strengths (a) and effective collision strengths (b) for the $2s^2 2p^4$ ($^3P_2$) - ($^3P_1$) transition between different target expansions: DARC $n = 2$ (black solid line), DARC $n = 3$ (red dotted line), BP $n = 2$ (green dashed line), BP $n = 3$ (blue dot-dashed line), BP(op) $n = 2$ (green solid line), BP(op) $n = 3$ (blue solid line), and ICFT(op) $n = 3$ (thick black solid). Uncertainty estimates are given for our recommended DARC $n = 2$ results with comparison to the previous R-matrix calculation (purple circle) of McLaughlin et al. [102].
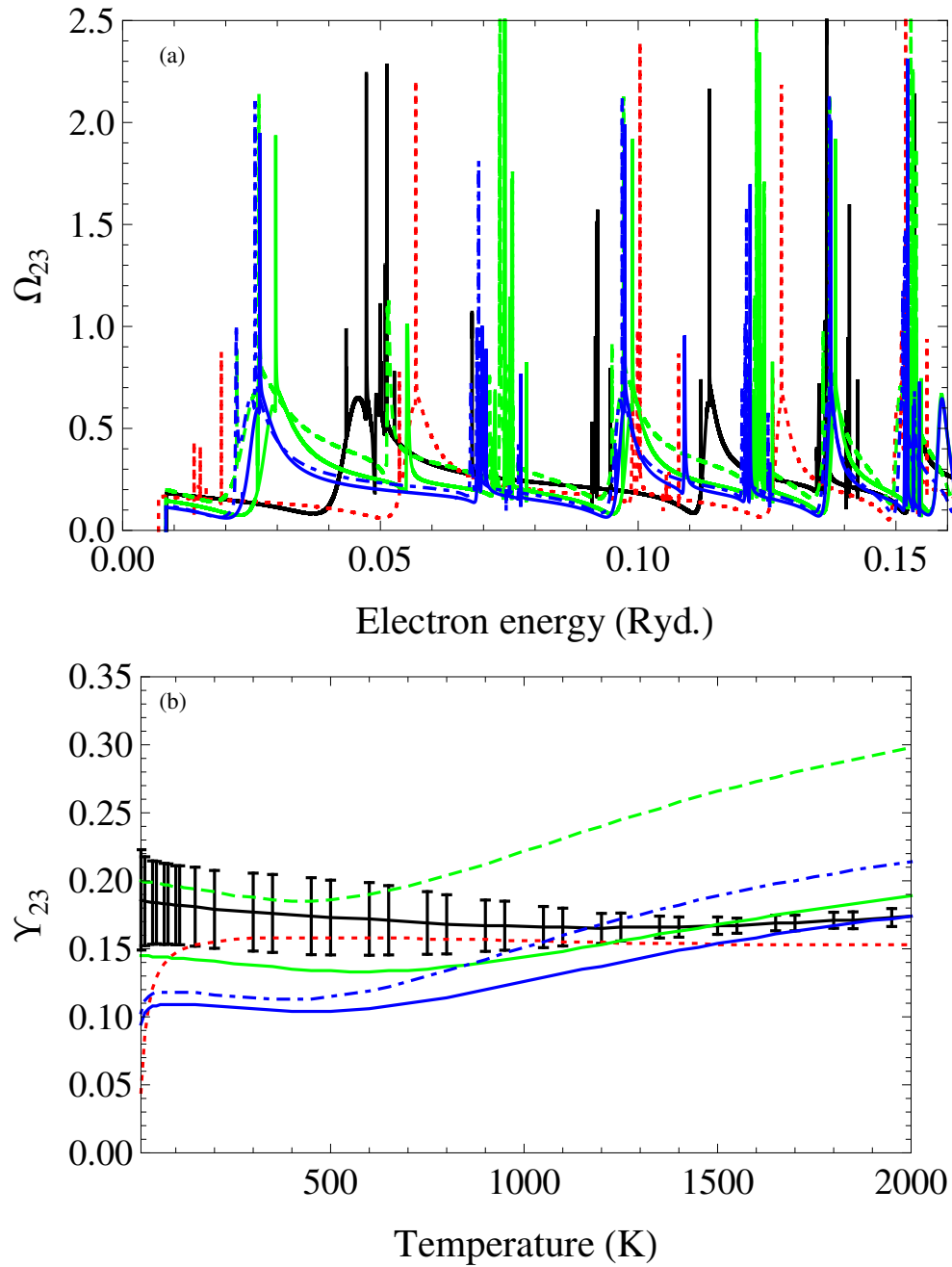
Figure 6.4: Comparison of Ne^{2+} collision strengths (a) and effective collision strengths (b) for the $2s^2 2p^4$ ($^3P_1$) - ($^3P_0$) transition between different target expansions: DARC $n = 2$ (black solid line), DARC $n = 3$ (red dotted line), BP $n = 2$ (green dashed line), BP $n = 3$ (blue dot-dashed line), BP(op) $n = 2$ (green solid line), BP(op) $n = 3$ (blue solid line), and ICFT(op) $n = 3$ (thick black solid). Uncertainty estimates are given for our recommended DARC $n = 2$ results.
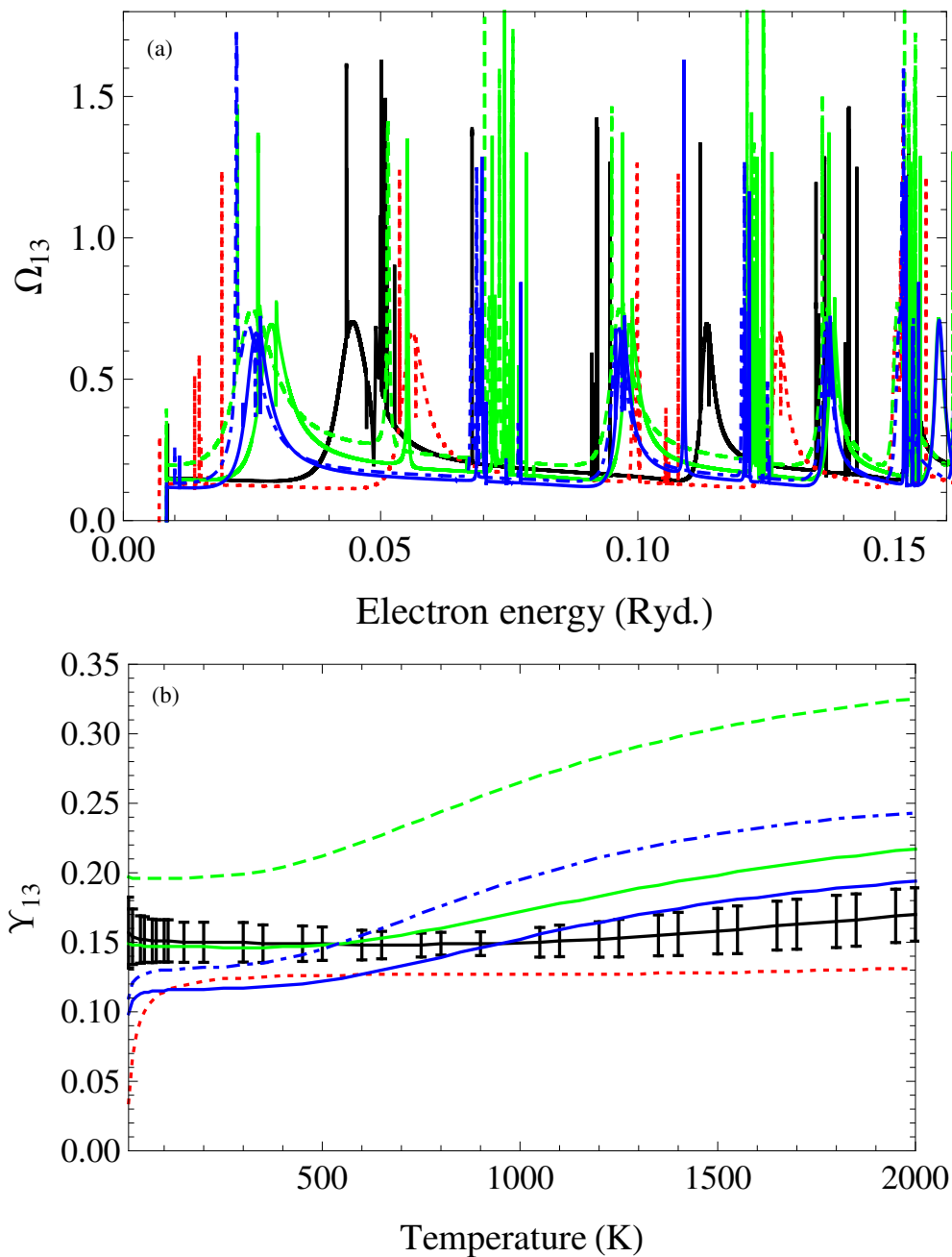
Figure 6.5: Comparison of Ne^{2+} collision strengths (a) and effective collision strengths (b) for the $2s^2 2p^4$ ($^3P_2$) - ($^3P_0$) transition between different target expansions: DARC $n = 2$ (black solid line), DARC $n = 3$ (red dotted line), BP $n = 2$ (green dashed line), BP $n = 3$ (blue dot-dashed line), BP(op) $n = 2$ (green solid line), and BP(op) $n = 3$ (blue solid line). Uncertainty estimates are given for our recommended DARC $n = 2$ results.

n shells in addition to the levels within the ground term. Overall, our recommended collision strength is that produced by the DARC $n = 2$ calculation, based upon energy level and A-value comparisons with NIST data as discussed above.

The uncertainty in the DARC $n = 2$ results are again provided in a similar fashion using Eq. 6.3 and the standard deviation of the other BP and DARC models. Values for $\bar{x}_{best}$ for Ne^{2+} are taken from the DARC $n = 2$, BP(op) $n = 2$, and BP(op) $n = 3$ calculations. It is interesting to note that the collision strengths from the optimised BP $n = 2$ calculation deviate significantly from the unoptimised BP $n = 2$ values.

Considering the effective collision strengths involving the higher excited state transitions (Figs. 6.4 and 6.5), the DARC $n = 2$ model remains our recommended dataset, with uncertainties given by the previously applied method. The uncertainty of the effective collision strengths from the DARC $n = 2$ calculations are $4.7 - 12.2\%$ (Fig. 6.3), $3.2 - 19.8\%$ (Fig. 6.4), and $5.5 - 16.2\%$ (Fig. 6.5).

As we present rate coefficients at very low temperatures (see table in Appendix B.2), we also investigated the sensitivity of the effective collision strengths to changes in the target threshold energy positions. It is expected that due to the Rydberg states having high principal quantum numbers there should be a very strong correlation between the energy shift of the target level and the corresponding energy shift of the resonance attached to it.

This study was performed by comparing a BP calculation with shifts to NIST energies and a BP calculation with no shifts, in each case for Ne^{2+}. See Figs. 6.6 – 6.8 for the results. The difference between the two BP calculations (with/without energy shift) is up to 89.0% for the $({}^3P_2)$ - $({}^3P_1)$ transition, up to 38.7% for the $({}^3P_1)$ - $({}^3P_0)$, and up to 31.8% for the $({}^3P_2)$ -$({}^3P_0)$. The large difference in the first transition is due to the presence of near threshold resonances. Thus, to generate accurate low temperature rate coefficients it is important to shift to accurate, experimental energies, and the cases with near threshold resonances are particularly sensitive.
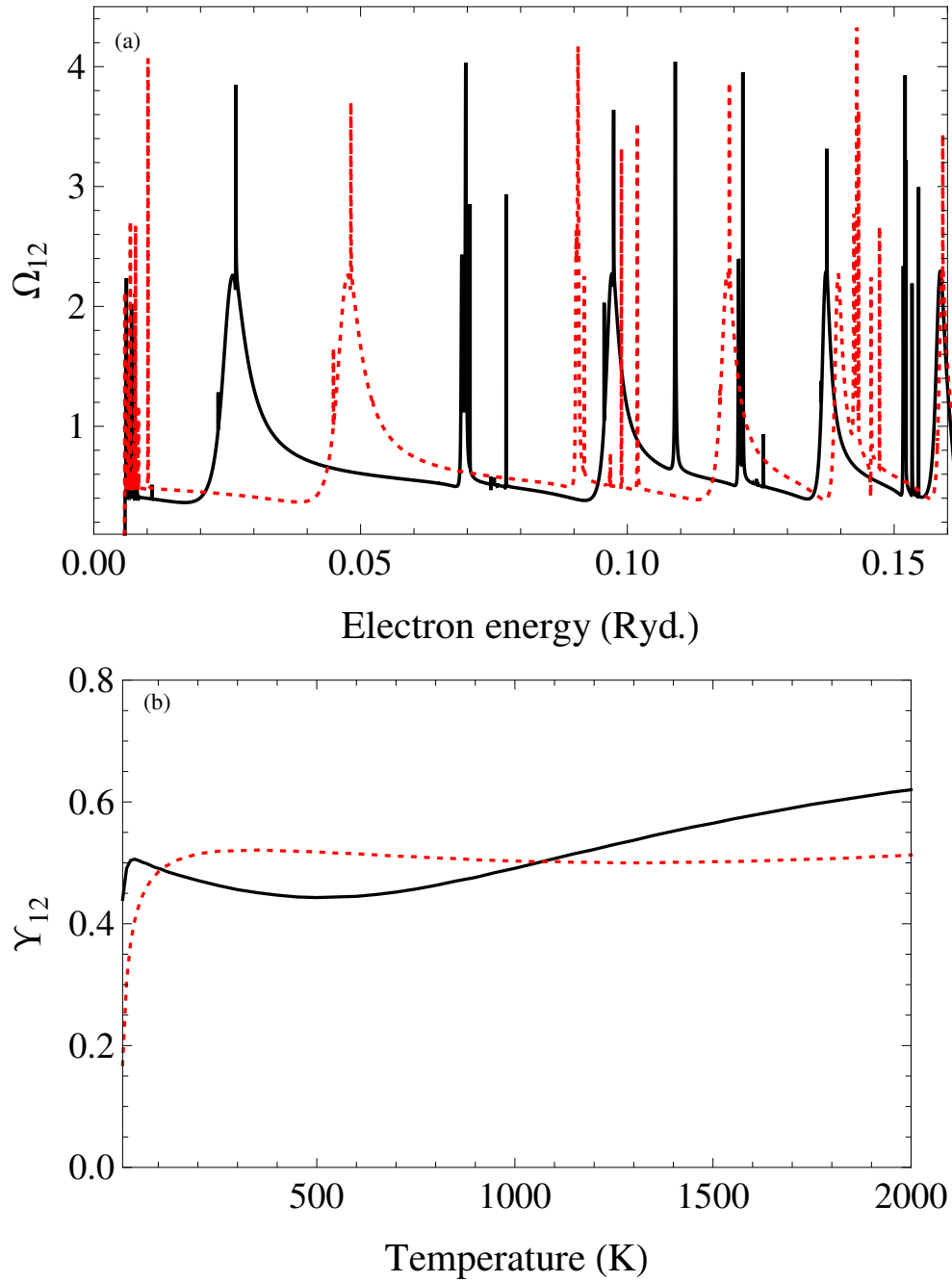
Figure 6.6: Comparison of Ne^{2+} collision strengths (top) and effective collision strengths (bottom) for the 2s^{2}2p^4 (^{3}P$_2$) - (^{3}P$_1$) transition: BP(op) $n = 3$ with (black solid line) and without (red dotted line) the energy shift.
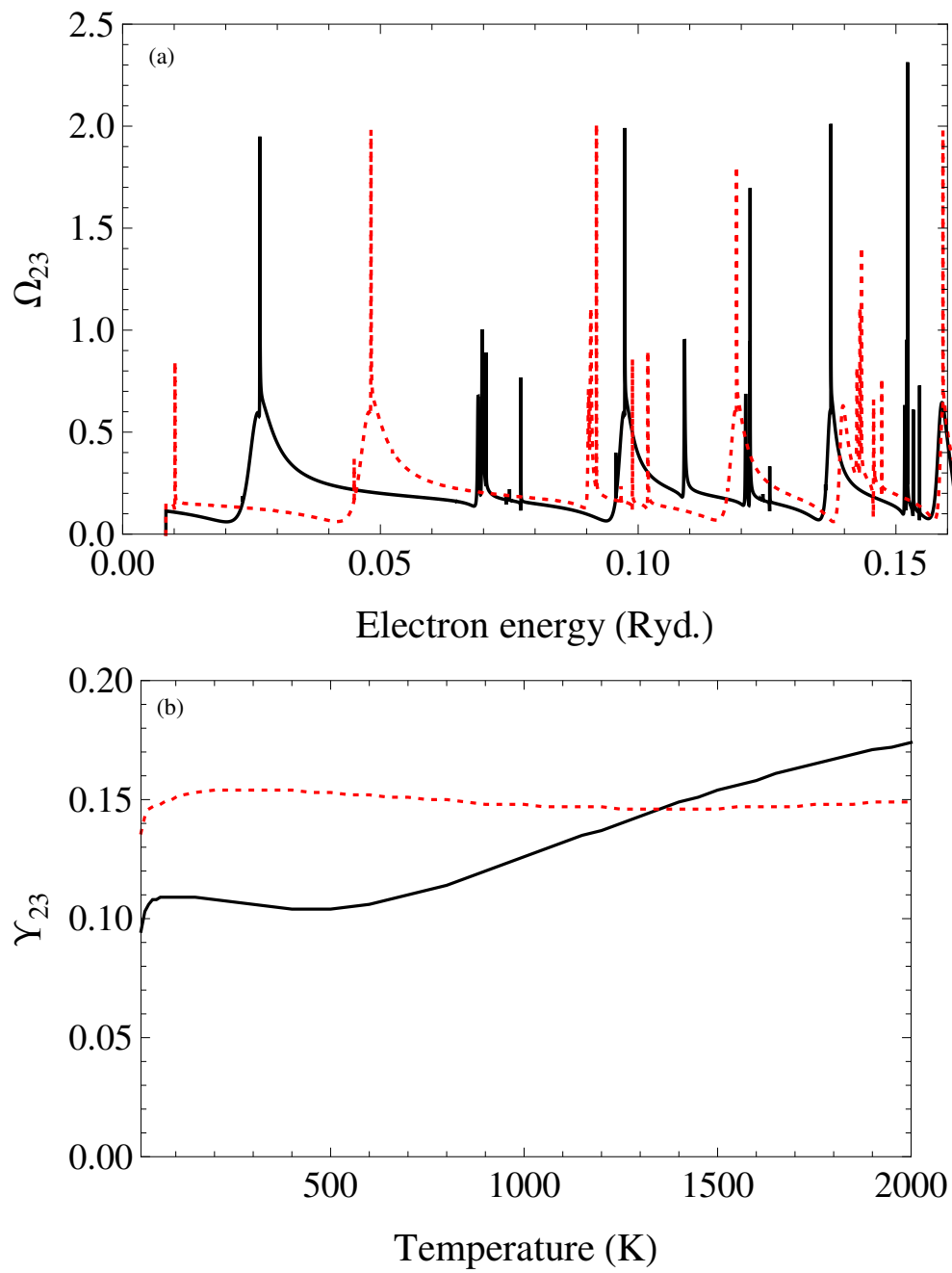
Figure 6.7: Comparison of Ne^{2+} collision strengths (top) and effective collision strengths (bottom) for the 2s^{2}2p^4 (^{3}P$_1$) - (^{3}P$_0$) transition: BP(op) $n = 3$ with (black solid line) and without (red dotted line) the energy shift.
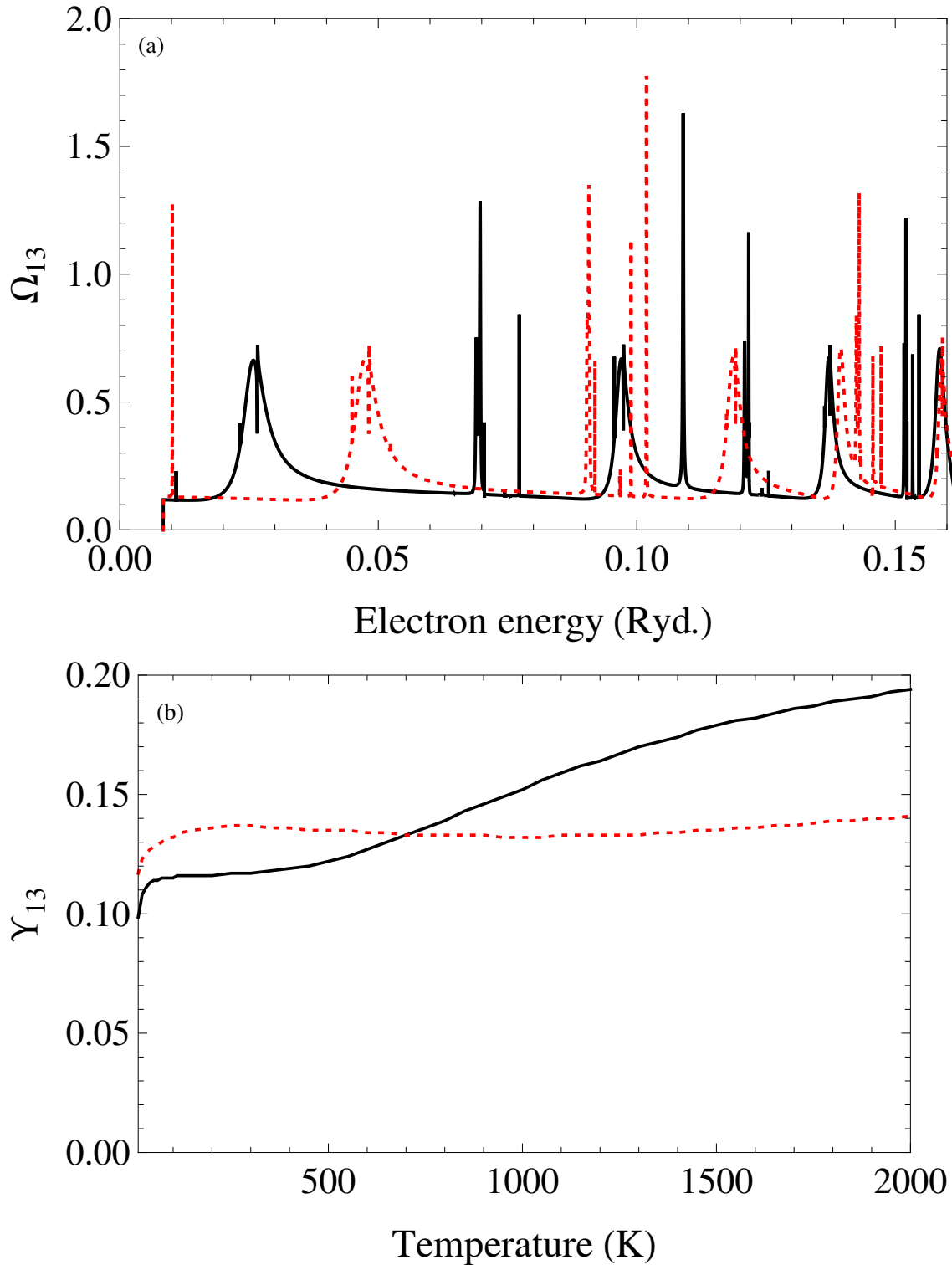
Figure 6.8: Comparison of Ne^{2+} collision strengths (top) and effective collision strengths (bottom) for the 2s^{2}2p^4 (^{3}P$_2$) - (^{3}P$_0$) transition: BP(op) $n = 3$ with (black solid line) and without (red dotted line) the energy shift.

6.5   Conclusions

We calculated the collision strengths and effective collision strengths for Ne^+ and Ne^{2+} with BP, ICFT and DARC R-matrix methods. We are interested in the rates at low temperature $(10 - 2000$ K$)$, so we focus on small energies $(0.007 - 0.107$ Ryd. for Ne^+ and $0.0058 - 0.1658$ Ryd. for $Ne^{2+})$ and perform small scale R-matrix calculations. After comparing the energies, the Einstein A coefficients (A_{ij}), collision strengths (Ω_{ij}), effective collision strengths (Υ_{ij}) and the Maxwellian excitation rate coefficient q_{ij}, we conclude that the DARC $n = 2$ model gives rise to the most reliable collision strengths and effective collision strengths with the Einstein A coefficients generated by this method being closest to the recommended values (i.e., NIST). Further, effective collision strengths computed with the DARC $n = 2$ approach result in rates which agree best with the existing data calculated by large-scale R-matrix methods.

Chapter 7

FUTURE WORK

Three topics are included in this dissertation: inner-shell photo-ionization followed by Auger decay, below threshold resonance contribution to Dielectronic Recombination and electron-impact fine-structure excitation. Each of these topics have future work that would be intersting to pursue.

For the inner shell photo-ionization followed by Auger decay topic, we would like to investigate negative ions. This system can be interesting because of the weaker coulomb potential and emergence of a new short range potential.

For the below threshold DR, we would like to continue with the search for satellite lines evidence of below threshold recombination Abell 30. While the UV spectrum from the IUE instrument did not have enough wavelength resolution to test for the presence of the lines, the STIS instrument on the Hubble Space Telescope would have sufficient resolution and sensitivity. As part of this work a proposal was submitted to request observing time on the Hubble Space Telescope. The idea was to observe the satellite lines of C^{3+} at 1550 A in a knot of Abell 30. While the temperature of this knot is a matter of some debate, it has been measured to be less than 1 eV when carbon lines are used. Appendix D contains the proposal that was submitted, where the reader can find details on the likely photon fluxes detected by the STIS instrument. It is our intention to submit future proposals for time on the STIS instrument. We will also perform additional searches of existing UV spectra of planetary nebulae, to determine if evidence already exists in archived data.

On the same topic, another possible method to verify the existence of below threshold DR contribution is to model the fractional abundances with the new calculated DR rate coefficients and compare with the observed ion stage abundances in low temperature plasmas.

O is an ideal candidate to perform this test because only O^{4+} has near threshold resonance and the DR rate coefficients of other ions of this element have accurate values in the current database. This will be investigated as part of future work. It would also be very beneficial to go through other iso-electronic squences and identify cases with near threshold resonances, correcting their rate coefficients as in chapter 5.

One other interesting thing to explore is the increase in the negative energy distribution function at higher temperatures, see Fig. 4.2. This is caused because dielectronic recombination is a very efficient means of populating the Rydberg states at the higher temperatures, while the loss rates are small. This causes an increase in the DR rate coefficient at higher temperatures. It would be interesting to verify this over population of the Rydberg states.

For the electron-impact fine-structure excitation topic, we would like to calculate the excitation coefficient for other ions, such as Ar^+, Ar^{2+}, and the low charge states of iron. In each case the R-matrix method would be used, and uncertainties assigned to the final excitation rate coefficients. The new fine-structure excitation data (including the work of this dissertation) should be combined with ion-impact excitation data being calculated at the University of Georgia and used in spectral models of ultra low temperature astrophysical plasmas.

Bibliography

[1] Qianxia Wang, S Sheinerman,F. Robicheaux, J. Phys. B **47**, 215003 (2014).

[2] Qianxia Wang, S.D. Loch, Phys. Rev. A **91**, 053416 (2015).

[3] R. Guillemin, S. Sheinerman, C. Bomme, et al., Phys. Rev. Lett. **109**, 013001 (2012).

[4] A.L. Landers, et al., Phys. Rev. Lett **102**, 223001 (2009).

[5] H. Massey and D. Bates, *The properties of neutral and ionized atomic oxygen and their influence on the upper atmosphere*, Rep. Prog. Phys. **9**, 62 (1943)

[6] M. Bitter, K. Hill, L. Roquemore, P. Beiersdorfer, D. Thorn, M.F.Gu, Rev. Sci. Instr. **74** 1977 (2003)

[7] A. Burgess, *Dielectronic recombination and the temperature of the solar corona*, Astrophysical Journal **139** 776 (1964)

[8] N.R. Badnell et al., Astronomy and Astrophysics **406**, 1151 (2003)

[9] M.F. Gu, The Astrophysical Journal **590**, 1131 (2003)

[10] M. Fogle, N.R. Badnell, P. Glans, S.D. Loch, S. Madzunkow, Sh. Abdel-Naby, M.S. Pindzola, R. Schuch, *Electron-ion recombination of Be-like C, N, and O*, Astronomy and Astrophysics **442**, 757 (2005)

[11] S. Shippers, D. Bernhardt, A. Muller, C. Krantz, M. Grieser, R. Repnow, A. Wolf, M. Lestisnsky, M. Hahn, O. Novotny, and D.W. Savin, *Dielectronic recombination of xenonlike tungsten ions*, Phys. Rev. A **83**, 012711 (2011)

[12] F. Robicheaux, S.D. Loch, M.S. Pindzola, and C.P. Ballance, *Contribution of Near Threshold States to Recombination in Plasmas*, Phys. Rev. Letts. **105** 233201 (2010)

[13] Guerrero, M. A., Ruiz, N., Hamann, W.-R., Chu, Y.-H., Todt, H., Schönberner, D., Oskinova, L., Gruendl, R. A., Steffen, M., Blair, W. P., and Toalá, J. A. (2012).

[14] Kramida, A., Ralchenko, Yu., Reader, J., and NIST ASD Team (2015). NIST Atomic Spectra Database (ver. 5.3), [Online]. Available: http://physics.nist.gov/asd. National Institute of Standards and Technology, Gaithersburg, MD.

[15] H.P. Summers, W.J. Dickson, M.G. O'Mullance, N.R. Badnell, A.D. Whiteford, D.H. Brooks, J. Lang, S.D. Loch, and D.C. Griffin, *Ionization state, excited populations and emission of impurities in dynamic finite density plasmas: I. The generalized collisional-radiative model for light elements*, Plasma Physics and Controlled Fusion **48** 263 (2006)

[16] Badnell N. R., *??*, J. Phys. B: At. Mol. Phys 1986; 19:3827.

[17] Badnell, N. R.: *A Breit-Pauli distorted-wave implementation for autostructure.* Comput. Phys. Commun. **182** 1528 (2011)

[18] Glassgold A. E., Najita J. R. and Igea J. *??* ApJ 2007; 656:515.

[19] Burke, P. G.: *R-matrix Theory of Atomic Collisions: Application to Atomic, Molecular and Optical Processes.* (New York, USA: Springer) (2011)

[20] F. Robicheaux, J. Phys. B **45**, 135007 (2012).

[21] F. Robicheaux, M.P. Jones, M. Schoffler, et al, J. Phys. B **45**, 175001 (2012).

[22] M. Yu. Kuchiev and S.A. Sheinerman, Sov.Phys.JETP **63**,1680(1986).

[23] M. Yu. Kuchiev and S.A. Sheinerman, J.Phys.B **21**,2027 (1988).

[24] M. Yu. Kuchiev and S.A. Sheinerman, J.Phys.B **27**,2943 (1994).

[25] P. van der Straten R. Morgenstern, and A. Niehaus, Z.Phys. D **8**,35 (1988).

[26] M. Yu. Kuchiev and S.A. Sheinerman, Sov.Phys.Usp. **32**,569 (1989).

[27] R. B. Barker and H. W. Berry, Phys. Rev. **151**, 14 (1966).

[28] F H Read, Radiat.Res. **64**, 23 (1975).

[29] G C King, F H Read, R C Bradford, J. Phys. B **8** 2210(1975).

[30] A Niehaus, J. Phys. B **10**, 1845 (1976).

[31] K. Helenelund, S. Hedman, L. Asplund, U. Gelius and K. Siegbahn, Phys. Scripta. **27**, 245 (1983). Rebirth of X-Ray Emission from the Born-again Planetary Nebula A30. *Astrophys. J.*, 755:129.

[32] V. N. Ostrovskii, Sov.Phys.-JETP **45**, 1092 (1977).

[33] M. Ya. Amus'ya, M. Yu. Kuchiev, S. A. Sheinerman, Sov.Phys.-JETP **47**, 238 (1979).

[34] M Yu Kuchiev and S A Sheinerman, J.Phys. B **18**, L551 (1985).

[35] J. Tulkki, G. B. Armen, T. Åberg, B. Crasemann, and M. H. Chen, Z.Physik D, **5**, 241(1987).

[36] G N Ogurtsov, J. Phys. B **16**, L745 (1983).

[37] Junya Mizuno, Takeshi Ishihara and Tsutomu Watanabe, J. Phys. B **18**, 1241 (1985).

[38] A Russek and W Mehlhorn, J.Phys. B **19**, 911 (1986)

[39] S.A. Sheinerman, P Lablanquie, F Penent, et al, J. Phys. B, **39**, 1017 (2006).

[40] L. Gerchikov and S. Sheinerman, Phys. Rev. A **84**, 022503 (2011).

[41] V. Schmidt, N. Sandner, W. Mehlhorn, M. Y. Adam, et al, Phys. Rev. Lett. **38**, 63 (1977).

[42] M. K. Bahl, R. L. Watson, and K. J. Irgollic, Phys. Rev. Lett. **42**, 165 (1979).

[43] B Lohmann, Xian-K Meng and M Keane, J. Phys. B **25**, 5223(1992).

[44] B Kämmerling, B Krässig and V Schmidt, J.Phys.B **26**,261(1993).

[45] L. Avaldi, P. Belotti, P. Bolognesi, R. Camilloni, and G. Stefani, Phys. Rev. Lett. **75**,1915 (1995).

[46] B. Kassühlke, R. Romberg, P. Averkamp, and P. Feulner, Phys. Rev. Lett. **81**, 2771(1998).

[47] S Sheinerman, and V Schmidt, J. Phys. B **32**, 5205(1999).

[48] S. Rioual, et al, Phys. Rev. Lett. **86**, 1470 (2001).

[49] N Scherer, H Lörch, T Kerkau and V Schmidt, J. Phys. B **37**, L121(2004).

[50] F. Penent, et al, Phys. Rev. Lett. **95**, 083002 (2005).

[51] S Sheinerman, et al, J. Phys. B **43**, 115001(2010).

[52] M J Van der Wiel, G R Wight and R R Tol, J.Phys.B **9**, L5 (1976).

[53] M Ya Amusia, M Yu Kuchiev, S A Sheinerman and S I Sheftel, J.Phys.B**10**, L535 (1977).

[54] W. Eberhardt, S. Bernstorff, H. W. Jochims, S.B. Whitfield, B. Crasemann, Phys. Rev. A **38**, 3808(1988).

[55] J. Tulkki, T. Åberg, S. B. Whitfield, and B. Crasemann, Phys. Rev. A **41**, 181(1990).

[56] G. B. Armen and Jon C. Levin Phys. Rev. A **56**, 3734(1997).

[57] S A Sheinerman, J.Phys.B **36**, 4435 (2003).

[58] A. De Fanis, et al, Phys. Rev. A **70**, 040702(R) (2004).

[59] S A Sheinerman, J.Phys.B **38**, 2279 (2005).

[60] A De Fanis, G Prümper, U Hergenhahn, et al, J. Phys. B **38**, 2229 (2005).

[61] U Hergenhahn, A De Fanis, G Prümper, et al, J. Phys. B **38**, 2843 (2005).

[62] Fumihiro Koike, J.Phys.Soc.Japan **57**, 2705 (1988).

[63] G. B. Armen, Jukka Tulkki, Teijo Aberg, and Bernd Crasemann, Phys. Rev. A **36**, 5606 (1987).

[64] M S Pindzola, F Robicheaux, S D Loch, et al, J. Phys. B **40**, R39 (2007).

[65] David Hochstuhl and Michael Bonitz J. Chem. Phys. **134**, 084106 (2011).

[66] David Hochstuhl and Michael Bonitz, Phys. Rev. A **86**, 053424(2012).

[67] J. Palaudoux, P. Lablanquie, L. Andric et al, J.Phys.: Conf. Ser. **141**, 012012 (2008).

[68] B Kämmerling, B Krässig, and V Schmidt, J. Phys. B **26**, 261(1993).

[69] M Yu Kuchiev and S A Sheinerman, J. Phys. B **27**, 2943(1994).

[70] J. Viefhaus, G. Snell, R. Hentges, M. Wiedenhöft, F. Heiser, O. Geβner, and U. Becker, Phys. Rev. Lett. **80**, 1618(1998).

[71] N. Scherer, H Lörch, T. Kerkau, and V. Schmidt, Phys. Rev. Lett. **82**, 4615(1999).

[72] N. Scherer, H Lörch, T Kerkau and V Schmidt, J. Phys. B **37**, L121(2004).

[73] M Wiedenhoeft, S E Canton1, A A Wills, T Gorczyca, J Viefhaus, U Becker and N Berrah1. J. Phys. B **41**, 095202(2008).

[74] S Sheinerman, P Lablanquie, F Penent, J Palaudoux, J H D Eland, T Aoto , Y Hikosaka and K Ito. J. Phys. B **39**, 1017(2006).

[75] S A Sheinerman, J. Phys. B **38**, 2279(2005).

[76] S. Rioual, B. Rouvellou, L. Avaldi, G. Battera, R. Camilloni, G. Stefani, and G. Turri, Phys. Rev. Lett. **86**, 1470 (2001).

[77] B. Rouvellou, S. Rioual, L. Avaldi, R. Camilloni, G. Stefani, and G. Turri, Phys. Rev. A **67**, 012706 (2003).

[78] M Yu Kuchiev and S A Sheinerman, J. Phys. B **21**, 2027(1988).

[79] P. Bolognesi and A. De Fanis, M. Coreno, and L. Avaldi, Phys. Rev. A **70**, 022701(2004).

[80] S A Sheinerman and V Schmidt, J. Phys. B **30**, 1677(1997).

[81] S Sheinerman, P Lablanquie, and F Penent J. Phys. B **40**, 1889(2007).

[82] F Penent, S Sheinerman, L Andric, P Lablanquie, et al J. Phys. B **41**, 045002(2008).

[83] Schmidt V 1997 Electron Spectrometry of Atoms Using Synchrotron Radiation(Cambridge: Cambridge University Press) pp 275, 276.

[84] Ballance, C. P., and Griffin D. C.: J. Phys. B: At. Mol. Opt. Phys. **39**, 3617 (2006)

[85] Ballance, C. P., Griffin, D. C., and McLaughlin, B. M.: J. Phys. B: At. Mol. Opt. Phys. **40** F327 (2007)

[86] Ballance, C. P., Loch S. D., Pindzola M. S., and Griffin D. C.: J. Phys. B: At. Mol. Opt. Phys. **46**, 055202 (2013)

[87] Berrington K. A., Burke P.G., Butler K., Seaton M.J., Storey P.J., Taylor K.T., and Yan Y., J. Phys. B 1987; 20:6379

[88] Grant, I. P.: *Quantum Theory of Atoms and Molecules: Theory and Computation* (New York, USA: Springer) (2007)

[89] Munoz Burgos J. M., Loch S. D., Ballance C. P., and Boivin R. F., A&A 2009; 500:1253.

[90] Parpia, F., Froese-Fischer, C., and Grant, I. P.: *Comput. Phys. Commun.* **94** 249 (2006)

[91] Pradhan A. K., J. Phys. B: At. Mol. Phys. 1974; 17:L503.

[92] Butler K. and Mendoza C., Mon. Not. R. Astron. Soc. 1984; 208:17P.

[93] Johnson C. T. and Kingston A. E., J. Phys. B: At. Mol. Phys. 1987; 20:5757.

[94] Saraph H. E. and Tully J. A., Astron. Astrophys. Suppl. 1994; 107:29

[95] Griffin D. C., Mitnik D. M. and Badnell N. R., J. Phys. B 2001; 34:4401.

[96] Colgan J., Loch S. D., Pindzola M. S., Ballance C. P., and Griffin D. C., Phys. Rev. A 2003; 68:032712.

[97] Berrington K. A., Ballance C. P., Griffin D C and Badnell N R, J. Phys. B: At. Mol. Opt. Phys. 2005; 38:1667.

[98] Witthoeft M C, Whiteford A D and Badnell N. R., J. Phys. B: At. Mol. Phys 2007; 40:2969.

[99] Munoz Burgos J. M., Loch S. D., Ballance C. P., and Boivin R. F., A&A 2009; 500:1253.

[100] Ludlow J. A., Lee T. G., Ballance C. P., Loch S. D., and Pindzola M. S., Phys. Rev. A 2011; 84:022701.

[101] Malespin C., Ballance C. P., Pindzola M. S., Witthoeft M. C., Kallman T. R. and Loch S. D., A&A 2011, 526:A115.

[102] McLaughlin B. M., Lee Teck-Ghee, Ludlow J. A., et al, J. Phys. B 2011, 44:175206.

[103] Wu Di, Loch S. D., Pindzola M. S., and Ballance C. P., Phys. Rev. A 2012; 85:012711.

[104] Abdel-Naby Sh. A., Ballance C. P., Lee T. G., Loch S. D., and Pindzola M. S., Phys. Rev. A 2013; 87: 022708.

[105] Abdel-Naby S A, Pindzola M S, Pearce A J, Ballance C P and Loch S D, J. Phys. B: At. Mol. Opt. Phys. 2015; 48:025203.

[106] Bahcall J. N. and Wolf R. A., ApJ 1968, 152: 701

[107] Meijerink R., Glassgold A. E. and Najita J. R., APJ 2008; 676:518.

[108] McLaughlin B M and Bell K L, J. Phys. B: At. Mol. Opt. Phys. 2000; 33:597.

[109] McLaughlin B M, Daw A and Bell K L, J. Phys. B: At. Mol. Opt. Phys. 2002; 35:283.

[110] Griffin D C, Badnell N R and Pindzola M S, J. Phys. B: At. Mol. Phys 1998; 31:3713.

[111] Berrington, K., Werner B. Eissner and Patrick H. Norringtona, comput. Phys. Commun. 1995; 92:290.

[112] Norrington P H and Grant I P, J. Phys. B: At. Mol. Phys 1981; 14:L261.

[113] Dyall, K. G., Grant, I. P., Johnson, C. T., and Plummer, E. P.: *GRASP: A general-purpose relativistic atomic structure program.Comput. Phys. Commun.* **55** 425 (1989)

[114] Chang J J, J. Phys. B: At. Mol. Phys 1975; 8:2327.

[115] Seaton M J, Proc. R. Soc. A 1953; 218:400.

[116] Eissner W, Martins P de A P, Nussbaumer H, Saraph H E and Seaton M J, Mon. Not. R. Astron. Soc. 1969; 146:63.

[117] *R-matrix DARC and BP codes website* `http://connorb.freeshell.org`

[118] Esteban, C., Bresolin, F., Peimbert, M., García-Rojas, J., Peimbert, A., and Mesa-Delgado, A. (2009). Keck HIRES Spectroscopy of Extragalactic H II Regions: C and O Abundances from Recombination Lines. *Astrophys. J.*, 700:654–678.

[119] Fang, X., Guerrero, M. A., Marquez-Lugo, R. A., Toalá, J. A., Arthur, S. J., Chu, Y.-H., Blair, W. P., Gruendl, R. A., Hamann, W.-R., Oskinova, L. M., and Todt, H. (2014). Expansion of Hydrogen-poor Knots in the Born-again Planetary Nebulae A30 and A78. *Astrophys. J.*, 797:100.

[120] Fogle, M., Badnell, N. R., Glans, P., Loch, S. D., Madzunkov, S., Abdel-Naby, S. A., Pindzola, M. S., and Schuch, R. (2005). Electron-ion recombination of Be-like C, N, and O. *Astronomy and Astrophysics*, 442:757–766.

[121] Harrington, J. P. and Feibelman, W. A. (1984). The remarkable ultraviolet spectrum of the planetary nebula Abell 30. *Astrophys. J.*, 277:716–724.

[122] Pindzola, M. S., Loch, S. D., and Robicheaux, F. (2011). Dielectronic recombination in C^{3+} above and below the ionization threshold. *Physical Review A*, 83(4):042705.

[123] Robicheaux, F., Loch, S. D., Pindzola, M. S., and Ballance, C. P. (2010). Contribution of Near Threshold States to Recombination in Plasmas. *Physical Review Letters*, 105(23):233201.

[124] Schippers, S., Schnell, M., Brandau, C., Kieslich, S., Müller, A., and Wolf, A. (2004). Experimental Mg IX photorecombination rate coefficient. *Astronomy and Astrophysics*, 421:1185–1191.

[125] Steffen, W. and López, J. A. (2004). On the Velocity Structure in Clumpy Planetary Nebulae. *Astrophys. J.*, 612:319–331.

[126] Wesson, R., Liu, X.-W., and Barlow, M. J. (2005). The abundance discrepancy - recombination line versus forbidden line abundances for a northern sample of galactic planetary nebulae. *Monthly Notices of the Royal Astronomical Society*, 362:424–454.

[127] J.E. Vernazza, E.H. Avrett, and R. Loeser, The Astrophysical Journal Supplement Series **45** 635 (1981)

[128] W. Curdt, P. Brekke, U. Feldman, K. Wilhelm, B.N. Dwivedi, U. Schühle, P. Lemaire, Astronomy and Astrophysics **375** 591 (2001)

Appendices

Appendix A

NUMERICAL PROCESS FOR THE TDSE METHOD

A.1 The non-uniform radial mesh for radius

We use non-uniform mesh for the radial grid to improve the efficiency of numerical calculation. We use equal steps for phase, so the transformation can be:

$$s = \sqrt{r}\sqrt{r_c + r}. \tag{A.1}$$

The grid in s is equal, $\delta s = \frac{s_f - s_i}{N}$ where $s_i = \sqrt{r_i}\sqrt{r_c + r_i}$ and $s_f = \sqrt{r_f}\sqrt{r_c + r_f}$. Then

$$s_j = \delta s * j. \tag{A.2}$$

Eq.s (A.1) and (A.2) will give

$$r_j = \sqrt{\frac{r_c^2}{4} + s_j^2} - \frac{r_c}{2}. \tag{A.3}$$

The mesh in r is small close to the nucleus, and smoothly becomes equal far away. r_c is selected as 20 a.u. for e_1 and 5 a.u. for e_2.

A.2 Numerical method to solve Eq. (1.1)

In Eq. (1.1),

$$H_1 F_1 = (-\frac{1}{2}\frac{\partial^2}{\partial r_1^2} + V_1)F_1. \tag{A.4}$$

Non-uniform mesh yields

$$(H_1 F_1)_j = -(\frac{F_{1j+1}}{\delta_{1j}\lambda_{1j}} + \frac{F_{1j-1}}{\delta_{1j-1}\lambda_{1j}} - \frac{F_{1j}}{\delta_{1j}\delta_{1j-1}}) + V_{1j}F_{1j}, \tag{A.5}$$

where $\delta_{1j} = r_{1j+1} - r_{1j}$ and $\lambda_{1j} = r_{1j+1} - r_{1j-1}$
Substitute (A.5) to Eq. (1.1), we can get:

$$D_j F_{1j+1} + M_j F_{1j} + L_j F_{1j-1} = -S_j, \tag{A.6}$$

where $D_j = -\frac{1}{\delta_{1j}\lambda_{1j}}$, $M_j = \frac{1}{\delta_{1j}\delta_{1j-1}} + V_{1j} - (E_1 + i\frac{\Gamma_c}{2})$, $L_j = -\frac{1}{\delta_{1j-1}\lambda_{1j}}$ and S= $D\phi_g = r_1 e^{-r_1^2}$.

$$
\begin{cases}
D_1 F_{12} + M_1 F_{11} = -S_1 \\
D_2 F_{13} + M_2 F_{12} + L_2 F_{11} = -S_2 \\
D_3 F_{14} + M_3 F_{13} + L_3 F_{12} = -S_3 \\
\dots \\
D_n F_{1n+1} + M_n F_{1n} + L_n F_{1n-1} = -S_n
\end{cases}
\tag{A.7}
$$

$F_{11} = (-S_1 - D_1 F_{12})/M_1$ can be obtained from the first equation of A.7. Plug this expression to the second equation of A.7,

$$
\begin{aligned}
& D_2 F_{13} + M_2 F_{12} + L_2/M_1(-S_1 - D_1 F_{12}) = -S2 \\
& \Rightarrow D_2 F_{13} + (M_2 - \tfrac{L_2 D_2}{M_1}) F_{12} = -(S_2 - \tfrac{L_2 S_1}{M_1}) \\
& \Rightarrow D_2 F_{13} + M_2' F_{12} = S_2'
\end{aligned}
\tag{A.8}
$$

.

And similar expression can be obtained from A.8: $F_{12} = (-S_2' - D_1 F_{12})/M_1'$. Plug it into the third equation of A.7,

$$
\begin{aligned}
& D_3 F_{14} + M_3 F_{13} + L_3/M_2'(-S_2' - D_2 F_{13}) = -S3 \\
& \Rightarrow D_3 F_{14} + (M_3 - \tfrac{L_3 D_2}{M_2'}) F_{13} = -(S_3 - \tfrac{L_3 S_2'}{M_2'}) \\
& \Rightarrow D_3 F_{14} + M_3' F_{13} = S_3'
\end{aligned}
\tag{A.9}
$$

.

Thus, Eqs. A.7 can be rewritten as:

$$
\begin{cases}
D_1 F_{12} + M_1' F_{11} = -S_1' \\
D_2 F_{13} + M_2' F_{12} = -S_2' \\
D_3 F_{14} + M_3' F_{13} = -S_3' \\
\dots \\
D_n F_{1n+1} + M_n' F_{1n} = -S_n'
\end{cases}
\tag{A.10}
$$

where $M_1' = M_1$, $S_1' = S_1$, $M_j' = M_j - \frac{L_j D_j}{M_{j-1}'}$ and $S_j' = S_j - \frac{L_j S_{j-1}'}{M_{j-1}'}$. j=2 to n. $F_{1n} = 0$, the wave-function at the point before it can be obtained by $F_{1n-1} = \frac{-S_{n-1}' - D_{n-1} F_{1n}}{M_{n-1}'}$. The wave-function at other points is solved in similar way.

Appendix B

Basic knowledge for R-matrix and Rate coefficients for Ne_+ and Ne_{2+}

B.1 R-matrix theory

A short summary of R-matrix theory is presented here and is used in chapter 6 of the dissertation. The R-matrix method is a non-perturbative approach to solving atomic physics collision cross sections. In this approach the configuration space is separated into 2 regions. In the first region (inside the R-matrix 'box') where electron exchange and correlation effects between the scattered electron and the target electrons are important, a configuration interaction basis expansion of the total wave function is adopted. In chapter 6 the atomic structure package AUTOSTRUCTURE [16] was used to generate the spectroscopic radial orbitals subsequently employed in the scattering calculation.

The wavefunction representing the close-coupling expansion in the inner region is given by:

$$\Psi_k^{N+1} = A \sum_{i,j} a_{ijk} \psi_i^{N+1} \frac{u_{ij}(r_{N+1})}{r_{N+1}} + \sum_i b_{ik} \chi_i^{N+1} \ , \tag{B.1}$$

where A is an antisymmetrization operator, ψ_i^{N+1} are channel functions obtained by coupling N-electron target states with the angular and spin functions of the scattered electron, $u_{ij}(r)$ are radial continuum basis functions, and χ_i^{N+1} are bound functions which ensure completeness of the total wavefunction. The χ_i^{N+1} terms are correlations terms, and are constructed only from target orbitals, and therefore will also have a negligible value on the the R-matrix boundary. The coefficients a_{ijk} and b_{ik} are determined by diagonalization of the total (N+1)-electron symmetric Hamiltonian.

The resulting eigenvalues and eigenvectors are subsequently used in the formation of the R-matrix, which acts as the interface between the inner and outer region is given by:

$$R_{ij}(E) = \frac{1}{2a_0} \sum_k \frac{w_{ik}w_{jk}}{E - E_k} \tag{B.2}$$

where E_k are the aforementioned eigenvalues of the $N+1$ electron Hamiltonian and w_{ik} are referred to as surface amplitudes. The w_{ik} are given by the following expression, where c_{ijk} correspond to the eigenvectors of the aforementioned Hamiltonian.

$$w_{ik} = \sum_j u_{ij}c_{ijk} \quad \text{at} \quad r = a_0 \tag{B.3}$$

The R-matrix relates the reduced radial wave function $F_i(r)$, describing the radial motion of the scattered electron in the ith channel, to its derivative on the boundary $r = a_0$.

$$F(r) = \sum_j R_{ij}(a_0 \frac{dF_j}{dr} - bF_j) \quad \text{at} \quad r = a_0 \tag{B.4}$$

The $n \times n$ R-matrix on the boundary can be related to the asymptotic form $n \times n$ K or S matrix from which cross sections may be derived, taking into account whether the system is a neutral or an ionic target. The final cross section in LS coupling for a transition from one state $\alpha_i L_i S_i$ to another $\alpha_j L_j S_j$ is given by

$$\sigma_{i \to j} = \frac{\pi}{k_i^2} \sum_{l_i, l_j} \frac{(2L+1)(2S+1)}{(2L_i+1)(2S_i+1)} |S_{ij} - \delta_{ij}|^2 \tag{B.5}$$

We use the R-matrix method to calculate electron-impact excitation cross sections in chapter 6.

B.2 Rate coefficients for Ne$^+$ and Ne^{2+}

Temperature	Ne$^+$ 2s^{2}2p^5(^{2}P$^0_{3/2}$) - (^{2}P$^0_{1/2}$)	Ne^{2+} 2s^{2}2p^4(^{3}P$_2$) - (^{3}P$_1$)	Ne^{2+} 2s^{2}2p^4(^{3}P$_1$) - (^{3}P$_0$)	Ne^{2+} 2s^{2}2p^4(^{3}P$_2$) - (^{3}P$_0$)
(K)	Υ_{12}, %Δ, q$_{12}$ (cm^{-3})	Υ_{12}, %Δ, q$_{12}$ (cm^{-3})	Υ_{23}, %Δ, q$_{23}$ (cm^{-3})	Υ_{13}, %Δ, q$_{13}$ (cm^{-3})
1.00×10^1	0.30, 4.77, 4.42$\times 10^{-56}$	0.63, 12.2, 1.25$\times 10^{-47}$	0.19, 19.8, 1.24$\times 10^{-24}$	0.16, 16.2, 2.27$\times 10^{-65}$
2.00×10^1	0.30, 4.79, 6.72$\times 10^{-32}$	0.64, 8.51, 1.47$\times 10^{-27}$	0.19, 17.7, 3.22$\times 10^{-16}$	0.15, 13.0, 9.67$\times 10^{-37}$
3.00×10^1	0.30, 4.82, 7.09$\times 10^{-24}$	0.64, 7.74, 6.62$\times 10^{-21}$	0.19, 17.0, 1.89$\times 10^{-13}$	0.15, 11.9, 3.10$\times 10^{-27}$
4.00×10^1	0.30, 4.78, 6.97$\times 10^{-20}$	0.64, 7.73, 1.34$\times 10^{-17}$	0.18, 16.7, 4.35$\times 10^{-12}$	0.15, 11.2, 1.67$\times 10^{-22}$

5.00×10^1	0.30, 4.78, 1.69×10^{-17}	0.64, 7.99, 1.26×10^{-15}	0.18, 16.4, 2.80×10^{-11}	0.15, 10.8, 1.13×10^{-19}
6.00×10^1	0.30, 4.78, 6.47×10^{-16}	0.64, 8.18, 2.57×10^{-14}	0.18, 16.3, 9.47×10^{-11}	0.15, 10.5, 8.58×10^{-18}
7.00×10^1	0.30, 4.81, 8.63×10^{-15}	0.64, 8.49, 2.19×10^{-13}	0.18, 16.3, 2.24×10^{-10}	0.15, 10.4, 1.85×10^{-16}
8.00×10^1	0.30, 4.81, 5.97×10^{-14}	0.64, 8.80, 1.08×10^{-12}	0.18, 16.1, 4.24×10^{-10}	0.15, 10.0, 1.85×10^{-15}
9.00×10^1	0.30, 4.81, 2.67×10^{-13}	0.64, 9.04, 3.73×10^{-12}	0.18, 16.0, 6.88×10^{-10}	0.15, 10.0, 1.10×10^{-14}
1.00×10^2	0.30, 4.81, 8.80×10^{-13}	0.64, 9.29, 9.96×10^{-12}	0.18, 16.0, 1.01×10^{-09}	0.15, 10.0, 4.55×10^{-14}
1.10×10^2	0.30, 4.80, 2.33×10^{-12}	0.64, 9.53, 2.22×10^{-11}	0.18, 16.0, 1.38×10^{-09}	0.15, 10.0, 1.45×10^{-13}
1.20×10^2	0.30, 4.80, 5.22×10^{-12}	0.64, 9.76, 4.31×10^{-11}	0.18, 15.8, 1.77×10^{-09}	0.15, 10.0, 3.79×10^{-13}
1.50×10^2	0.30, 4.80, 3.02×10^{-11}	0.64, 10.3, 1.83×10^{-10}	0.18, 16.0, 3.06×10^{-09}	0.15, 9.62, 3.07×10^{-12}
2.00×10^2	0.30, 4.76, 1.69×10^{-10}	0.65, 11.0, 7.48×10^{-10}	0.18, 16.0, 5.06×10^{-09}	0.15, 9.62, 2.42×10^{-11}
2.50×10^2	0.30, 4.76, 4.64×10^{-10}	0.64, 11.4, 1.69×10^{-09}	0.18, 16.1, 6.68×10^{-09}	0.15, 9.49, 8.15×10^{-11}
3.00×10^2	0.30, 4.76, 8.95×10^{-10}	0.64, 11.7, 2.86×10^{-09}	0.18, 16.2, 7.89×10^{-09}	0.15, 9.49, 1.80×10^{-10}
3.50×10^2	0.30, 4.76, 1.41×10^{-09}	0.64, 11.9, 4.10×10^{-09}	0.18, 16.3, 8.76×10^{-09}	0.15, 9.05, 3.11×10^{-10}
4.00×10^2	0.30, 4.79, 1.97×10^{-09}	0.63, 11.9, 5.32×10^{-09}	0.18, 16.2, 9.38×10^{-09}	0.15, 8.88, 4.67×10^{-10}
4.50×10^2	0.30, 4.79, 2.54×10^{-09}	0.63, 11.9, 6.44×10^{-09}	0.17, 16.3, 9.82×10^{-09}	0.15, 8.56, 6.37×10^{-10}
5.00×10^2	0.30, 4.79, 3.09×10^{-09}	0.62, 11.7, 7.47×10^{-09}	0.17, 15.9, 1.01×10^{-08}	0.15, 8.07, 8.11×10^{-10}
5.50×10^2	0.30, 4.75, 3.61×10^{-09}	0.62, 11.6, 8.38×10^{-09}	0.17, 15.8, 1.03×10^{-08}	0.15, 7.59, 9.84×10^{-10}
6.00×10^2	0.30, 4.75, 4.09×10^{-09}	0.62, 11.2, 9.18×10^{-09}	0.17, 15.5, 1.05×10^{-08}	0.15, 7.21, 1.14×10^{-09}
6.50×10^2	0.30, 4.75, 4.54×10^{-09}	0.61, 10.8, 9.87×10^{-09}	0.17, 14.9, 1.05×10^{-08}	0.15, 6.67, 1.30×10^{-09}
7.00×10^2	0.30, 4.75, 4.95×10^{-09}	0.61, 10.4, 1.05×10^{-08}	0.17, 14.3, 1.05×10^{-08}	0.15, 6.20, 1.45×10^{-09}
7.50×10^2	0.30, 4.75, 5.34×10^{-09}	0.60, 9.92, 1.10×10^{-08}	0.17, 13.6, 1.05×10^{-08}	0.15, 5.79, 1.59×10^{-09}
8.00×10^2	0.30, 4.75, 5.67×10^{-09}	0.60, 9.43, 1.15×10^{-08}	0.17, 12.9, 1.04×10^{-08}	0.15, 5.49, 1.73×10^{-09}
8.50×10^2	0.30, 4.75, 5.98×10^{-09}	0.60, 8.90, 1.19×10^{-08}	0.17, 12.2, 1.04×10^{-08}	0.15, 5.62, 1.85×10^{-09}
9.00×10^2	0.30, 4.71, 6.25×10^{-09}	0.60, 8.36, 1.22×10^{-08}	0.17, 11.3, 1.03×10^{-08}	0.15, 5.72, 1.96×10^{-09}
9.50×10^2	0.30, 4.71, 6.50×10^{-09}	0.60, 7.75, 1.25×10^{-08}	0.17, 10.8, 1.03×10^{-08}	0.15, 6.18, 2.07×10^{-09}
1.00×10^3	0.30, 4.74, 6.72×10^{-09}	0.59, 7.24, 1.28×10^{-08}	0.17, 9.85, 1.02×10^{-08}	0.15, 6.49, 2.17×10^{-09}
1.05×10^3	0.30, 4.74, 6.91×10^{-09}	0.59, 6.75, 1.30×10^{-08}	0.17, 9.11, 1.01×10^{-08}	0.15, 7.10, 2.26×10^{-09}
1.10×10^3	0.30, 4.74, 7.09×10^{-09}	0.59, 6.30, 1.32×10^{-08}	0.17, 8.37, 1.01×10^{-08}	0.15, 7.50, 2.35×10^{-09}
1.15×10^3	0.30, 4.74, 7.25×10^{-09}	0.59, 5.95, 1.34×10^{-08}	0.17, 7.43, 9.93×10^{-09}	0.15, 7.62, 2.44×10^{-09}
1.20×10^3	0.30, 4.74, 7.39×10^{-09}	0.59, 5.59, 1.35×10^{-08}	0.17, 6.69, 9.86×10^{-09}	0.15, 8.36, 2.51×10^{-09}
1.25×10^3	0.30, 4.70, 7.52×10^{-09}	0.59, 5.28, 1.37×10^{-08}	0.17, 6.19, 9.85×10^{-09}	0.15, 8.82, 2.59×10^{-09}
1.30×10^3	0.30, 4.70, 7.63×10^{-09}	0.59, 5.10, 1.38×10^{-08}	0.17, 5.48, 9.77×10^{-09}	0.15, 9.29, 2.66×10^{-09}
1.35×10^3	0.30, 4.70, 7.73×10^{-09}	0.59, 4.91, 1.39×10^{-08}	0.17, 4.84, 9.70×10^{-09}	0.16, 9.48, 2.73×10^{-09}
1.40×10^3	0.30, 4.70, 7.84×10^{-09}	0.59, 4.84, 1.41×10^{-08}	0.17, 4.46, 9.62×10^{-09}	0.16, 9.94, 2.79×10^{-09}
1.45×10^3	0.30, 4.70, 7.92×10^{-09}	0.59, 4.81, 1.42×10^{-08}	0.17, 3.98, 9.61×10^{-09}	0.16, 10.1, 2.85×10^{-09}
1.50×10^3	0.30, 4.70, 7.99×10^{-09}	0.60, 4.75, 1.43×10^{-08}	0.17, 3.82, 9.53×10^{-09}	0.16, 10.3, 2.91×10^{-09}
1.55×10^3	0.30, 4.70, 8.06×10^{-09}	0.60, 4.86, 1.43×10^{-08}	0.17, 3.33, 9.46×10^{-09}	0.16, 10.8, 2.96×10^{-09}
1.60×10^3	0.30, 4.70, 8.11×10^{-09}	0.60, 4.99, 1.44×10^{-08}	0.17, 3.24, 9.44×10^{-09}	0.16, 10.7, 3.03×10^{-09}
1.65×10^3	0.30, 4.66, 8.16×10^{-09}	0.60, 5.01, 1.45×10^{-08}	0.17, 3.39, 9.42×10^{-09}	0.16, 10.8, 3.08×10^{-09}
1.70×10^3	0.30, 4.69, 8.20×10^{-09}	0.60, 5.15, 1.46×10^{-08}	0.17, 3.39, 9.35×10^{-09}	0.16, 11.0, 3.13×10^{-09}
1.75×10^3	0.30, 4.69, 8.23×10^{-09}	0.61, 5.25, 1.47×10^{-08}	0.17, 3.20, 9.33×10^{-09}	0.16, 11.2, 3.17×10^{-09}
1.80×10^3	0.30, 4.69, 8.27×10^{-09}	0.61, 5.41, 1.47×10^{-08}	0.17, 3.44, 9.31×10^{-09}	0.17, 11.4, 3.21×10^{-09}
1.85×10^3	0.30, 4.69, 8.29×10^{-09}	0.61, 5.49, 1.48×10^{-08}	0.17, 3.62, 9.24×10^{-09}	0.17, 11.3, 3.25×10^{-09}
1.90×10^3	0.30, 4.69, 8.31×10^{-09}	0.61, 5.66, 1.48×10^{-08}	0.17, 3.71, 9.22×10^{-09}	0.17, 11.2, 3.31×10^{-09}
1.95×10^3	0.30, 4.69, 8.33×10^{-09}	0.62, 5.75, 1.49×10^{-08}	0.17, 3.81, 9.20×10^{-09}	0.17, 11.4, 3.35×10^{-09}
2.00×10^3	0.30, 4.68, 8.37×10^{-09}	0.62, 5.85, 1.49×10^{-08}	0.17, 3.94, 9.19×10^{-09}	0.17, 11.3, 3.38×10^{-09}

Table B.1: Effective collision strengths Υ_{12}, uncertainty %Δ and excitation rate coefficients q_{ij} for Ne$^+$ and Ne^{2+} calculated by the DARC approach with $n = 2$ target expansion.

Appendix C

Hubble Space Telescope proposal for Abell 30

C.1 Justification

Background, goals and significance of this proposal

Low temperature photoionized plasmas have a number of currently unexplained mysteries, such as the discrepancies between electron temperatures as derived from Optical Recombination Lines (ORL) and those from Collisionally Excited Lines (CEL) [118, 126]. The Born Again planetary nebulae (Abell 30, Abell 58, Abell 78, and V4334 Sgr) are particularly important objects for study. In this proposal we are requesting STIS/MAMA spectral observations at 1550 Å of one of the knots of plasma in Abell 30, with the aim of confirming a new low temperature recombination mechanism that has been recently proposed [123]. If confirmed, this would be the first observational evidence of this new mechanism. This would have a large potential impact on the modeling and understanding of low temperature photo-ionized plasmas.

Born Again planetary nebulae (and Abell 30 in particular) are also of interest in their own regard and would benefit from high resolution UV spectral measurements. They have hydrogen-deficient knots of plasma which were ejected by a late thermal pulse and are embedded in a fast stellar wind [119]. Thus, there is a large H-rich outer nebula which surrounds irregularly shaped H-deficient structures closer to the star. The behavior of the H-deficient knots of plasma are key indicators of the dynamic processes in the nebula. They are sensitive to both the stellar wind and the background nebula, leading to complex velocity structures [125]. C IV resonance lines are used for many spectral diagnostics of Abell 30. However, if the proposed below threshold spectral lines exist, they would be blended with the resonance lines in lower resolution spectra, leading to an underestimation of the flux in the resonance
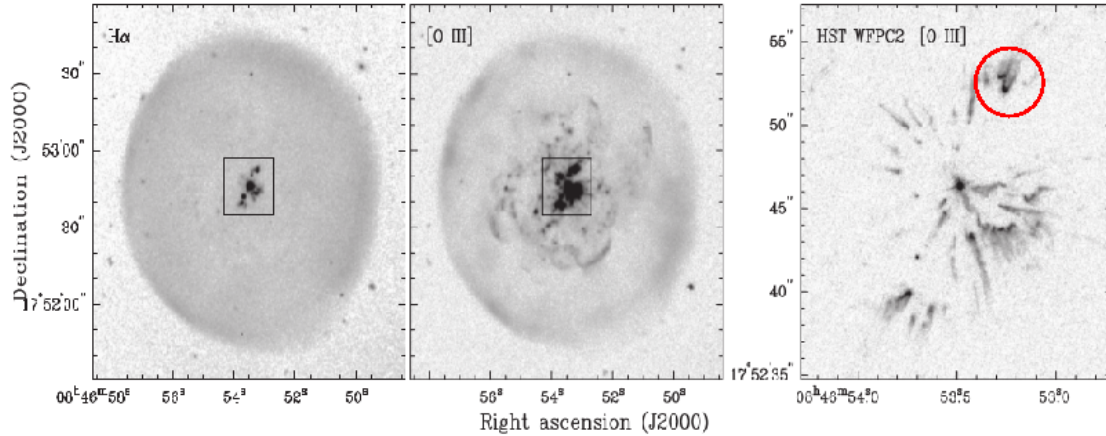
Figure C.1: Images of Abell 30, figure taken from Guerrero et al. [13]. The left hand figure shows an Hα image and center figure shows an O III image. Both of these were taken from ground based observations. The right hand image shows an O III image with taken using HST WFPC2 and the F502N filter.

lines. The extra recombination would also not be reflected in line ratio diagnostics for carbon ionic abundance. Thus, the proposed observations can also aid in the understanding of these low density Planetary Nebulae. Recently X-ray observations have also been used to study Abell 30 [13]. Figure 1 shows images of Abell 30; the knot of plasma that we wish to observe with STIS is circled in the right hand side figure.

Low temperature recombination of electrons in plasmas can proceed via radiative (RR) or dielectronic recombination (DR). The process of DR proceeds via capture of a free electron into a doubly excited state and results in spectral features known as satellite lines, due to their proximity to nearby resonance lines. Robicheaux et al. (2010) showed that in very low temperature conditions, it should be possible for the electrons to recombine via 'below threshold resonances'. This has the effect of enhancing the recombination at low temperatures and could be the resolution to long standing problems in current low temperature DR databases [120, 124]. It is important to stress that this mechanism is currently ignored in all modeling of low temperature photo-ionized plasmas. One of the reasons for this is that
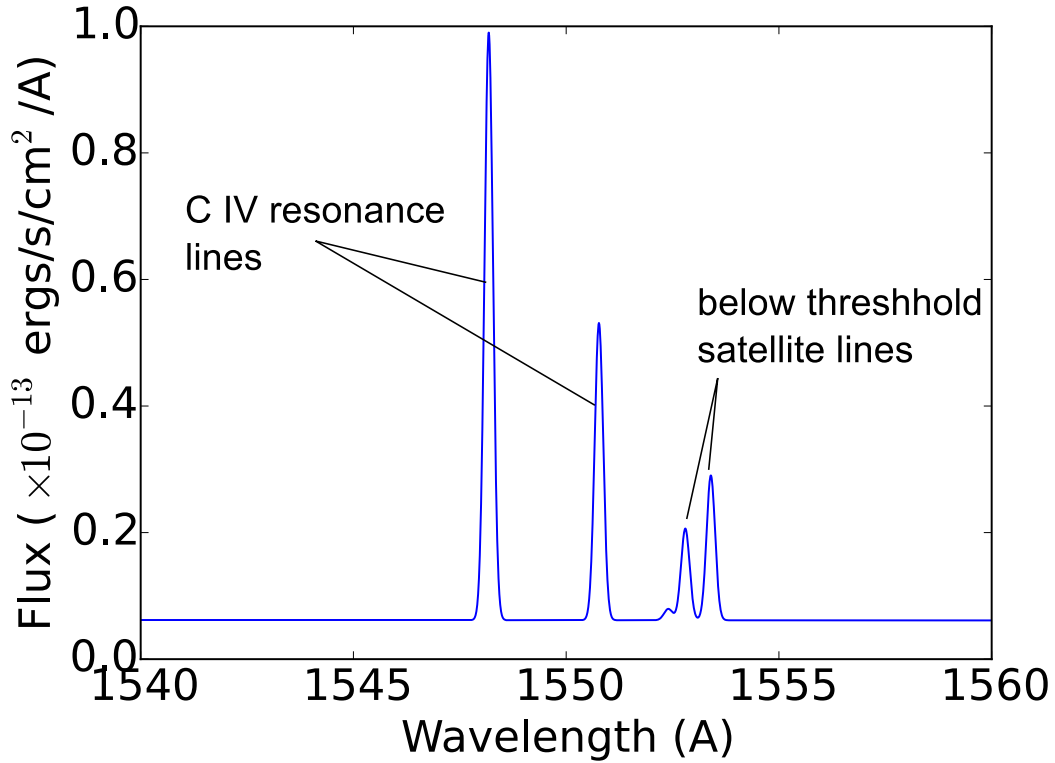
Figure C.2: Synthetic spectrum of the knot in Abell 30, with the spectral resolution of STIS, assuming an electron temperature of 9,200K.

there is as yet no experimental evidence of this new recombination mechanism. However, this mechanism should produce satellite lines which could be observed.

After a search through possible candidates, we have identified C IV as one of the best cases for observing such satellite line features. Fig. C.2 shows the predicted emission from knot #3 of Abell 30 for Te=9,200 K . Note that the satellite lines are at 1553 Å, while the two resonance lines are at 1548 Å and 1550 Å, so should be easily resolvable with STIS using the G140M grating. The plasma conditions required for the below threshold satellite lines of C IV to be strong are an electron temperature less than 11,400 K and a significant C^{3+} abundance. The knots in Abell 30 show evidence of both of these conditions [121]. We have evaluated the expected wavelength positions of these satellite lines based upon NIST energies, and have evaluated a synthetic spectrum based upon recently calculated below

threshold dielectronic capture rate coefficients [122], see Fig. C.2. Thus, Abell 30 is the ideal candidate to provide evidence of this new recombination mechanism, but requires high resolution UV measurements close to 1550 Å.

A number of discrepancies reported by Harrington and Feibelman [121] could be explained by the presence of this new recombination mechanism. They showed that the electron temperature derived from C IV λ 1549 / C III λ 4650 lines in knot 3 was 10,600K, Similarly the T_e derived from the C III λ 1909 / C II λ 4267 lines was 7,800 K. However, these were in marked contrast from the temperatures derived from Ne IV lines (which gave T_e=18,300 K), or from O III lines (which gave T_e = 16,400 K). They speculate that *"one approach would be to postulate the existence of some as yet undiscovered process which augments the carbon recombination lines"*

They also point out that the line intensity of CII λ 1909 is uncommonly weak compared with the C IV λ 1549 Å line. They look for a mechanism to reduce the intensity of the λ 1909 Å line, but cannot find a good candidate. A different possibility is that the 1549 Å line is enhanced through the presence of satellite lines that could not be resolved in the IUE spectrum used by Harrington and Feibelman [121].

The effect of this new recombination mechanism would be strongest on C IV, and would result in extra radiative cooling in the carbon rich parts of the nebula. This has the potential to explain the temperature discrepancies between the C, N and O diagnostics.

Thus, this proposal will address two main objectives:

- Search for spectroscopic evidence for a new recombination mechanism that could affect many low temperature plasmas, and as a result have a large impact on our understanding and modeling of these plasmas.

- Assist in a better understanding of the features in Abell 30, resolving some existing discrepancies.

C.2 Description of the Observation

We are requesting an observation of a region of the planetary nebula Abell 30, coordinates RA 08:46:53.29 DEC +17:52:53.5. The feature in question (referred to as knot #3 in Harrington and Feibelman [121]) is approximately 3 arsec × 3 arcsec. The feature is approximately 6.6 arsec from the central star, see Fig. 1. In our positioning of the detector, we have allowed for the proper motion of the knot since the WFPC2 observation was made, with this motion being quantified recently [119].

We are requesting a STIS FUV-MAMA observation of the object, using the G140M grating (1550 Å) and the $52''$ × $0.2''$ slit. The spectral feature that we are interested in is expected to be at 1553 Å, resolvable from the C IV resonance lines at 1548 and 1550 Å. We are requesting 5 orbits to gather the spectral data.

We estimate the flux and S/N ratio for the observation using the measured C IV flux in knot 3 reported by Harrington and Feibelman [121]. They gave a C IV flux of 1.2×10^{-12} ergs/cm^2/s, and the WFPC2 observations of Abell 30 in O III [Prop.ID 5404] showed that the knot is $3''$ × $3''$, giving an expected flux of 1.33×10^{-13}erg/cm^2/s/arcsec^2. Our spectral feature is at 1553 Å, thus we convert from ergs to photon counts to get a count rate of 0.0103 ph/cm^2/s/arcsec^2.

Applying this to the HST mirror (57000 cm^2), gives a photon count on mirror of 591 counts/s. One HST orbit is 3200 s, so we expect the count rate to be 1.89×10^6 counts/orbit. Throughput of the STIS instrument is 0.5%, resulting in 9.45×10^3 photons/orbit detected in the C IV resonance lines. The detector has $(\frac{3}{0.025})$ × $(\frac{0.2}{0.025})$=960 pixels that would view the knot, thus we expect about 10 counts/pixel on each orbit from the main resonance lines. The below threshold satellite lines that we are looking for are about a factor of 5 times smaller than the resonance lines, so would produce about 2 counts/pixel on each orbit (total counts of 1890 counts/orbit).

The Dark count for STIS would be $(1 \times 10^{-14}$ couts/s/pixel) × 3200 s × 960 pixels=307.2 counts/orbit. The spectrum also has a possible recombination continuum at this

wavelenth. However, Harrington et al. (1984) attribute almost all of their continuum emission to starlight on their detector. If this is true, then we would have negligible continuum contribution in the STIS observations, as the star would not be in the slit. This would lead to a S/N ratio for the below threshold lines of 6. If we assume that all of the continuum radiation observed by Harrington et al. would contribute to our signal, we get a S/N ratio of 2 (ETC ID: STIS.sp.801988).

C.3   Special Requests

To ensure that the observation includes the knot of interest, we are requesting an Orient of 90 degrees. The motion of the knots has been measured by Feng et al (2011), and was found to be 0.1" in twenty years for the inner knots and 1" in twenty years for the outer knots. This Orient value results in about 60 days/year where the observations could be scheduled.

We do not expect the nearby star in Abell 30 to be producing a dangerous flux on the detector as it does appear in the viewing apperture. The closest distance from the slit to the star would be 1.4 arcsecs. The flux from the star also falls below the safety threshold for STIS. An ETC calculations (ID:STIS.sp.802129) show that the counts per second on the detector if the star were visible would be 723 counts/s on the entire detector for each complete orbit. For the ETC calculation we used the esimated stellar flux from Harrington and Feibelman [121].